PROCESSING AND CHARACTERIZATION OF ATZ AND YSZ-GRAPHENE COMPOSITES FOR FABRICATION OF MEMS SCALE MICROTHRUSTER

KALAIMANI MARKANDAN

Thesis submitted to the University of Nottingham

for the Degree of Doctor of Philosophy

JANUARY 2017

DECLARATION

I hereby declare that the present work is prepared solely by me during the course of my doctoral studies at the University of Nottingham Malaysia Campus (UNMC). It has not been submitted anywhere for any award. Work of other people is fully acknowledged according to standard referencing.

This thesis complies fully with the regulations set by the University of Nottingham.

Kalaimani Markandan

January 2017

List of Publications

1. **K. Markandan**, J. K. Chin and M. T. T. Tan (2014) 'Study on Mechanical Properties of Zirconia-Alumina Based Ceramics', Applied Mechanics and Materials. doi: 10.4028/www.scientific.net/AMM.625.81
2. **K. Markandan**, M. T. T. Tan, J. Chin and S. S. Lim (2015) 'A novel synthesis route and mechanical properties of Si–O–C cured Yttria stabilised zirconia (YSZ)–graphene composite', Ceramics International. doi: 10.1016/j.ceramint.2014.11.008
3. **K. Markandan**, J. K. Chin and M. T. T. Tan (2015) 'The Effect of Different Sintering Strategies on Properties of YSZ Composites', MATEC Web of Conferences. doi: 10.1051/matecconf/20152601001
4. **K. Markandan**, J. K. Chin and M. T. T. Tan (2016) 'Recent progress in graphene based ceramic composites: A review', Journal of Materials Research. doi: 10.1557/jmr.2016.390.
5. **K. Markandan**, J. K. Chin and M. T. T. Tan (2016) 'Enhancing Electroconductivity of Yttria-Stabilised Zirconia Ceramic Using Graphene Platelets', Key Engineering Materials. doi: 10.4028/www.scientific.net/KEM.690.1
6. **K. Markandan**, J. K. Chin and M. T. T. Tan (2016) 'Low temperature fabrication and characterization of Si-O-C cured alumina toughened zirconia ATZ', Materials Today: Proceedings. [In press]

ABSTRACT

Structural ceramics such as zirconia and alumina are widely used in the materials industry owing to their high hardness, chemical inertness and electrical insulation properties. However, they bear the disadvantage of low fracture toughness that has limited their further applications. As such, ceramics with improved fracture toughness are desired in many engineering fields.

As for silicones, they are extensively used in current micro-electromechanical system (MEMS) components such as fuel cells and combustion engines. However, in hot and aggressive environments, silicon reduces functionality and efficiency of the components. Besides, low hardness and toughness of silicone material is undesirable in MEMS components. The ideal MEMS components require that the material has excellent structural strength at high temperature, exceptional thermal shock resistance and resistant to chemical corrosion. In view of these limitations, ceramics are currently being used to fabricate MEMS components.

This PhD project sets out to tackle the disadvantages of ceramics such as brittleness and low electrical conductivity by developing ceramic nanocomposites using nanostructured fillers. Graphene nanoplatelets (GNPs) - a newly emerging carbon nanomaterial and alumina were chosen as the reinforcing fillers. Two types of composites namely alumina toughened zirconia (ATZ) and yttria stabilized zirconia- graphene (YSZ-Gr) composites were fabricated and their properties were investigated. These composites were produced by gel-casting route on PDMS soft molds. There were two main problems in fabrication of YSZ-Gr composites: (i) achieving homogenous dispersion of graphene in ceramic matrix and (ii) production of good quality graphene. The first problem was solved by dispersing

commercially available graphene platelets in a surfactant; cetyltrimethylammonium bromide (CTAB). Scanning electron microscopy (SEM) ascertains homogenously dispersion of graphene in the ceramic matrix. In order to solve the second problem, processing parameters such as stirring speed and duration were optimised before fabricating the composites.

Nearly dense ATZ and YSZ-Gr ceramic composites were obtained after sintering and infiltration with PDC resin (RD-212a). The prepared ceramic composites were characterized and their properties were studied. Analysis shows that hardness and fracture toughness of composites increased with the addition of fillers. For ATZ composites, there was an improvement of ≈25.26 % in fracture toughness and ≈16.29 % in hardness with 20 wt. % alumina. For YSZ-Gr composites, there was an improvement of ≈20.31 % in fracture toughness and ≈25.78 % in hardness with 1 wt. % GNP. Electrical conductivity of YSZ-Gr composites was increased by ≈9 orders of magnitude with 2 wt. % GNP compared to pure YSZ.

The idea of this research is to use the two materials (ATZ and YSZ-Gr) to fabricate a MEMS scale chemical microthruster for space applications. Graphene provides conductive paths to decompose propellant (hydroxylammonium nitrate, HAN) and hence produces thrust. The characterization and testing of microthruster revealed that the proposed design is a success where; optimum thrust of 180.5 mN was achieved at a propellant flow rate of 60 µl/min. Future work should focus on optimization of chamber geometry, nozzle geometry and fuel choices to enable thruster to produce larger forces while decreasing the power consumption. Modelling and simulation of MEMS microthrusters can be used to verify the experimental results obtained.

ACKNOWLEDGEMENT

My years in UNMC could be one of the most precious and valuable moments in my life-thanks to so many wonderful people around me. I am such a blessed person. It would not even be possible to list all the names that I want to and should thank for being there as companions and helping me with walking all the way through.

First and foremost, I would like to thank both my PhD supervisors Associate Prof. Dr. Chin Jit Kai and Associate Prof. Dr. Michelle Tan, not only for the expert guidance they provided me during my research but also for providing me with the ability to work in a simulating environment with continuous learning. Dr. Chin has been a constant source for my motivation and I have always been impressed by his dedication towards research. Dr. Michelle has always been supportive of my direction in research. Without their encouragement and kind guidance, I could not have completed my thesis. I owe considerable gratitude to them for being very caring and thoughtful supervisors.

I would like to thank all my friends who made research life in UNMC very meaningful. Every one of them were wonderful and amazing. It was because of them that I enjoyed going to the office and labs even when I underwent hardships with research. I will miss them so much. There are numerous people I want to remember always and thank at UNMC (just to name a few): Abhay, Haroon, Revathy, Harshini, Asad, Anand, and my co-hall tutor, Pooria.

While I was in UNMC, I had the privilege to travel to China, India and Thailand for conferences. I would like to thank Faculty of Engineering UNMC and MOSTI (E-Science code: 04-02-12-SF0198) for the funding provided. The final icing on the cake and probably the best achievement I have till date was winning the grand prize at the UNMC's

annual FOE postgraduate research showcase where the grand prize was a travel fund to the UK, for which I am very grateful to the Nottingham University's Faculty of Engineering.

Special thanks to my family for encouraging me throughout my PhD. I am grateful to my father, Markandan and mother Muthamah for all the sacrifices they made so that I can have good education. Words cannot express how blessed I feel to be your daughter. To my sister, Dr. Uma thanks to you for tolerating my dramas and I love you!

Finally yet importantly, I would like to thank the technicians in UNMC who have helped me so much throughout my research. Just to name a few: Filzah, Khairani and Fareez- thank you so much!

TABLE OF CONTENTS

LIST OF ABBREVIATIONS

Al_2O_3	:	Alumina
APS	:	Ammonium persulphate
ATZ	:	Alumina toughened zirconia
C-MEMS	:	Ceramic microelectromechanical systems
CNT	:	Carbon nanotubes
CTAB	:	Cetyltrimethylammonium bromide
DMA	:	Dynamic mechanical analysis
EDL	:	Electric double layer
FLG	:	Few layer graphene
FT-IR	:	Fourier transform infrared spectroscopy
GCMC	:	Graphene ceramic matrix composites
GNP	:	Graphene nanoplatelets
GNS	:	Graphene nanosheets
GO	:	Graphene oxide
HAN	:	Hydroxylammonium nitrate
HMAM	:	Hydroxymethylacrylamide
HTCC	:	High temperature co-fired ceramic
HFIHS	:	High frequency induction heat sintering
IEP	:	Isoelectric point
KBr	:	Pottasium bromide
LTCC	:	Low temperature co-fired ceramic
MAM	:	Methacrylamide

MBAM	:	N,N- methylenebisacrylamide
MEMS	:	Microelectromechanical systems
MWCNT	:	Multi walled carbon nanotubes
PAM	:	Polyacrylamide
PDC	:	Polymer derived ceramic
PDMS	:	Polydimethylsiloxane
PIP	:	Polymer infiltration pyrolysis
PVP	:	Polyvinylpyrolidone
SEM	:	Scanning electron microscopy
SPS	:	Spark plasma sintering
SWCNT	:	Single walled carbon nanotubes
TEM	:	Transmission electron microscopy
TEMED	:	Tetramethylethylenediamine
TGA	:	Thermal gravimetric analysis
VLM	:	Vaporizing liquid microthruster
XRD	:	X-ray diffraction
YSZ	:	Yttria stabilized zirconia
YSZ-Gr	:	Yttria stabilized zirconia-graphene
ZrO_2	:	Zirconia
ZTA	:	Zirconia toughened alumina

LIST OF FIGURES

LIST OF TABLES

Chapter 4

Chapter 5

Chapter 1

Introduction

"Ceramics once referred purely to pottery and to articles made by firing materials extracted from the earth. Today, the term has a much broader definition. A ceramic material is an inorganic, non-metallic, often crystalline oxide, nitride or carbide material with a range of useful properties; including very high hardness, strength, durability and extremely high melting points".

-Chris Woodford-

1.1 Thesis background

1.1.1 Ceramic composites

Monolithic ceramics have attractive properties such as high mechanical strength and stability at high temperatures which make them useful for electronic, biomedical, automotive and space applications. Despite the fact that monolithic ceramics are promising structural materials; they are susceptible to brittleness, mechanical unreliability and poor electrical conductivity. In view of these limitations, ceramic matrix composites (CMC) have been developed. In earlier stages, much effort had been focussed on incorporation of a second ceramic material as filler to produce ceramic matrix composites of higher structural reliability. For example, zirconia toughened alumina (ZTA) and alumina toughened zirconia composites (ATZ) were invented. Studies have shown that these ceramic composites show improved strength and toughness in comparison to monolithic ceramics [1–4]. The advantages of

monolithic ceramics such as high strength, high temperature stability, damage tolerance and fracture toughness extends the application scope of ceramic composites [5,6]. Oxide ceramic as reinforcement for CMC are of enormous interest for technical applications in aerospace and power engineering industries because of their excellent resistance in oxidative and corrosive atmospheres [7]. Furthermore, ceramic composites with excellent mechanical stability and relatively low density compared to metals make them a potential material in aerospace industry.

In the last decade, research was focussed mainly on graphene reinforced ceramic composites. Thanks to exceptional properties of graphene (Young's modulus of 1 TPa, breaking strength of 42 N/m [8] and in plane electrical conductivity of 10^7 S/m [9]), incorporating graphene into ceramics has great potential to produce tough and electrically conductive ceramic composites which could solve a wider range of material related challenges in processing industries, aerospace, transportation and military applications [8,10–12]. Research on graphene ceramic matrix composites (GCMC) although quite promising, is still limited and unexploited.

1.1.2 Creation of ceramic microthruster

Thrusters are propulsive device used by spacecraft for orbital station-keeping, attitude control, low thrust acceleration and propulsion. As technology advances, smaller satellites are possible that require less thrust. The resulting miniature electric thrusters need low-weight and compact designs. The advent of microelectromechanical systems (MEMS) has introduced a new market with incredibly small scale designs. Using this technology with low temperature co-fired ceramic (LTCC) materials has paved way to ceramic microelectromechanical systems (C-MEMS). The advantages of ceramic materials in micropropulsion are its high mechanical strength in the fired state with

multi-layer structures, ability to withstand the harsh environment created by high temperatures and its good seal capabilities which makes it an excellent choice for devices [13–15].

These excellent properties of ceramic materials also have the potential to replace silicon which was originally developed and most commonly used in microelectronic industries. The use of silicon, a good thermal conductor as main structural material has exposed the system to excessive heat loss and consequently lower efficiency [16]. Thus, the better thermal insulation of ceramic materials has the ability to improve performance of the system over silicon based systems.

In micropropulsion systems, the term "micro" can refer to either of two things: (i) a propulsion system which delivers thrust in the order of micro-newton (μN) or (ii) propulsion system which are in the micro-metre (μm) scale [13]. The former does not have requirements on maximum size or mass and the latter can be designed to produce more or less thrust. Current microthruster delivers thrust in μN range and its components are designed in μm scale. Besides, the microthruster is based on chemical propulsion which relies on chemical reactions to create thrust; such as through combustion and decomposition of propellant.

1.1.3 Thesis outline

This thesis presents a study on both engineering and material science aspects of ceramic processing, leading to fabrication and characterization of ceramics composites. The research described in this thesis was driven jointly by the needs for further improvement on the brittleness and electrical conductivity of monolithic ceramic materials for use in micropropulsion devices.

Considering the important roles of ceramic materials in micropropulsion devices, few approaches have been proposed in this research. The thesis is divided into three sections: (i) alumina toughened zirconia (ATZ) composites, (ii) graphene toughened yttria stabilised zirconia (YSZ) composites and (iii) fabrication of C-MEMS microthruster using ATZ and YSZ-Gr composite. This thesis contains six chapters.

Chapter 1 introduces the research topic covered in this thesis. It includes the project aims, objectives and thesis structure. In the next chapter, the findings of literature review carried out on ceramic composites and ceramic microthrusters will be presented.

Chapter 2, *Literature Review* provides details about graphene, processing and properties of ceramic composites and the developments in fabrication of MEMS scale ceramic microthruster. This chapter also highlights the challenges and perspectives for future progress in application. Chapter 2 is followed by the processing of ATZ composites.

Chapter 3, *Low Temperature Synthesis, Characterization and Mechanical Properties of Alumina Toughened Zirconia (ATZ) Composites* outlines the synthesis, characterization and fabrication of ATZ composites. This chapter also demonstrates the viability of using the dispersant, Dolapix CE64 to achieve homogenous dispersion of Al_2O_3 within YSZ matrix.

Chapter 4, *Characterization, and Properties of YSZ Reinforced Graphene Ceramic Composites* further reports a completely new, novel synthesis method of producing YSZ-Gr composites by gel casting on PDMS soft molds. The mechanical and electrical properties will be analysed by varying key parameters such as filler composition, stirring duration and stirring speed. The latter part of the chapter aims to

provide a preliminary investigation of the composite material for use in space application.

Chapter 5, *Design and fabrication of ATZ-graphene based MEMS scale microthruster* is focussed on exploring the possibility to fabricate a MEMS scale microthruster using ATZ and YSZ-Gr composites. This chapter also contains details on fabrication procedure, characterization, microstructural analysis and testing of the ceramic microthruster.

Chapter 6, *Conclusion and Future Direction* summarize the main findings and conclusion with regard to the research objectives and highlight the scope for future work.

The following flowchart gives a brief information on the thesis outline (Figure 1.1).

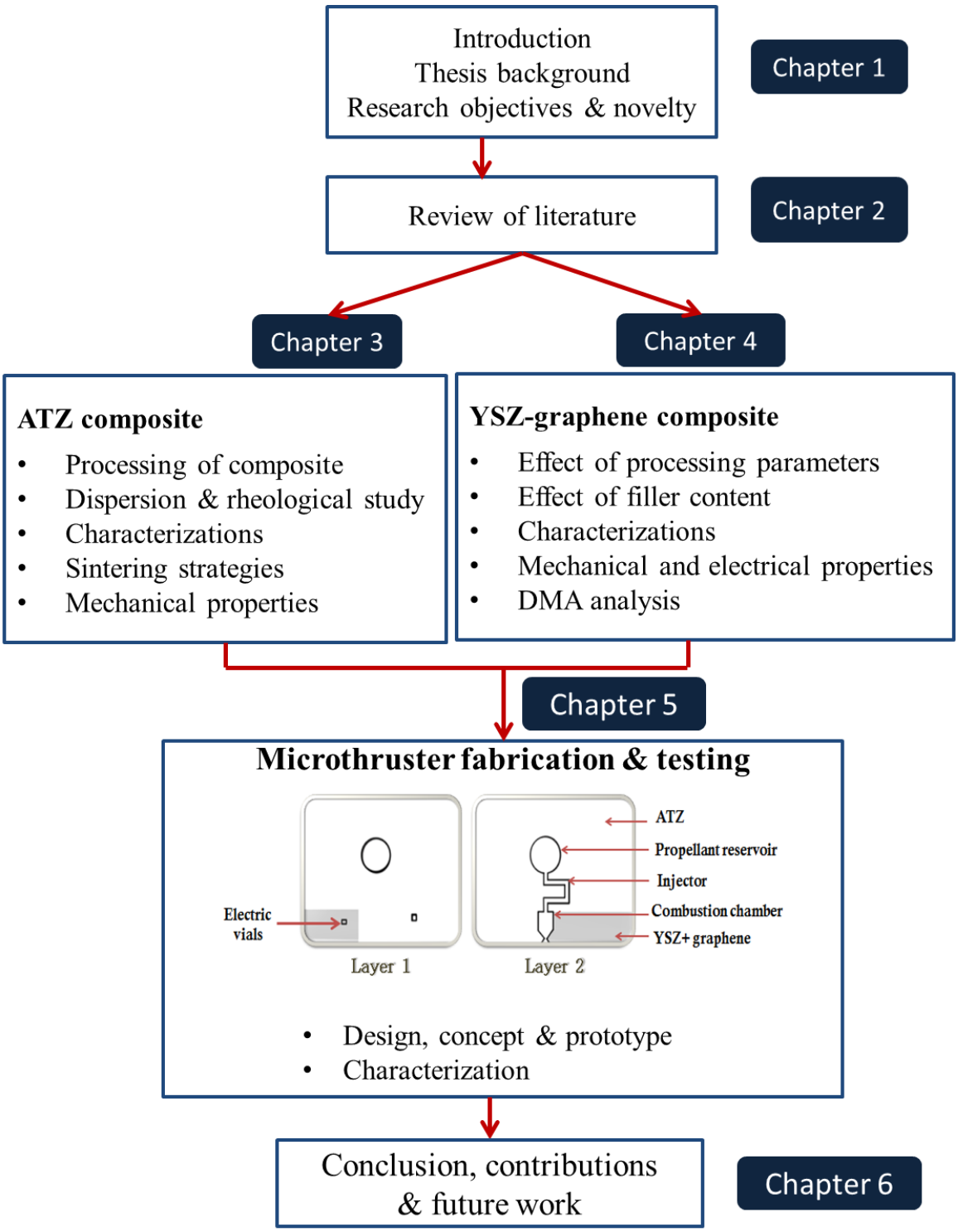

Figure 1.1: Brief representation of thesis outline.

1.2 Research objectives and novelties

The aim for this research project was to develop validated procedures for fabrication of C-MEMS scale microthruster using ATZ and YSZ-Gr composites. The main drive to develop microsystems with this technology is based on the need for smaller propulsion devices with improved functionality, higher mechanical strength and lower power consumption. Current work is divided into two major stages, i.e. material analysis and device fabrication. The four objectives of this research project are listed as below;

- To synthesize, characterize and evaluate the mechanical properties of ATZ composites.
- To optimize the processing parameters, synthesize, characterize and evaluate the properties (mechanical and electrical) of YSZ-Gr composites.
- To design and fabricate a microthruster using ATZ and YSZ-Gr composites as structural materials.
- To evaluate the performance of developed microthruster using hydroxyl ammonium nitrate (HAN) as liquid propellant.

Newly developed aqueous gel casting of ceramic suspension (ATZ and YSZ-Gr) combined with soft micromolding technique was used as the fabrication route to replicate microthruster design onto ceramic layers. As a result, prototypes of microthruster using ATZ and YSZ-Gr as structural material for the first time in micro-space literature are expected. Fabricated prototypes were characterized using scanning electron microscopy (SEM), thermal gravimetric analysis (TGA), x-ray diffraction (XRD) and fourier transform infrared spectroscopy (FTIR). The microthrusters were tested for their performance by measuring thrust produced and comparing with thrust values reported in existing literatures.

Chapter 2

Review of literature

Many products in our daily life are made of ceramics. For example, dishes, knives, resistors, bearings, turbine rotors and extrusion dies. Due to their chemical inertness and biocompatibility, ceramics are used in medical applications such as dental crowns, hip and knee prostheses and bone implants. Man kind has known the early ceramic product, pottery since 30 000 years ago [17]. From then, other ceramic products such as bricks and cements were invented and have been used to support human life. The development of furnace played a major role in improving ceramic properties and invention of new ceramics or ceramic composites. High hardness, high stiffness and chemical inertness make ceramics distinct from other materials [18]. These promising properties have triggered research on improving ceramics for wider technical applications and particularly for components operating at elevated temperatures.

2.1 Technical ceramics

Ceramic materials produced from raw material modification and refinement or even synthesized to form new ceramic materials are often called technical, advanced, engineering or fine ceramics. Technical ceramics can be classified into oxide ceramics, non-oxide ceramics and ceramic composites (Figure 2.1). Generally, oxide ceramics are oxidation resistant, chemically inert and very hard. Non-oxide ceramics can be classified based on their chemical components. Ceramic composites were invented by researchers to combine the above ceramics and achieve better properties,

i.e. alumina toughened zirconia (ATZ) or zirconia toughened alumina (ZTA) [1,7,19,20].

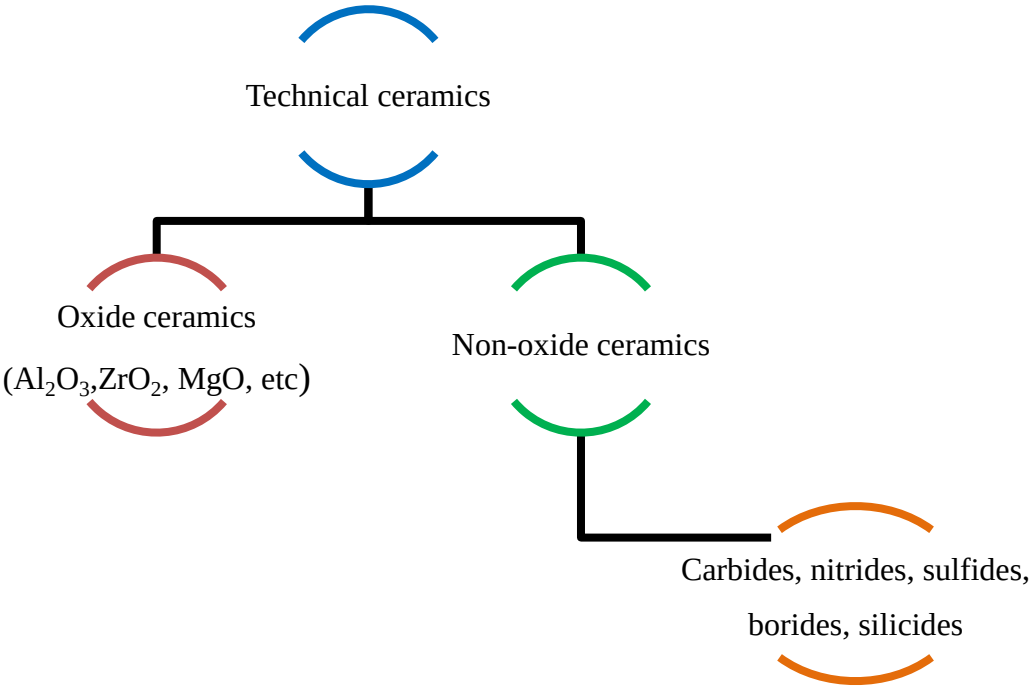

Figure 2.1: Classification of technical ceramics.

Commercially available structural ceramics like alumina (Al_2O_3) and zirconia (ZrO_2) have been used in many applications. Alumina can be found in nature as bauxite which contains hydrated alumina ($Al_2O_3H_2O$). By chemical processing, high purity (99.5 %) alumina can be obtained. Alumina ceramic is used in many products since it is relatively cheap, chemically inert and easier to produce in comparison to other ceramics [21]. Besides, a dense product (99.9 %) made of alumina can be achieved via good sintering procedure.

Zirconia (ZrO_2) has high melting temperature (2700°C) and it has three kinds of crystal structures. At room temperature, the crystal structure of zirconia is monoclinic while at 1000°C, the crystal structure transform into tetragonal and at even higher temperatures (2370°C), the tetragonal crystal transforms into a cubic shape crystal

[22]. The transformation process is accompanied by a great volume change which leads to cracks formation. However, addition of Y_2O_3, CaO or MgO into zirconia can maintain the tetragonal or cubic phase at room temperature. The high toughness properties of zirconia are attractive in many systems that operate in harsh environments. Properties of these commercially available ceramics are provided in Table 2.1.

Table 2.1: Properties of Al_2O_3 and ZrO_2 [23].

Property	Unit	Al_2O_3	ZrO_2
Fracture toughness	$MPa.m^{0.5}$	3.5	10
Young's Modulus	GPa	390	205
Density	kg/m^3	3900	6050
Hardness	GPa	22	14
Thermal shock resistance	K	200	250

2.2 Graphitic carbon nanomaterials

Carbon has various allotropes that differ in their chemical structure and material properties which range from sp^3 hybridized diamond to sp^2 graphite. The existing family of carbon allotropes was extended with the emergence of 0-dimensional (0-D) fullerene, one dimensional (1-D) carbon nanotubes and two dimensional (2-D) graphene [24–27]. Fullerenes, carbon nanotubes (CNT) and graphene are all comprised of sp^2 hybridized carbon atoms and thus designated as graphitic carbon nanomaterials (Figure 2.2). They have unique chemical structures which lead to properties (electrical, mechanical and optical) that are distinct from bulk graphitic materials and superior to graphite for certain applications. Owing to their advanced properties, these carbon nanomaterials have improved the performance in various composite matrices such as ceramic, polymer and metal [28–33].

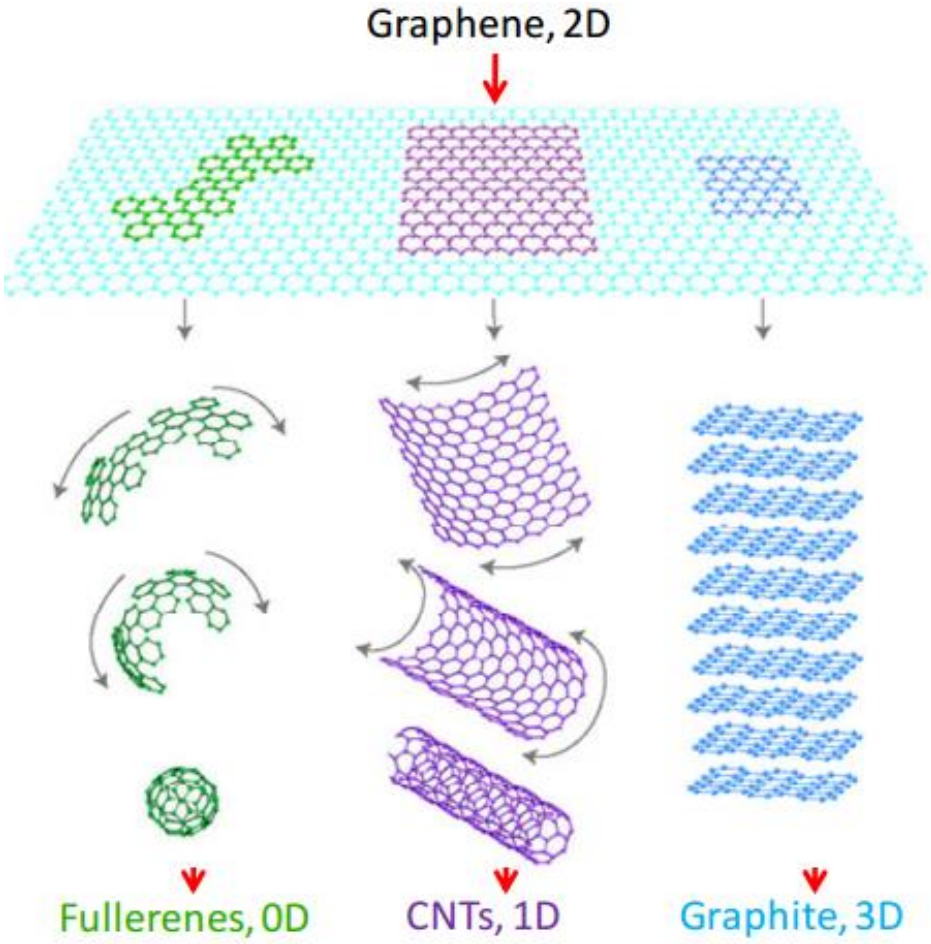

Figure 2.2: Building blocks for all graphitic form. Construction of zero dimensional (0-D) fullerene, one dimensional (1-D) CNT and three dimensional (3-D) graphite from the two dimensional (2-D) graphene (a single layer of graphite) [26].

2.2.1 Graphene

Graphene, a single layer form of graphite is a one atom thick planar sheet of sp^2 bonded carbon atoms densely packed in a honeycomb crystal lattice. The quality and quantity of work on graphene have attracted worldwide attention in the mere five-year span upon its emergence. This is ascertained by the intensity and number of publications arising from various countries in the field of graphene (Figure 2.3). In fact, by the year 2020, graphene market will rise by a Compound Annual Growth Rate (CAGR) of 60 %. As of today, research on graphene has been revolutionized in every

discipline. A total of 174,521 articles were retrieved via Web of Science search tool for the syntax string <graphene> from the year 2000 to 2015. The publication trend on graphene reveals that the amount of research on graphene has increased exponentially from 90 articles in the year 2000 to 44,648 articles in the year 2015. A refined analysis shows that the annual number of publications for graphene has been increasing dramatically and graphene's properties are likely to be exploited in the primary area of applications. In the last five years, materials science (no. of documents: 79,273) was the most researched area followed by chemistry (73,951), physics and astronomy (60,495), engineering (44,962) and energy (14,328). This indicates the importance of graphene research in various research areas across the world.

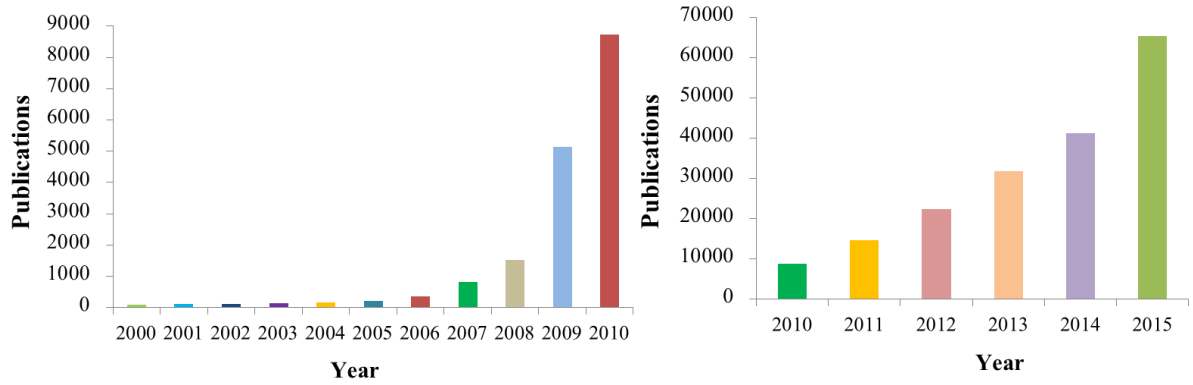

Figure 2.3: Publication trend of graphene from the year 2000 to 2015.

In view of its chemical structure, the 2s orbital interacts with the $2p_x$ and $2p_y$ orbitals to form the 3σ bonds which are the strongest covalent bond that can exist [34]. This is the source of the excellent mechanical properties of graphene. A single layer of graphene has a thickness of less than 1 nm, but despite this thinness, the theoretical Young's modulus of a single layer of graphene has been reported as 1.06 TPa [35]. Jiang et al used molecular dynamics (MD) approach to theoretically compute Young's modulus of graphene by observing the thermal vibrations [35]. They reported that

Young's modulus or stiffness of graphene is dependent on factors such as size, temperature and isotropy. The Young's modulus was found to increase from 0.7 to 1.1 TPa when the length of graphene was increased from 10Å to 40 Å. Further increase in size did not affect the Young's modulus as shown in Figure 2.4.

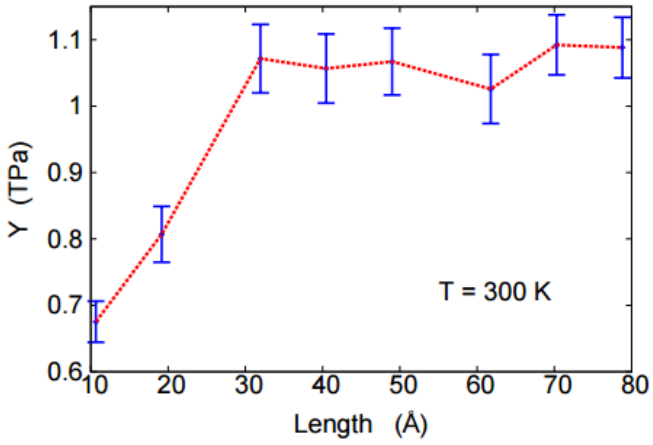

Figure 2.4: Effect of graphene size on the Young's modulus [35].

The similar group of authors also investigated the effect of temperature on Young's modulus. Upon increasing the temperature from 100 K to 500 K, the Young's modulus increased from 0.95 to 1.1 TPa as shown in Figure 2.5. Increase in temperature above 500 K resulted in a decrease of Young's modulus value. Thus, the ability to control these factors leads to the potential of tuning graphene's strength for the intended applications.

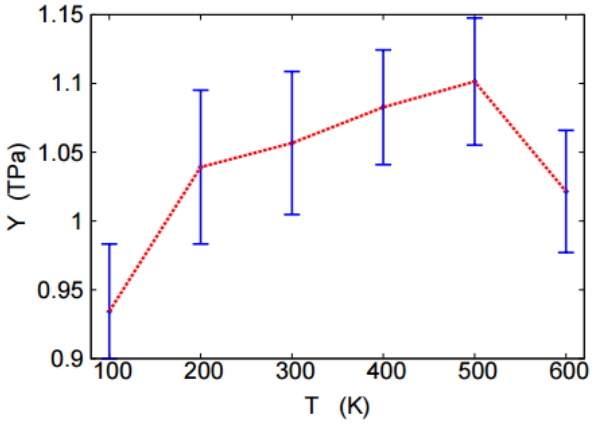

Figure 2.5: Effect of temperature on Young's modulus of graphene [35].

On the other hand, the $2p_z$ orbital is uniformly distributed between the two carbon atoms creating a π bond. The p_z electrons have very weak interaction with the nuclei which leads to graphene's enhanced electrical properties [36]. Geim et al. proceeded to measure the carrier concentration by measuring the field effect and magnetoresistance according to equations below [26];

$$\mu = \sigma(V_g) \, / enV_g$$

$$\mu = R_H/\rho$$

where μ is the carrier mobility, σ is the conductivity, V_g is the gate voltage, R_H is the Hall coefficient and ρ is the resistivity. Both experiments yielded the same values for μ which ranged from ≈15, 000 cm^2/V. s at 300 K and ≈60, 000 cm^2/V. s at 4 K. Thus, the carrier mobility is independent of absolute temperature. Amongst other characteristics, the offer of ballistic transport and linear current-voltage characteristics make graphene a viable candidate for electrical applications.

Figure 2.6 shows the TEM image of graphene sheets which resembles crumpled silk. The excellent properties of graphene alongside with its low density, high surface area, and high aspect ratio enables graphene to be a desirable material for reinforcement in composite materials. A summary of graphene properties is provided in Table 2.2.

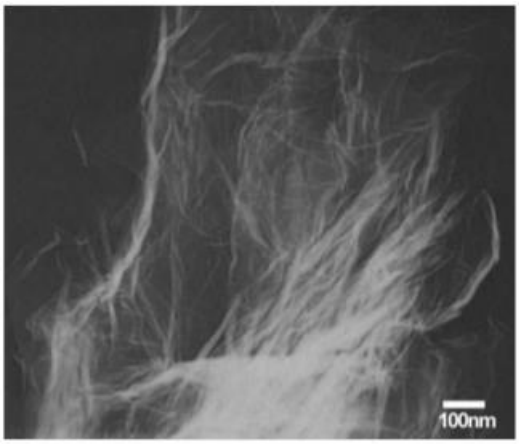

Figure 2.6: TEM image of graphene sheets [37].

2.2.2 Graphene oxide (GO)

The functionalization of graphene aims to improve the dispersibility of graphene since graphene is hydrophobic in nature [38,39]. GO is basically a wrinkled two-dimensional carbon material covered by oxygen functional groups on its basal plane and edges. These oxygen functional groups strongly affect the electrical and mechanical properties which results property differences between GO and pristine graphene.

The synthesis of GO is usually performed by Hummers or Offeman method in which graphite is treated with a mixture of sulphuric acid, sodium nitrate and potassium permanganate (strong oxidizer) [40]. More efficient methods have been developed to reach 70 % oxidisation by increasing quantities of potassium permanganate and adding phosphoric acid with sulphuric acid instead of sodium nitrate [41]. The oxidation of graphite is followed by exfoliation via sonication. The resulting GO is a sheet of graphene having covalently attached functional groups such as hydroxyl, epoxy, carboxyl and carbonyl [42,43]. The structural model of GO is shown in Figure 2.7. The physical properties of graphene and GO are similar. However, the price for graphene oxide is much lower than that of graphene, so graphene oxide is used for modification instead of pure graphene.

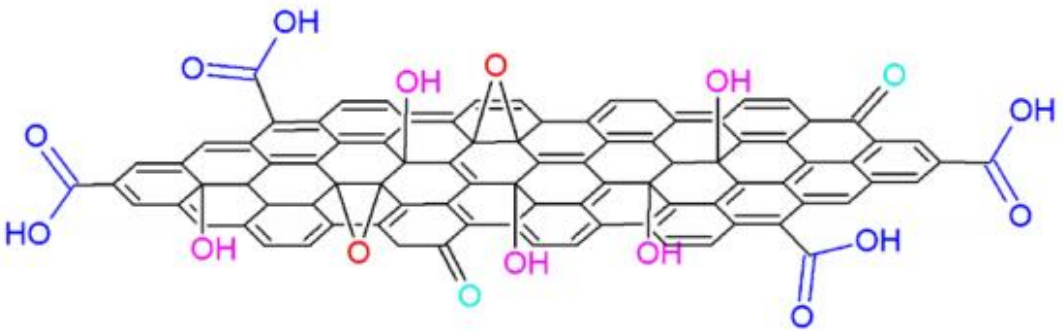

Figure 2.7: Schematic structure of graphene oxide (GO) [44].

However, GO is electrically insulating due to the disrupted sp^2 network during chemical oxidation process [45]. Hence, reduction process is carried out to recover electrical conductivity by restoring the p-network. The conductivity is usually enhanced by several orders of magnitude during the reduction process. The common reagent used for chemical reduction of GO is hydrazine as demonstrated by Stankovich et al [36]. In a typical synthesis, ≈100 mg of GO is added into a round bottomed flask containing 100 ml of water. The mixture is sonicated until a homogenous dispersion is obtained before 1 ml of hydrazine is added into the solution. The solution is then heated at 100°C in an oil bath for 24 hours. As the oxygenated groups in GO are reduced, GO loses its hydrophilicity and precipitates out of the solution. When this occurs, complete reduction is assumed to be achieved. However, hydrazine is known as a highly corrosive and flammable reducing agent which prompts to other reduction approaches. Dubin et al. employed an alternative reduction process by using solvothermal methods [46]. In this approach, N-methylpyrolidone (NMP) is refluxed with GO dispersion, yielding a colour change from homogenous light brown dispersion to black which indicates reduction of GO has taken place. This process is carried out in an oil bath held at ~240°C for 24 hours.

2.2.3 Carbon nanotubes (CNTs)

The structure of nanotubes originates from graphite. In graphite, carbon atoms sit in hexagonal patterns and form 2 dimensional sheets. Single walled nanotubes (SWNTs) can be seen as seamless cylinders rolled up from graphene. Another type of nanotube is multi-walled nanotubes (MWNTs) which are concrete cylinders of multiple graphene layers. MWNTs are larger than SWNTs. Their properties are interplays of multiple layers and typically more defective. On the other hand, SWNTs are light,

strong and stiff. The Young's modulus of nanotubes is ≈1 TPa which is five times higher than steel [47]. Theoretically predicted tensile strength of SWNTs was 130 GPa while of MWNTs was 63 GPa [48,49].

SWNTs also have remarkable electrical performances. High quality SWNTs can have mobility larger than 10, 000 cm^2/Vs and can be either metallic or semiconducting depending on their chirality. These electrical properties coupled with mechanical properties paved way to integrate SWNTs into electromechanical systems such as electrically actuated tunable oscillator [50]. The key properties of CNTs are summarized in Table 2.2.

From Table 2.2, it can be concluded that graphene has exceptional mechanical properties (Young's modulus and hardness) in comparison to other carbon materials. Besides, graphene showed many advantages for electrochemical applications due to their excellent electrical conductivity. A key electrical property of graphene is its electron mobility (the speed at which electrons move within it when a voltage is applied) which is faster than any other material. Graphene also exhibits surface area of 2630 m^2/g which is much greater than graphite (10 m^2/g), carbon nanotubes (1300 m^2/g) or graphene oxide (736.6 m^2/g). Thus, graphene precludes the problems associated with other carbon nanomaterials while out performing their properties in many ways. The present study will focus on the utilization of graphene as nanofiller in ceramic composites to produce graphene based ceramic composites (GCMC).

Table 2.2: Properties of carbon nanomaterials as reported in literatures.

Carbon allotropes	Density (g/cm^3)	Specific surface area (m^2/g)	Thermal conductivity (W/mK)	Electrical conductivity (S/cm)	Young's modulus (TPa)	Hardness (GPa)
Graphene	2.09-2.23[a]	2630	4840- 5300	2000	1.04	1.13
		[51]	[27]	[36]	[52]	[53]
Graphite	2.266[a]	10-20	1500-2000	27.78[b]	0.795	0.2-0.9
		[54]	[55]	[39]	[35]	[56]
Carbon nanotubes	>1	1300	3500	Structure dependent	0.8 ± 0.41	0.5
		[57]	[58]		[59]	[60]
Graphene oxide	0.5-1	736.6	18	Non-conducting	0.2076	NA
		[61]	[62]		[63]	
Reduced graphene oxide (rGO)	1.91	422.69 - 499.85	NA	6667	NA	NA
		[64]		[65]		

[a] The properties are provided by Graphenea S.A., Spain.

[b] The listed conductivity is the conductivity of the powder and not the intrinsic conductivity of the material.

2.3 Processing of ceramic composites

The desirable characteristics of ceramic composites depends on many factors such as phase homogeneity, fine particle size that promote sintering, equiaxed shape to enhance packing and uniform distribution of fillers within the ceramic matrix. The difficulty in fabricating composites with well controlled micro/nano-structures has been a key issue in assessing toughening mechanisms of these composites [66]. Thus, suitable processing route is critical to obtain ceramic composites with desired properties and microstructural features [67]. The following subsections present the classifications of major processing techniques to fabricate ceramic composites.

2.3.1 Powder processing

Powder processing route has been very commonly applied and were the first processing route considered in early stages in ceramic development. For example, fired clay figures appeared about 22,000 B.C in the archaeological record [68]. These figures were probably natural clay pieces shaped by hand, allowed to dry and placed in fire. This processing route is also used in modern ceramics to develop ceramic composites.

In graphene based ceramic composites, graphene is deagglomerated via ultrasonication or stirring prior mixing with ceramic mixture using ball milling. The most common dispersant for graphene are ethanol or n-methyl-2-pyrrolidone (NMP) whereas milling time ranging from 3-30 hours to produce well dispersed composites. Kun et al. synthesized fine particles of graphene and Si_3N_4 using this technique by milling in highly efficient attritor mill to form the composite [69]. The milling was performed at high rotation speed of 3000 rpm for 4.5 hours in which the graphene particles conferred a cumulative effect in improving mechanical attributes of the

composites and decreased the agglomeration quotient of graphene in the ceramics. A similar technique was demonstrated by Miranzo et al. using SiC powder and graphene, milled in ethanol for 2 hours and spark plasma sintered at a heating rate of 133°C/min under 4 Pa at 1850°C [70]. In another study, Tapaszto et al. produced Si_3N_4 composites reinforced with single walled carbon nanotubes (SWCNTs), multi-walled carbon nanotubes (MWCNTs) and few layer graphene (FLG) using attritor milling [71]. Small angle neutron scattering experiments and SEM images confirmed that graphene can be dispersed more efficiently in the ceramic matrix in comparison to CNTs. In 2014, Michalkova et al. compared homogenisation of graphene in Si_3N_4 matrix using various methods such as attritor milling, ball milling and planetary ball milling [72]. The best results were obtained for ceramic composites prepared using planetary ball milling although all composites displayed a decrease in mechanical properties compared to monolithic Si_3N_4.

Guimares et al. investigated ZrO_2–Al_2O_3 nanocomposites using powder processing approach [73]. They prepared suspensions of ZrO_2 and Al_2O_3 with 0.5 wt. % of aminobenzoic acid as deflocculant in alcohol. The two suspensions were mixed in appropriate ratios and ball-milled, followed by addition of 0.5 wt. % of oleic acid. The overall suspension was mixed further, dried and sieved. The use of deflocculants (aminobenzoic acid and oleic acid) improved dispersion of zirconia, although it was not mentioned how effective these measures were in forming stable suspensions. Daguano et al. used a similar approach in their investigation of ZrO_2–Al_2O_3 composites where powder mixtures after attrition milling for 4 hours in isopropylic alcohol have hardness and fracture toughness values of 1500 HV and 8 MPa $m^{1/2}$ respectively; that make it suitable for bio-applications such as dental implants [74].

In conclusion, powder processing route offers unprecedented opportunities to significantly reduce complexity, cost and time to synthesize ceramic composites. Besides, this technique has successfully created homogenous dispersion of second phase in ceramic composites. However, it should be noted that distribution of high surface area and high aspect ratio filler in the absence of driving force impede graphene to de-agglomerate and distribute from ceramic powder particle surface into bulk of the mixture.

2.3.2 Colloidal processing

Colloidal processing refers to the route of producing intimate dispersion of filler and ceramic matrix to produce composites with homogenous microstructure and controllable properties on the basis of colloidal chemistry. For ceramic-graphene composites, colloidal suspensions are usually used to coat graphene with ceramic particles by modifying the surface chemistry, stabilizing suspensions and reducing repulsion between graphene which facilitates homogenous dispersion of graphene throughout ceramic matrix grains [75]. It is noteworthy that dispersion of graphene is established by manipulating surface chemistry of two phases during low temperature processing; wherein this dispersion is retained even after sintering. Typically, similar solvent is preferred for both graphene and ceramic powders to ensure uniform dispersing medium [76]. Moreover, slow mixing (magnetic stirring/ultrasonication) is important to favour uniform dispersion of graphene into the ceramic matrix. Another requirement for colloidal processing is surface modification of both graphene and ceramic matrix; which is achievable via direct functionalization (i.e: oxidation) or by using surfactants that generate electric charges. In most cases, modification involves generation of charges between ceramic powders and graphene; a process known as heterocoagulation. To date, many literatures have demonstrated heterocoagulation as

a very effective route for producing well dispersed ceramic-graphene composites [75–80].

The first true study on heterocoagulation process to produce Al_2O_3-graphene composites was reported by Wang et al. in 2011 [80]. In their work, graphene oxide (GO) and alumina suspension was prepared by ultrasonication in water separately. Then, GO was added dropwise into the alumina suspension under stirring conditions. A similar technique was repeated by Centeno et al. where graphene-alumina based ceramic composites were fabricated by adding GO dropwise into alumina suspension under mechanical stirring while pH at 10 was maintained [75]. Similar to the previous studies, Fan et al. prepared Al_2O_3-GNS (graphene nanosheets) composites via colloidal processing route; where GO colloid and alumina colloid were added dropwise into each other [79]. In another study by Walker et al. Si_3N_4-graphene composites were successfully produced via colloidal processing route [77]. Cetyl trimethyl ammonium bromide (CTAB) was used as a cationic surfactant to produce positive charges on both ceramic and graphene surfaces. 1 wt. % CTAB was used to disperse both graphene and Si_3N_4 to develop electrostatic repulsive forces on the surfaces, to obtain good dispersion of graphene within the ceramic matrix. Although a variety of colloidal processing routes have been described, there is still a lack of quantitative information to precisely compare the dispersion potential of each route interms of agglomerate size to quantitatively evaluate the dispersion homogenity of various routes.

2.3.3 Sol-gel processing

Sol-gel processing route provides an alternative route to create an intimate dispersion of fillers in ceramic composites. The difference between colloidal and sol-gel processing is described in Table 2.3.

Table 2.3: Difference between colloidal and sol gel processing

Colloidal processing	Sol-gel processing
Wet chemistry precipitation process in which solutions of different ions are mixed under controlled temperature and pressure to form insoluble precipitates.	Colloidal chemistry technology. Sol-gel process consists of chemical transformation of a liquid (the sol) into the gel state and with subsequent post-treatment into solid material.

In sol-gel method, filler is dispersed in molecular precursor solution (e.g.: tetra methyl ortho silicate (TMOS)) that undergoes condensation reaction to generate green body for subsequent consolidation. Later, suspension of TMOS and filler will be sonicated to obtain a uniformly dispersed sol. Gelation is initiated by adding catalyst (e.g.: acidic water) which promotes hydrolysis and leads to formation of composite gels upon condensation at room temperature. This technique has been utilised mainly to create silica nanocomposite. For example, Watcharotone et al. prepared graphene-silica film to be used as transparent conductors, where TMOS was added to the Hummers-modified graphene oxide (GO) suspension to create a stable suspension [81]. GO (highly oxygenated graphene) was used instead of graphene since GO has good solubility in polar solvents in comparison to graphene [82]. Another work by DiMaio et al. used tetra ethyl ortho silicate (TEOS) as the molecular precursor solution to produce silica composites for non-linear optic application with low CNT content (0.25 wt. %) [83]. Although sol-gel process is ought to provide route to good dispersions, agglomeration in the precursor suspensions has been problematic [28]. Nevertheless, this technique only requires liquid precursors; which eases the

preparation of doped materials or well-dispersed composites by dissolving or suspending materials in liquid phase [84].

2.3.4 Polymer derived ceramics (PDC)

Polymer derived ceramic (PDC) route is used to produce composite materials that are difficult to be processed via conventional powder technology. In this technique, common preceramic polymers such as poly (silazanes), poly (siloxanes), and poly (carbosilanes) are processed and shaped using well established polymer forming techniques such as polymer infiltration pyrolysis (PIP), injection moulding, coating from solvent, extrusion, and resin transfer moulding (RTM) [85]. Upon processing, objects made from pre-ceramic polymers can be converted into ceramic components by heating to temperatures that are sufficient to consolidate elements in the structure into a ceramic. One of the fundamental advantages of PDC route is the versatility of the materials that can easily be shaped in form of fibres or bulk composites. Besides, PDCs exhibits excellent thermo-mechanical properties such as temperature stabilities up to 1500°C. In fact, recent studies shows that temperature stability up to 2000°C can be achieved if the preceramic polymers contains boron [86]. Furthermore, PDCs have also been considered as additive free ceramic materials that possess excellent oxidation and creep resistance. In particular, PDC technique is suitable for ceramic-graphene composites since desired dispersion of nanofiller can be produced in liquid phase precursors prior pyrolysis [87,88].

One of the earliest study utilising PDC route was reported by Ji et al. where GO was dispersed in polysiloxane (PSO) precursor liquid and SiOC followed by crosslinking and pyrolysis at 1000°C in Argon gas to produce SiOC-GNS [89]. Their results show that discharging capacity of GNS-SiOC composite was higher in comparison to monolithic SiOC because of increasing number of electrochemically active sites.

Another technique in PDC route involves the infiltration of PDC resin from solution into pre-existing fabricated ceramic green body, which was demonstrated by Cheah et al. in 2013 [90]. They first fabricated green bodies of zirconia by gel casting the ceramic suspension on PDMS soft molds. These green bodies were then infiltrated with PDC resin (RD-212a) before sintering at 1200°C. In their study, infiltration of the pre-ceramic resin into pre-sintered ceramic has successfully sealed the pores.

However, there are several concerns in using this processing route such as considerable shrinkage ratio and volume decrease due to material change and gas loss during thermal treatment [91]. Shrinkage also causes cracking while gas loss may leave poorly distributed pores behind. In some cases, retaining the as-formed shape throughout the thermal treatment stage becomes difficult since polymers become less viscous. In view of these limitations, extensive experimental or modelling data are necessary to understand how PDC route may affect the microstructural features and composition of graphene based ceramic composites.

2.3.5 Molecular level mixing

Molecular level mixing is another route used to produce ceramic composites by utilizing a molecular level mixing process. This route has been reported for graphene based ceramic composites. Functionalised graphene in a solvent will be mixed with ceramic salt; which was then converted into ceramic particles by heat treatment or other processing methods [52,92]. This route enables molecular level coating of ceramic particles with graphene. In 2014, Lee et al. reported molecular level mixing to produce Al_2O_3-GO composite with different wt.% of GO [92]. In their study, GO was dispersed in distilled water by sonication to form a GO suspension. Alumina nitrate precursor salt ($Al(NO_3)_3.9H_2O$) was added and stirred for 12 hours by magnetic stirring. The solution was then vaporised at 100°C and dried powders were

oxidised at 350°C hot air to produce alumina particles. The powder was further processed by ball milling for 12 hours to obtain well dispersed Al_2O_3-GO powders. In the first stage, aluminium nitrate was thermally decomposed to Al^{3+} ions while hydroxyl and carboxylic groups present on the surface of GO react with Al^{3+} ions at the molecular level. This results in heterogeneous nucleation of Al ions on GO surface. Coating of Al^{3+} ions on surface of GO avoids agglomeration of GO flakes. Interestingly enough, the authors examined Al-O-C bonding via FT-IR analysis and interface area of reduced Al_2O_3-GO matrix using TEM analysis; which are strong evidences of molecular level mixing process. Due to the characteristic microstructure, the GO-alumina composite shows enhanced strength, hardness and fracture toughness superior to monolithic. The schematic representation for fabricating reduced GO-Al_2O_3 composite by molecular level mixing process is depicted in Figure 2.8. The key advantages of this processing route are the excellent dispersion of graphene in the ceramic matrix and good interfacial bonding of ceramic-graphene at molecular level. As a consequence of good interfacial bonding between ceramic matrix and graphene, molecular level combination of the two components (ceramic & filler) necessary to enhance property of the composite may be relatively easier to achieve.

Previous works on ceramic composites were mostly based on conventional powder metallurgy route; resulting in lower than expected mechanical properties since graphene is prone to agglomeration due to van der Waals forces [80]. Besides, sol-gel process have been proven to disperse graphene within ceramic matrix, however; interface between graphene and ceramic matrix were not strong [83]. Therefore, although molecular level processing remains to be explored in detail, it is nonetheless plausible to claim that this route is the most promising process to obtain homogenous dispersion of graphene and strong interfacial strength.

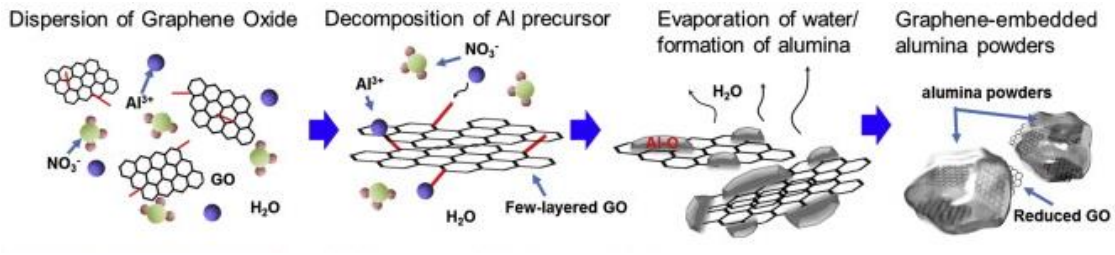

Figure 2.8: Schematic representation for fabricating reduced GO-alumina composite by molecular level mixing process [92].

2.4 Compaction and consolidation

2.4.1 Spark plasma sintering (SPS)

SPS is considered a relatively new; high temperature-low dwell time powder consolidation technique successfully implemented to create fully dense ceramics [93–95]. SPS involves simultaneous application of pressure and electric current through a graphite die containing ceramic powders to be sintered. The pulsed current assists in densification of ceramics via creep mechanism; unlike conventional sintering techniques that relies on diffusion and mass transport phenomena across grain boundaries during long periods of dwelling time. In particular, SPS has been useful for investigating the sintering behaviour of carbon based fillers (graphene) reinforced ceramic composites; since isothermal conditions can be achieved rapidly enabling densification to be studied over wide range of densities [96].

Other key advantages of SPS technique is the in-situ reduction of GO to graphene in a single step without additional steps and alignment of graphene in host matrix [75]. Centeno et al. used Raman spectroscopy to ascertain the alignment of graphene in alumina matrix during SPS [75]. Results show that I_D/I_G ratio (the ratio of D and G peaks) was higher for sample surface perpendicular to pressing direction (I_D/I_G =1.13) than the sample surface parallel to pressing direction (I_D/I_G =0.83). Typically, the I_D/I_G ratio in Raman spectra can be used to quantify defects in graphene. Figure 2.9 shows

the Raman spectra of composites taken at different directions. The percentage of graphene surface exposed to Raman scans were considerably higher in orientation parallel to the pressure direction applied in SPS leading to a higher Raman intensity; while in the perpendicular orientation the percentage of the graphene surface exposed to the measurement were considerably low.

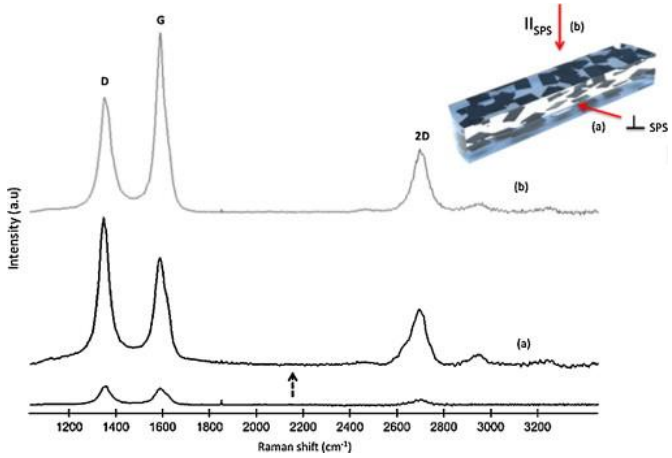

Figure 2.9: Raman spectrum of the Al_2O_3 –graphene composite at two different orientations: (a) perpendicular to pressure direction applied in SPS (b) parallel to pressure direction applied in SPS [75].

An et al. produced alumina nanopowder by electrical explosion of wires and sintered the samples using spark plasma sintering at 40 MPa and temperatures of 1400°C, 1500°C and 1600°C respectively [97]. The authors reported that increase in sintering temperature leads to higher density of sintered alumina nanopowder where relative density increased from 78.44 to 98.21 %. A highly dense ceramic indicates minimal porosity and increased mechanical strength of the composite. In a more recent study, Bartolome et al. prepared ATZ composites via CO_2 laser co-vaporization [98]. During subsequent spark plasma sintering, the zirconia defect structures and transition alumina phases transformed to homogeneously distributed tetragonal ZrO_2 (52.4 vol. %) and α-Al_2O_3 (47.6 vol. %), the ceramics were completely dense with average grain

sizes of 250 nm and has outstanding mechanical properties (flexural strength of=1500 MPa, fracture toughness K_{ic}=6.8 MPa $m^{1/2}$).

2.4.2 High-frequency induction heat sintering (HFIHS)

HFIHS focuses on sintering ceramics over very short sintering times (<2 min) through the simultaneous application of induced current and high pressure (Fig 2.10). Role of the current in HFIHS is two-folded; (i) intrinsic contribution of current to mass transport and (ii) fast heating attributed by Joule heating at contact points. The composites produced via this technique were fairly dense; with relative density as high as 96 %.

Kim et al. produced Al_2O_3-ZrO_2 composites with two types of yttria stabilized zirconia: 3 mol. % and 8 mol. % yttria doped ZrO_2 (3 YSZ and 8 YSZ); where the composites were consolidated very rapidly to full density by HFIHS [99]. The authors reported that 3YSZ is more effective as a second phase toughening filler than 8YSZ. Besides, Al_2O_3-3YSZ composites with higher mechanical properties and small grain size were successfully developed at relatively low temperatures through this sintering technique.

In 2015, Kwon et al. demonstrated that HFIHS can also be used to sinter and densify ZrO_2-graphene ceramic composites [100]. Recently, Ahmad et al. reported similar sintering technique (HFIHS) in processing conditions of 1500°C sintering at 60 MPa and 3 min holding time which produced Al_2O_3-graphene composites with near theoretical densities (> 99 %) [101]. While this sintering technique is not earth shattering; it is still plausible as it represents a new sintering approach to that of SPS. By careful modification or optimisation of the process parameters, it may be possible to push the relative density values to near 100 % by increasing the heating rates. The

challenge is to avoid property deterioration of filler (graphene) within the ceramic composite and in an economical approach.

2.4.3 Flash sintering

A more recent technique of sintering ceramics is via flash sintering. It occurs when electrical field is applied to a heated ceramic compact. At critical combination of field and temperature, power surge ("flash event") resulting in sintering completion in few seconds [102]. The growing interest in flash sintering arouse after publication from Cologna et al. in 2010 [103]. In their study, an initial voltage was applied to zirconia powder compact whilst it is slowly heated in a conventional furnace. At 850°C, "flash event" occurs and over a few seconds specimens are sintered to near full density. This finding was explained by local Joule heating of grain boundaries, in which on one hand promotes grain-boundary diffusion (kinetic effect) and simultaneously restricts grain growth (thermodynamic effect). The smaller grain size and higher temperature at grain boundaries work synergistically to enhance rate of sintering. In a recent study, Grasso et al. used flash sintering to sinter ZrB_2 ceramics [104]. The ceramic was densified up to 95 % in 35 seconds under an applied pressure of 16 MPa. In comparison to conventional SPS technique, the newly developed flash sintering resulted in unprecedented energy and time savings of approximately 95 % and 98 % respectively.

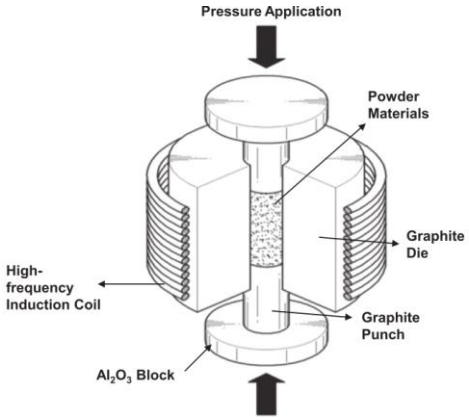

Figure 2.10: Schematic representation of the equipment for HFIHS [100].

2.5 Material properties

2.5.1 Alumina-zirconia composites

A composite material is the way to improve reliability and lifetime of ceramic materials by providing higher fracture toughness and mechanical strength. Therefore, this section attempts to summarize the main mechanical properties of alumina-zirconia composites reported in literature.

The essential idea behind toughening mechanisms in alumina-zirconia composites is to increase the energy needed to extend a crack. The basic mechanisms are crack deflection, crack bridging and transformation toughening. Claussen et al. was one of the first to investigate the alumina-zirconia system [105]. According to Claussen, fracture toughness of a ceramic can be increased by a second phase dispersion. The increase in fracture energy is attributed to the interaction of crack with the second phase and energy-absorbing mechanisms such as crack deviation and crack front elongation. Green et al. used alumina as the matrix and zirconia as the filler and reported that alumina experienced grain growth during sintering which caused porosity and exaggerated (or abnormal) grain growth [106]. The introduction of second phase (zirconia) controlled the grain growth of alumina and promoted

sintering kinetics which led to a fully dense ceramic. Naglieri et al. prepared alumina-zirconia composite by surface modification of commercial alumina with aqueous solutions of zirconium chloride [107]. The authors reported that this technique produced composites with desired alumina-zirconia ratio and strictly tailored microstructural features such as zirconia grain size and distribution. Besides, incorporation of 10 vol. % zirconia increased fracture toughness of the composite from 2.7 $MPam^{0.5}$ to 3.5 $MPam^{0.5}$. Table 2.4 summarizes the mechanical properties of alumina-zirconia composites reported in literature.

Table 2.4: Mechanical properties of alumina toughened zirconia (ATZ) and zirconia toughened alumina (ZTA) composites.

Matrix	Filler composition (wt.%)	Mechanical properties			Ref
		Hardness (GPa)	Fracture toughness ($MPa^{\frac{1}{2}}$)	Flexural strength (MPa)	
ZTA	20.2*	-	5.88±0.14	720	[108]
ZTA	50.0	14.73	4.82	-	[109]
ZTA	18.0	8	5	-	[110]
ZTA	14.4*	15.3	4.8	570	[111]
ATZ	3.0	17.0±0.3	4.2±0.2	-	[112]
ATZ	43.6*	11.5	-	931	[113]
ATZ	20.0	-	5.2	-	[20]

(*when loading was reported in volume percent, the density of alumina (3.95 g/cm^3) and zirconia (5.68 g/cm^3) were used to convert to a weight percent loading)

2.5.2 Ceramic-graphene composites

2.5.2.1 Toughening and mechanical properties

The intensity of reinforcement effects depends solely on interfacial bonding of ceramic-graphene and graphene dispersion throughout the ceramic matrix. Toughening mechanism proposed in graphene reinforced ceramic composites are

crack deflection due to load transfer, crack bridging and graphene pull-outs. All these mechanisms are crucial to be microstructurally characterized for fruitful discussions.

In 2013, Centeno et al. reported that 0.22 wt.% of graphene loading in alumina prepared by colloidal method has led to 50 % increment in fracture toughness; due to crack bridging phenomena [75]. In other work by Dusza et al. 1 wt.% Si_3N_4-graphene composites by hot isostatic pressing were prepared; in which the hardness and fracture toughness of composites reinforced with different types of graphene (multilayer graphene, exfoliated GNP and GNP) were compared [114]. Authors reported that graphene platelets induced porosity leading to lower hardness and fracture toughness values in comparison to composites reinforced with multilayer graphene.

In a similar vein, Kun et al. prepared and characterized Si_3N_4 based nanocomposites reinforced with different amounts of carbon reinforcement in the form of multilayer graphene, graphene nanoplatelets and nano-graphene platelets [69]. The results were in good agreement with Dusza et al. where graphene platelets induced porosity in samples leading to lower bending strength and module of elasticity values in comparison to composites reinforced with multilayer graphene. Most of the studies on graphene based ceramic composites have shown toughening mechanisms originated from pull-outs, crack deflection, crack branching and crack bridging (Fig 2.11 and 2.12).

Ramirez et al. discussed the toughening mechanism in Si_3N_4-graphene using a well-established model for reinforcement in ceramic composites [115]. The assumptions made were (i) GNP/GO were aligned in direction perpendicular to pressing direction in SPS (ii) graphene in ceramic matrix are in residual tension die to mismatch in thermal expansion coefficient of Si_3N_4 and graphene (iii) since graphene are in

residual tension in Si_3N_4 matrix, fracture toughening due to graphene pull-out were not considered. This assumption is contradictory to experimental evidence; where many authors reported improvement in fracture due to graphene pull-out [116–118]. The improvement in toughness due to failure of graphene in wake zone was evaluated using Eq.2.1;

$$\Delta G_c = 2f\int_0^{t=S} tdu + \frac{4f\Gamma_i\, d}{(1-f)R}$$

$$= \frac{fS^2R[(\lambda_1+\lambda_2(^d/_R)^2-(E_F{}^{e_T}/_S)^2(\lambda_3+\lambda_4(^d/_R))^2}{Ef(\lambda_1+\lambda_2(^d/_R))} + \frac{4f\Gamma_i\, d}{(1-f)R} \qquad \text{[Eq.2.1]}$$

where f is filler volume, S is the strength of filler, R is the filler radius, E_f is the elastic modulus of fiber, e_T is the misfit strain and Γ_i is the interface fracture energy. λ_i coefficients depend on filler volume fraction and ratio between fiber and elastic modulus of fiber. The first term in the equation is attributed to toughening due to crack bridging while the second term is associated with debond surface energy. The authors converted the toughness data to critical strain energy release rate (G_c) using the expression $G_I = \frac{K_I{}^2}{E}$ and compared to data plotted using equation above. Experimental and theoretical data for GNP composites were found to be in good correlation. Crack bridging is the dominant toughening mechanism in Si_3N_4-GNP composites. However, crack bridging becomes invalid for high loading of graphene due to formation of 3-dimensional inter-connected network of GNP which controls failure of composites.

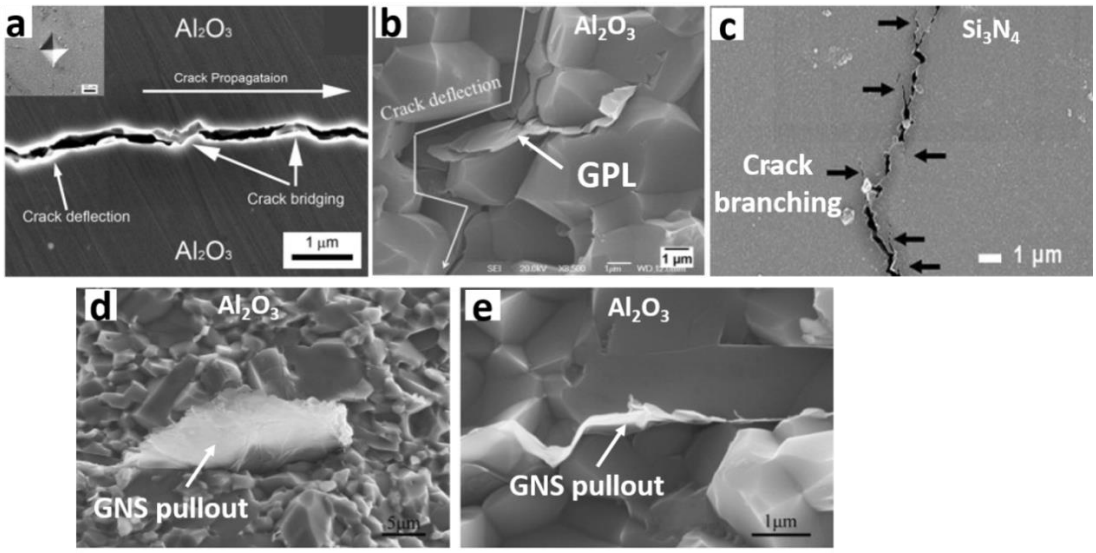

Figure 2.11: Various toughening mechanisms in graphene based ceramic composites (a) crack deflection and bridging [101] (b) crack deflection [119] (c) crack branching [117] (d) and (e) GNS pullouts [116].

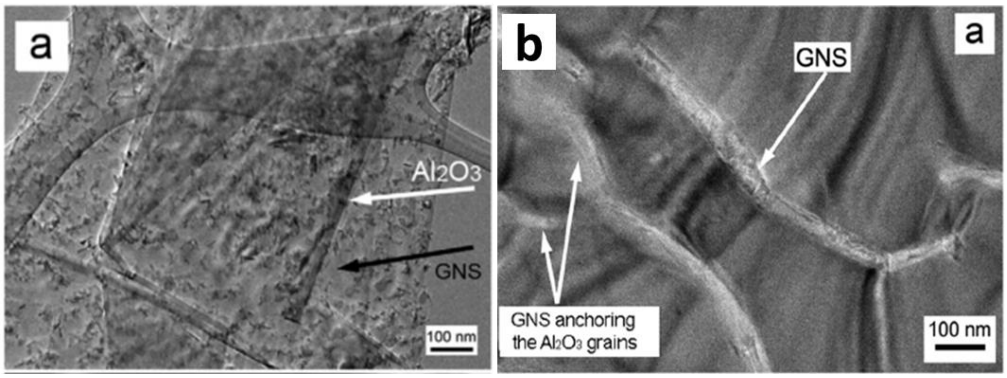

Figure 2.12: TEM images representing (a) distribution of Al_2O_3 nanoparticles over graphene nanosheets (GNS) and (b) GNS anchoring interaction with the base matrix grains [101].

Some promising mechanical results were reported in a work by Walker et al. where an improvement of 235 % in fracture toughness with only 1.5 vol.% loading of GNS in Si_3N_4 matrix via aqueous colloidal processing method [77]. Some unexpected toughening mechanisms were observed for these composites. For example, cracks

were not able to propagate through graphene walls and arrested. Thus, cracks were forced to deviate around the graphene sheets. This toughening mechanism is comparatively new in contrast to previous observation. A relatively new approach to incorporate graphene into a ceramic composite was reported by Porwal et al. where Al_2O_3-graphene composite was prepared using liquid phase exfoliation of graphene and dispersed them dropwise into Al_2O_3 matrix via ultrasonication and powder processing route, resulting in 40 % increment in fracture toughness with only 0.8 vol.% graphene [120]. The aforementioned processing route appears advantageous as it solves the problem of producing good quality graphene without affecting its properties compared to Hummer's method. A breakthrough however came in a recent work by Yazdani et al. where Al_2O_3 nanocomposites reinforced with hybrid GNTs (graphene nanoplatelets (GNP) and CNTs) prepared via a combination of wet dispersion and probe sonication technique, fracture toughness increased from 3.5 $MPam^{0.5}$ to 5.7 $MPam^{0.5}$ at hybrid addition of 0.5 wt.% GNP and 1 wt. % CNTs respectively [121]. This was accompanied by improvement in strength from 360 MPa to 424 MPa. The improvement was due to the CNTs attached to GNP surfaces and edges during mixing process, which assisted in deagglomeration and homogenous dispersion within the matrix. Toughening mechanism was attributed to the change in fracture mode from inter-granular in monolithic Al_2O_3 to blurry and glaze-like trans-granular mode in Al_2O_3 reinforced graphene composites.

Another study by Kim et al. compared mechanical properties of Al_2O_3 reinforced with unoxidized graphene, GO and reduced GO respectively [122]. Their findings suggest that the best results were obtained for unoxidized Al_2O_3-graphene composites. The improvement in mechanical properties were related to less defect concentration in unoxidized graphene flakes; ≈48 % in fracture toughness, ≈28 % in flexural strength,

and ≈95 % in wear resistance. Crack bridging was considered as key toughening mechanism in the ceramic composite. They also investigated the effect of graphene size (≈100, 20, and 10 μm respectively) on fracture toughness of Al_2O_3 - graphene composite. The best results were obtained for graphene flakes with lateral size of ≈20 μm. Graphene flakes of ≈100 μm produced structural defects in ceramic composite while toughening mechanisms such as crack bridging were less dominant when smaller flakes (≈10 μm) were used.

In an ideal situation, external load applied to ceramic-graphene composites should be transferred to graphene, allowing them to take major share of the load. The efficiency of load transfer depends on interfacial bonding of ceramic and graphene. In nanofiller reinforced ceramic, high strength of reinforcing fillers is important because once matrix crack is initiated; load will be transferred from matrix to fillers during crack initiation. If matrix-fillers adhesion is weak, initiated crack will be deflected along the matrix-filler interface, leaving the fillers intact; thus toughening the composite material. However, if matrix is too strong, matrix crack penetrates through the ceramic particles resulting in brittle composites as exemplified by monolithic ceramics [87].

It should also be noted that in almost all studies; mechanical properties of graphene reinforced ceramic composites do not show proportional improvement with increasing graphene content. The reasons for this phenomenon are two-folded; (i) increase in porosity with increasing graphene content and (ii) overlapping/ agglomeration of graphene. Pores acts as fracture initiation sites upon indentation load. Upon agglomeration of graphene; more pores are likely to be formed between agglomerated graphene platelets and ceramic matrix interface. The presence of these pores inevitably reduces contact area of ceramic matrix with graphene platelets and initiates

cracks in which stresses are released in an inefficient way. For example, if a crack propagates and meets the graphene platelets, it is arrested and deflected in plane. Such mechanism creates a complex pathway to release stress which helps to increase toughness of ceramic composite [118]. In the presence of pores, contact area of graphene and ceramic is reduced. Besides, pores weaken the interfacial friction during graphene pull-out from the ceramic matrix. As such agglomeration of graphene platelets leads to degradation of graphene toughening mechanisms in their host matrix [72]. Table 2.5 summarizes mechanical properties of graphene based ceramic composites reported in literatures.

Table 2.5: Effect of graphene addition on mechanical properties of ceramic composites.

Matrix	Optimum filler composition (wt. %)	Mechanical properties				Ref.
		Flexural strength (MPa)	Youngs Modulus (GPa)	Hardness (GPa)	Fracture Toughness ($MPa^{\frac{1}{2}}$)	
Si_3N_4	7	740	-	-	-	[72]
Si_3N_4	1	-	-	16.38±0.48	9.92±0.38	[117]
Si_3N_4	1	-	-	16.4±0.4	9.9±0.3	[123]
Si_3N_4	1	876±53	-	12.2±0.1	8.6±0.4	[124]
Si_3N_4	3	-	-	15.6±0.2	4.2±0.1	[125]
Si_3N_4	0.03*	-	290±4	-	6.6±0.1	[115]
Si_3N_4-ZrO_2	1		-	16.4±0.4	9.9±0.4	[126]
Al_2O_3	1	440	-	17	5.7	[121]
Al_2O_3	0.2	542	-	-	6.6	[116]
Al_2O_3	0.5		-	≈18.5	5.7	[101]
Al_2O_3	0.45*	-	373	21.6±0.55	3.9±0.13	[120]
Al_2O_3-3YTZP	1.1*	-	373.9±3.1	23.5±0.3	-	[78]
Al_2O_3-ZrO_2	0.43*	-	-	16.13±0.53	9.05±55	[118]
ZrB_2	4	219±23	-	15.9±0.84	2.15±0.24	[76]
YSZ	1.63*	-	-	10.8	5.9	[127]

(*when loading was reported in volume percent, the density of bulk graphite (2.2 g/cm^3) was used to convert to a weight percent loading)

2.5.2.2 Electrical properties and percolation threshold

Volume conductivity higher than 10^{-10} S/cm for electrically conducting composites is classified as an important group of relatively inexpensive materials for a range of engineering applications [128,129]. From virtually the moment graphene was discovered it is expected to display superlative electrical and thermal properties by analogy to graphite. It had been long known that graphite had an in plane electrical conductivity of 10^7 S/m and thermal conductivity of 5300 W/mK [9,27]. Thus, graphene is expected to be in a class of their own in terms of high electrical and thermal conductivities.

Electrically conducting behaviour of ceramics with conducting fillers such as graphene can be explained using the percolation theory (Figure 2.13). It is a condition that refers to the critical filler content where electrical conductivity increases significantly to several orders of magnitude due to the formation of continuous electron/ conducting paths. Electron paths do not exist below the percolation transition range; thus concentration of conducting filler must be above the percolation threshold in order to achieve conducting networks in the ceramics. Electrical conductivity experiences saturation plateau when multiple electron paths exist above the percolation transition range. This phenomenon can be explained by the change in nano-filler concentration based on the scaling law [Eq.2.2];

$$\sigma_c = \sigma_o(\emptyset - \emptyset_c)^t \qquad \text{[Eq. 2.2]}$$

where $\emptyset_c$ and σ_o are the conductivity of composite material and nano-filler (graphene) respectively. $\emptyset$ is the volume fraction of graphene, $\emptyset_c$ is the percolation threshold and t is the universal critical exponent revealing the dimensionality of the conducting system. In comparison to systems with spherical (graphene agglomerates)

conducting fillers, the onset of percolation in fibre or "stick like" (flakes and platelets) systems takes place at a lower ∅ of conducting filler [130]. Even at low filler concentrations, graphene fillers may be in direct contact with each other owing to their high aspect ratios. This results in macroscale conductive pathways through the entire ceramic composite. For uniformly dispersed particles, ∅ for onset of percolation threshold decreases with increasing aspect ratio (L/D) of graphene [131].

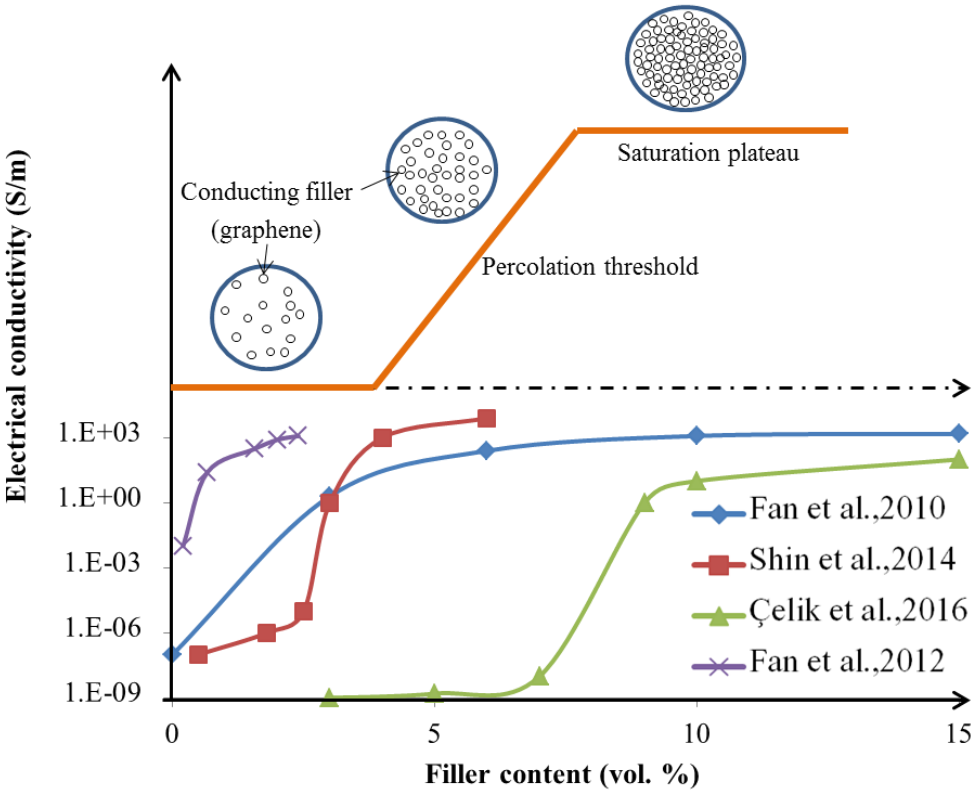

Figure 2.13: Electrical conductivity and percolation phenomenon as a function of filler volume fraction in graphene based ceramic composites [79,127,132,133].

One of the earliest studies on percolation threshold for graphene reinforced ceramic composites was carried out by Fan et al. in year 2010 [132]. Al_2O_3-graphene composites were prepared by spark plasma sintering with 0-15 vol. % graphene.

They demonstrated that percolation threshold for the ceramic composite was at 3 vol. %. The electrical conductivity increased with graphene loading; reaching a value of 5709 S/m for 15 vol. % graphene. The increase in conductivity was explained by the increase in number of charge carriers across the composites.

In later study by Fan et al., colloidal processing was used for preparation of well dispersed GO and alumina composite powders, where GO was reduced to graphene via SPS processing [79]. This study has improved upon their previous study with threshold of 0.38 vol. % lower than 3 vol. % reported previously. The electrical conductivity was 1000 S/m for only 2.35 vol. % loading of graphene. A breakthrough, however came when the hall coefficient reversed its sign from positive to negative; with increasing graphene loading revealing a change in major charge carrier. This was ascertained by measuring value of Seebeck coefficient, which also changed from positive to negative. The improvement in electrical conductivity was attributed to good dispersion and high quality of graphene whereas the positive Hall coefficient was due to doping of graphene by the alumina matrix. In another study by Centeno et al., low percolation thresholds of 0.22 wt. % witnessed increase in conductivity up to 8 orders of magnitude in comparison to unreinforced alumina [75]. The authors reported that increase in graphene loading above percolation threshold resulted in electrical conductivity increase which was due to increase in intersheet connections along the graphene planes.

Electrical conductivity of an insulator/ conductor binary mixture (σ_m) can also be expressed as a function of filler volume fraction (V_h) by the general effective media (GEM) [134];

$$\frac{(1-V_h)(\sigma_l{}^{1/t}-\sigma_m{}^{1/t})}{\sigma_l{}^{1/t}+A\sigma_m{}^{1/t}}+\frac{V_h(\sigma_h{}^{1/t}-\sigma_m{}^{1/t})}{\sigma_h{}^{1/t}+A\sigma_m{}^{1/t}}=0 \; where \; A=\left(1-V_{h,c}\right)V^{-1}{}_{h,c} \qquad \text{[Eq. 2.3]}$$

where σ_l and σ_h are the conductivities of the low and high conductivity phases, respectively, $V_{h,c}$ is the percolation threshold. The exponent *t* is a parameter dependent on shape and orientation of filler. Thus, *t* can be treated as phenomenological parameter typical of conductivity of a given composite [134]. GEM equation is advantageous over conventional percolation threshold model owing to the data analysis close to percolation threshold. Ramirez et al. studied the effect of GPL loading above their percolation threshold (12 wt.% and 15 wt.%) on the electrical conductivity via conductive scanning force microscopy and GEM equation [135]. They reported that graphene concentration was directly proportional to the conductivity of ceramic composite. In addition, electronic response and final microstructure of the composite was due to the stiffness and aspect ratio that leads to self-orientation of GPL and lying on *a-b* plane during SPS. Besides, highly anisotropic nature of graphene reinforced ceramic composites lead to differences in transport activation energy which determines the different current values measured under the same conditions for parallel and perpendicular orientations. In 2012, the group of researchers extended their study using Si_3N_4 matrix reinforced with up to 20 vol.% graphene platelets [136]. They reported electrical conductivity of 40 S/cm with the preferential orientation of graphene platelets in the ceramic matrix. In the direction perpendicular to the SPS pressing axis, electrical conductivity was an order of magnitude higher than that in the parallel direction. The authors also reported percolation threshold in the range of 7-9 vol. % relying on the direction of conductivity measurement. In their study, different mechanisms of charge transport were reported for different directions such as variable range hopping mechanism in perpendicular direction and metallic type transition in parallel direction.

In 2014, Shin et al. fabricated fully densified YSZ ceramics reinforced with reduced GO by spark plasma sintering [127]. GO was reduced to graphene thermally during SPS processing. They reported a threshold value ≈2.5 vol. % which was comparable to that observed in graphene-Al_2O_3 composite produced by Fan et al. The electrical conductivity of the composite increased drastically reaching maximum conductivity of ≈12 000 S/m at 4.1 vol. % GO addition. The significant improvement in electrical conductivity of the composite was due to the effective distribution of GO and interconnected electron pathway. Figure 2.14 shows the electrical conductivities as a function of graphene loading.

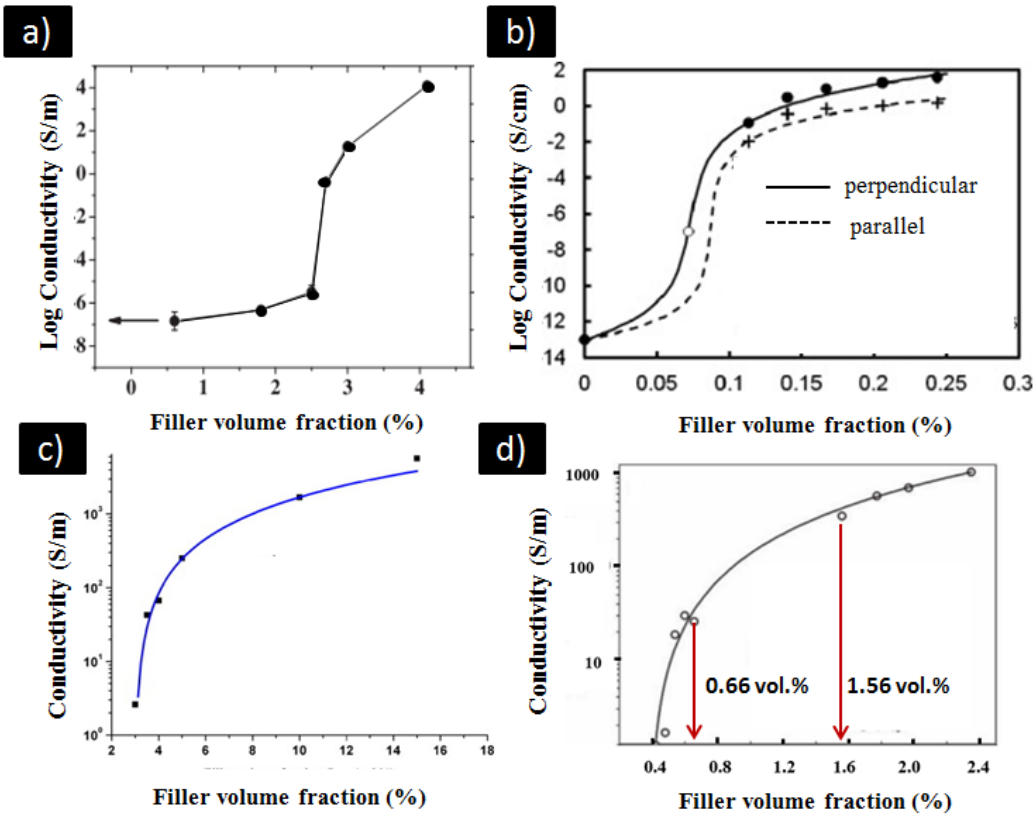

Figure 2.14: Electrical conductivity as a function of filler volume fraction of (a) GO - YSZ [127] (b) GNP-Si_3N_4 [136] (c) GNS-Al_2O_3 [132] and (d) FLG-Al_2O_3 [79] composites.

Kwon et al. used high-frequency induction-heated sintering (HFIHS) to introduce graphene as a reinforcing agent in ZrO_2 ceramics [100]. The electrical conductivity of the ceramic composites increased with amount of graphene as depicted in Figure 2.15 and was 1000 times higher (3 wt. %) in comparison to monolithic ZrO_2. This improvement was attributed to good dispersion and high quality of graphene. Table 2.6 summarizes the electrical properties of graphene reinforced ceramic composites reported in literature to date.

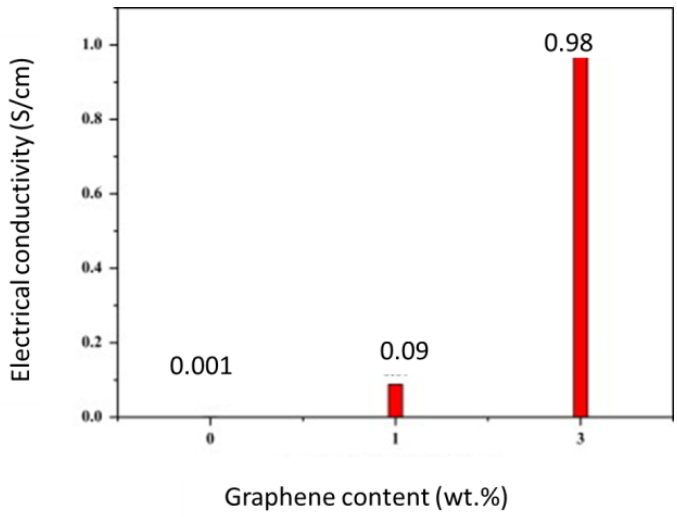

Figure 2.15: Electrical conductivity of ZrO_2 and ZrO_2 reinforced graphene composites sintered by HFIHS [100].

Table 2.6: Electrical properties of graphene based ceramic composites as reported in literature.

Matrix material	Nanofiller type	Nanofiller content (wt. %)	Percolation threshold	Electrical conductivity (S/cm)	Ref.
Al_2O_3	GO reduced to graphene chemically	2	N/A	1.72	[80]
Al_2O_3	GO reduced to graphene chemically	0.16, 0.22 and 0.45	0.22	8 orders magnitude higher than monolithic Al_2O_3	[75]
Al_2O_3	GO reduced to graphene thermally	1.32*	0.38	10	[132]
Al_2O_3	Graphene platelets	8.95*	3	57.09	[79]
Al_2SiO_5	N-doped graphene sheets	N/A		6.9341	[137]
Si_3N_4	Graphene nanoplatelets	12 and 15	> 4.4	N/A	[135]
Si_3N_4	Graphene nanoplatelets	2.6 to 17.6*	7-9	40	[138]
SiC	Few layer graphene (FLG)	2.8*	N/A	1.02	[70]
YSZ	GO reduced to graphene chemically	1.53*	2.5	120	[127]
ZrO_2	Graphene platelets	3	N/A	0.98	[100]

(*when loading was reported in volume percent, the density of bulk graphite (2.2 g/cm^3) was used to convert to a weight percent loading)

2.6 Recent developments in fabrication of ceramic microstructures

In recent years, the demand to achieve extremely low levels of thrust in different space missions has increased. Smaller size of spacecraft has attracted much interest owing to their low cost and short lead times. Microscale thrust is also required when size of spacecraft is reduced to tens of kg. Therefore, the use of micro-electromechanical system (MEMS) based propulsion has many benefits with advancements in microfabrication technique that allow thrust in micro-Newton range. Besides, their construction is extremely light weight and small in volume thus reducing overall mass of the propulsion system.

Ceramic materials such as alumina, mullite, silicon carbide and zirconia are promising materials in MEMS manufacturing. They are preferred in high temperature applications owing to their very high melting point. Table 2.7 compares the melting points of silicon- the most common structural material for various microsystems and various types of ceramic, which are used in harsh environments such as in reactive atmospheres, which makes them suitable choices for chemical microthrusters [139].

Table 2.7: Comparison of melting points between silicon and ceramics.

Structural material	Melting temperature (K)
Silicon	1690
Alumina	2070
Mullite	2110
Zirconia	2980

The two common technologies for ceramic MEMS microthrusters are low-temperature co-fired ceramics (LTCC) and high temperature co-fired ceramics (HTCC). For LTCC, the firing temperature is below 1000°C whereas for HTCC the firing temperature is around 1600°C. In co-fired ceramic devices, each layer can be processed differently and assembled to form a final structure. This research focusses on LTCC fabrication route. In this route, ceramic green tapes were first prepared by conventional tape casting technique [140]. They were then patterned on the green tapes using either laser machining or micro-punching. Integration of heating elements or conductive paths into the micro-systems is carried out via screen-printing of conductive paste on tapes. Finally, the green tapes were laminated and co-fired at a relatively low temperature to form ceramic micro-components such as microthruster. Figure 2.16 shows a LTCC microthruster.

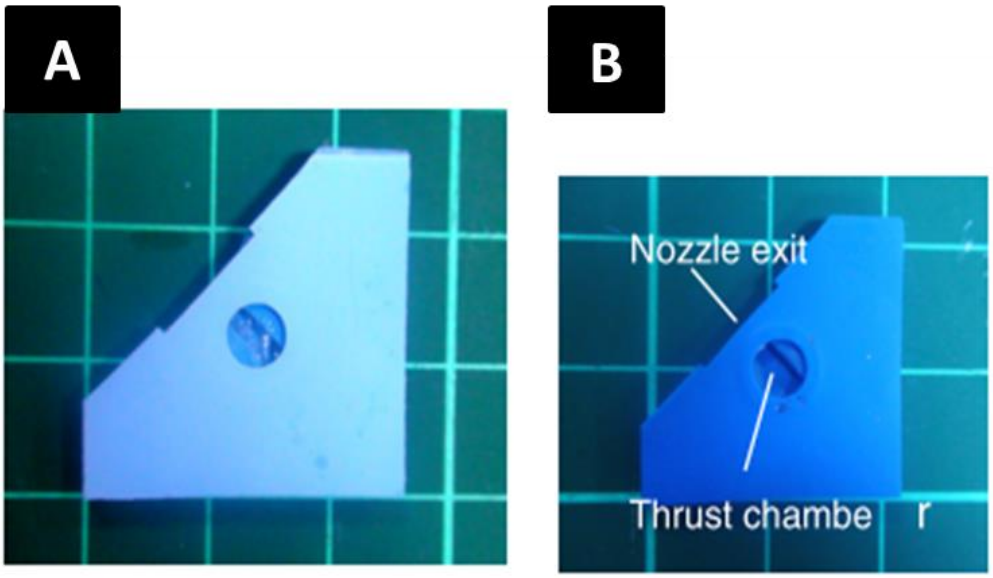

Figure 2.16: Bi-propellant LTCC microthruster (a) before and (b) after co-firing [140].

LTCC technology which requires no expensive equipment and complicated fabrication steps was adapted to develop mono-propellant [90,141–143] and bi-propellant microthrusters [140]. The better thermal insulation of LTCC tapes has improved the performance of the systems over silicon-based systems as reported by Zhang et al. [143]. However, since the maximum servicing temperature of LTCC tapes are limited to 1200 K, HTCC technology have been adapted for the development of high-performance micropropulsion systems that operate at higher temperatures (Figure 2.17). For example, Cheah et al. fabricated a vaporizing liquid microthruster (VLM) via HTCC technology using zirconia as the structural material [16]. It is widely recognized for its superior thermal-mechanical properties such as good mechanical strength and fracture toughness, low thermal conductivity and exceptional thermal shock resistance which make it appealing for the development of chemical micropropulsion systems.

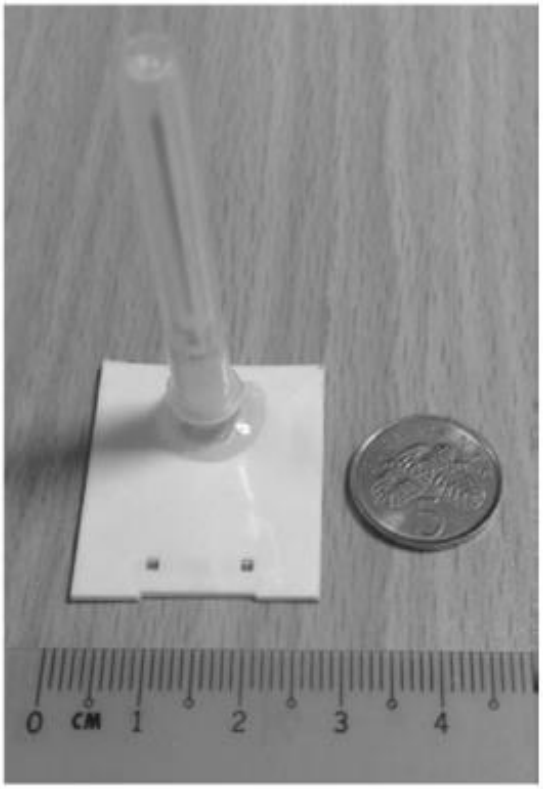

Figure 2.17: Vaporizing liquid HTCC microthruster in comparison to a Singaporean 5 cent coin [16].

Through LTCC and HTCC routes, various MEMS scale ceramic microthrusters such as mono-propellant, bi-propellant, cold gas and vaporizing liquid microthrusters were fabricated and tested. Table 2.8 summarizes the various ceramic microthrusters, their advantages and disadvantages as reported in literature.

Table 2.8: The various ceramic microthrusters reported in literature.

Thruster type	Material	Advantages	Disadvantages	Ref.
VLM	Zirconia Silicon carbide (SiC)	• A single VLM can be used for several times depending on quality of valve and volume of fuel storage.	• VLM consumes more electric energy to vaporize liquid propellant.	[16] [144]
Mono-propellant	Alumina	• Lower system complexity.	• Lower specific impulse than a bipropellant thruster.	[90][142][15]
Bi-propellant	Alumina	• Bipropellant rockets cover the range of higher thrust & higher total impulse missions. • Ability to be restarted and high thrust-weight ratio.	• Power consumption for pumps and valves. • Necessary cooling system to avoid high temperature. • Proper mixing of propellants.	[140]
Cold-gas	Zirconia	• Low complexity of their subsystems. • Well suited for mass-critical applications.	• Relatively low efficiency or specific impulse (Isp).	[13]

2.7 Conclusions

In conclusion, progress has been made in using ceramic composites for micropropulsion devices over the last decade. The excellent mechanical and electrical properties of graphene render a huge potential for structural and functional applications of graphene-ceramic composites such as surface renewable electrodes [145], low temperature fuel cells [65], energy storage materials [146], hip-joint prosthetics [147] and electronic devices [148]. In this chapter, an overview of current research in ceramic composites is provided with focus on carbon nanomaterials, processing of ceramic composite as well as the recent developments in fabrication of ceramic microthrusters. Thus, from the review on recent literatures it was identified that gel casting route of homogenously dispersed ceramic suspension on PDMS soft mold will be the most feasible route to replicate the geometries and hence fabricate a microthruster.

Chapter 3

Low temperature synthesis, characterization and mechanical properties of alumina toughened zirconia (ATZ)

3.1 Introduction

Zirconium materials have witnessed significant interest in the scientific community over the past decade since it has comparable toughness to stainless steel. In particular, tetragonal yttria stabilized zirconia (YSZ) ceramic has attracted major attention due to the possibility of fabricating nano-grained bulk ceramic with controllable microstructure and enhanced mechanical properties. The mechanical behaviour of this material is because of its tetragonal to monoclinic phase transformation and regimes of heat treatment to achieve full densification of ceramics [149]. However, similar to many ceramic materials YSZ is brittle and susceptible to fracture due to flaws induced during fabrication process. In addition, with high thermal expansion coefficient and low thermal conductivity, YSZ is also known to be thermal-shock sensitive [150]. As such, much effort has been done to incorporate other materials within YSZ to produce ceramic composites of high structural reliability.

Within this context, Al_2O_3 has been known to improve strength and fracture toughness of YSZ with promising applications for dental implants, knife blades and constructions [151–155]. YSZ reinforced with alumina particles are known as alumina toughened zirconia and denominated as ATZ. Up to date, several studies on ATZ have been reported and in most cases, powder processing or colloidal processing route were utilized [150,152,153,156,157]. The effective utilization of

Al_2O_3 in ceramics depends on the ability to disperse Al_2O_3 homogenously throughout the matrix; thus achieving strong interfacial bonding of Al_2O_3 with the ceramic element. Herein, we report the synthesis of ATZ via gel casting on polydimethylsiloxane (PDMS) soft molds. The main motivation to choose gel casting route was the ability of this technique to form complex shapes. Besides, gel casting technique has rapidly turned into a high research target in ceramic forming field due to high strength, high density, low cost and machinable property of the formed ceramic green bodies. To the best of our knowledge, synthesis, characterization and mechanical properties of ATZ produced by gel casting on PDMS soft molds have never been reported in open literature.

In the first section of this chapter, the need of dispersant (Dolapix CE64) to achieve homogenous dispersion of Al_2O_3 within YSZ matrix will be studied. The results obtained from this study will be used to synthesize, characterize and evaluate mechanical properties of ATZ composite. Characterization is done by thermogravimetric (TGA), fourier transform infrared spectroscopy (FTIR), x-ray diffraction (XRD) and scanning electron microscopy (SEM). The mechanical properties (hardness and toughness) of the composite were evaluated by varying the amount of alumina in YSZ.

3.2 Experimental Procedure

3.2.1 Materials and reagents

The PDMS prepolymer and its curing agent was obtained from Sylgard 184, Dow Corning, U.S.A. The high purity α-alumina and yttria stabilised zirconia (YSZ) used in this investigation was procured from ABSCO Materials, UK (Figure 3.1). The detailed properties of these materials are summarized in Table 3.1. Methacrylamide (MAM) and N, N-methylenebisacrylamide (MBAM) were purchased from Fisher

Scientific (U.S.A) with 99 % purity. Glycerol was used as plasticizer and purchased from Sigma Aldrich (U.S.A). PDC resin (RD-212a) which was used to seal the pores of sintered ceramics was obtained from Starfire Systems Inc, (U.S.A). Ammonium persulphate (APS, 99 %, Merck) was used as the free radicals to initiate polymerization whereas N, N, N', N'-tetramethyl ethyldiamine (TEMED, 99 %, Merck) was used as the catalyst to accelerate rate of polymerization. Dolapix CE64 (Zschimmer & Schwarz, Germany) which is a carbonic acid based polyelectrolyte without foam development and free from alkali was used as a dispersant. The specifications given by the manufacturer are listed in Table 3.2.

Table 3.1: Properties of YSZ and Al_2O_3 powder.

Powder characteristics	YSZ	Al_2O_3
Average particle size (μm)	1.5	0.1
Specific surface area (m^2/g)	16	7.9
Density (g/cm^3)	6.52	3.9
Isoelectric point (IEP)	5.4	9.1

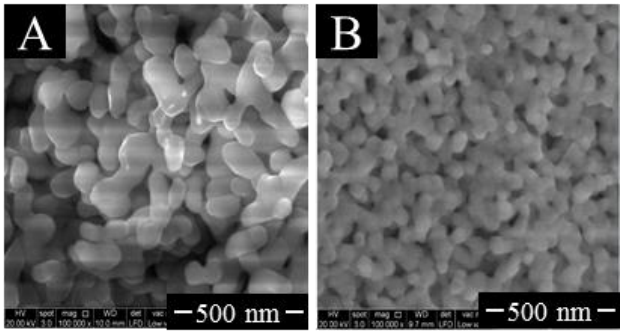

Figure 3.1: SEM images with magnification of 100 000X of as-received (A) YSZ and (B) Al_2O_3 powder.

Table 3.2: Characteristics of Dolapix CE64 (provided by manufacturer).

Property	Characteristic
Appearance	Yellowish liquid
Active matter	≈ 65 %
Solubility	Water miscible
pH	≈ 7

3.2.2 Fabrication of ceramic composites

3.2.2.1 PDMS soft mold preparation

PVC rigid sheets of 0.2 mm thickness were stacked onto each other using adhesive tapes to form master mold with dimension of 2.5 cm (L) x 2.5 cm (W) x 0.3 cm (H). Mixture of PDMS prepolymer and its curing agent was prepared at ratio 10:1, poured onto the PVC master mold and kept inside a vacuum desiccator for degassing to ensure gas bubbles removal. It was then heated at 80°C for 2 hours and the cross-linked PDMS that replicated the dimension from the master mold was peeled off and ready to be used as soft mold. An illustration for the PDMS soft mold preparation is shown in Figure 3.2.

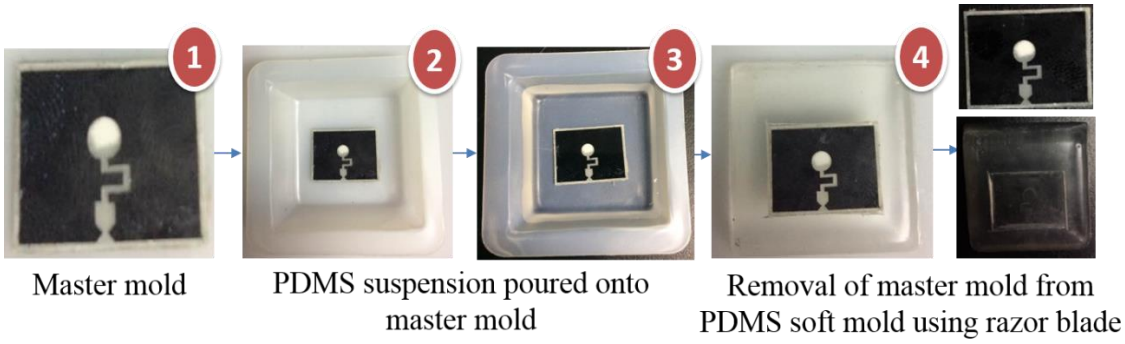

Figure 3.2: Flowchart for preparation of PDMS soft mold from master mold.

3.2.2.2 Gel casting of ceramic suspension

ATZ ceramic composites were prepared according to the procedure illustrated in Figure 3.4. The pre-mixed aqueous solution was prepared using the monomer and cross linker (MAM and MBAM) at a ratio of 6:1. The compositions of additives for gel casting on PDMS soft molds and variation in composition of ceramic powders (YSZ and Al_2O_3) are depicted in Table 3.3. It is important to ensure that all additives as listed in Table 3.3 were dissolved into the pre-mixed solution prior addition of YSZ and Al_2O_3.

In the present study, gel-casting (acrylamide based) was used as the ceramic forming technique. Ceramic particles were dispersed homogenously in aqueous solution of monomer and cross-linker. MAM is of low toxicity, low cost and able to form stiff gel. Then, free radical-initiated polymerization immobilized the particles into desired shape (Figure 3.3). Ammonium persulfate (APS) is used as the initiator which is decomposed into free radicals;

$$(NH_4)_2 S_2O_8 \longrightarrow 2NH_4^+ + 2SO_4^-$$

Adding catalyst, tetramethylethylenediamine (TEMED) promotes decomposition of persulfate into free radical and thus increases rate of polymerization. Subsequent reaction between free radicals and acrylamide monomer molecules forms monomer free radicals (by breaking C=C double bond), which continously combine with other monomer molecules to produce long polymer chains. The two C=C double bonds in crosslinker, MBAM provide anchoring sites where long polymer chains are bridged together to form 3 dimensional network. Figure 3.4 and 3.5 show the schematic representation for preparation of ATZ green body and an illustartion of gel casting process.

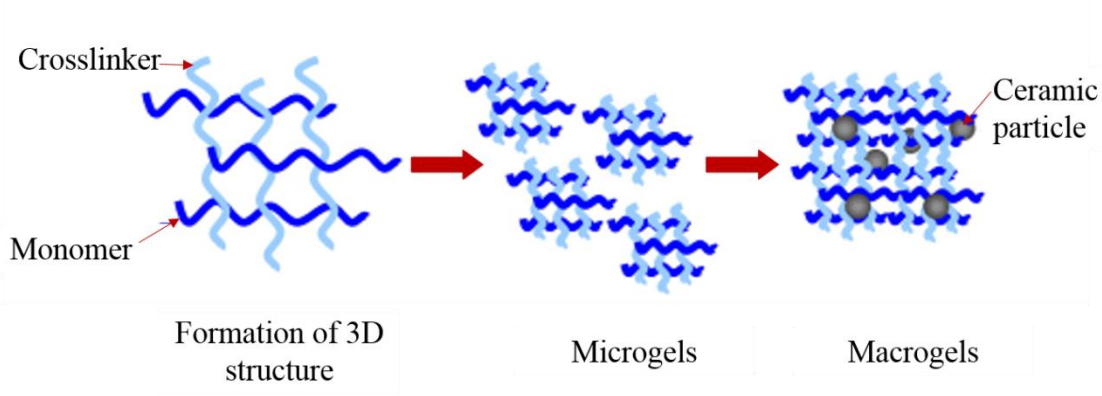

Figure 3.3: Schematic representation of gel formation.

Table 3.3: Compositions for preparation of ATZ suspension by gel casting.

Material	Purpose	Composition (wt. %)
Yytria-stabilized Zirconia (YSZ) Alumina (Al_2O_3)	Structural material Reinforcing material	70.38
Methacrylamide (MAM)	Monomer	2.46
N,N-Methylenebisacrylamide (MBAM)	Cross linker	0.41
Water	Medium for dispersion	16.31
Dolapix CE64	Dispersant	0.64
Polyvinylpyrolidone	Anti-polymerization inhibitor	1.80
Glycerol	Plasticizer	8.00

Powder	YSZ	Al_2O_3
Particle size	1.5 µm	100nm
Composition (wt. %)	100	-
	65	35
	80	20
	90	10
	-	100

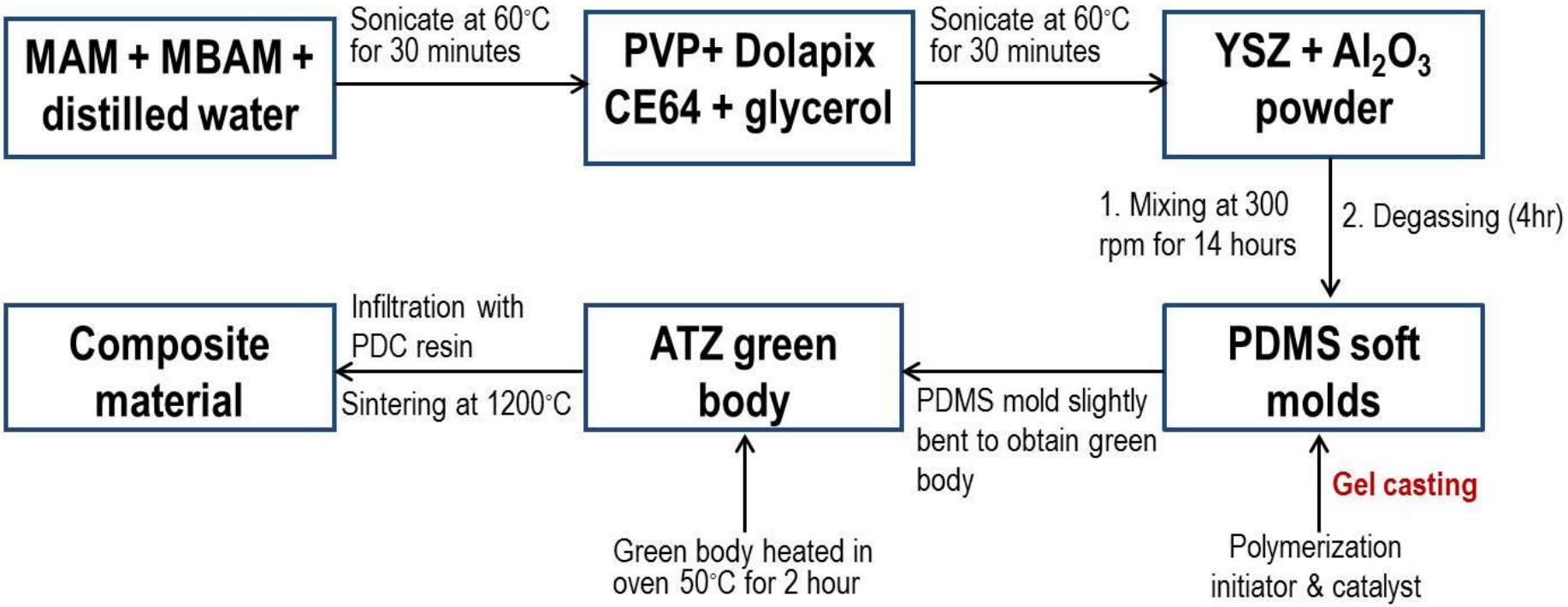

Figure 3.4: Schematic representation for preparation of ATZ via gel casting and further curing with PDC resin.

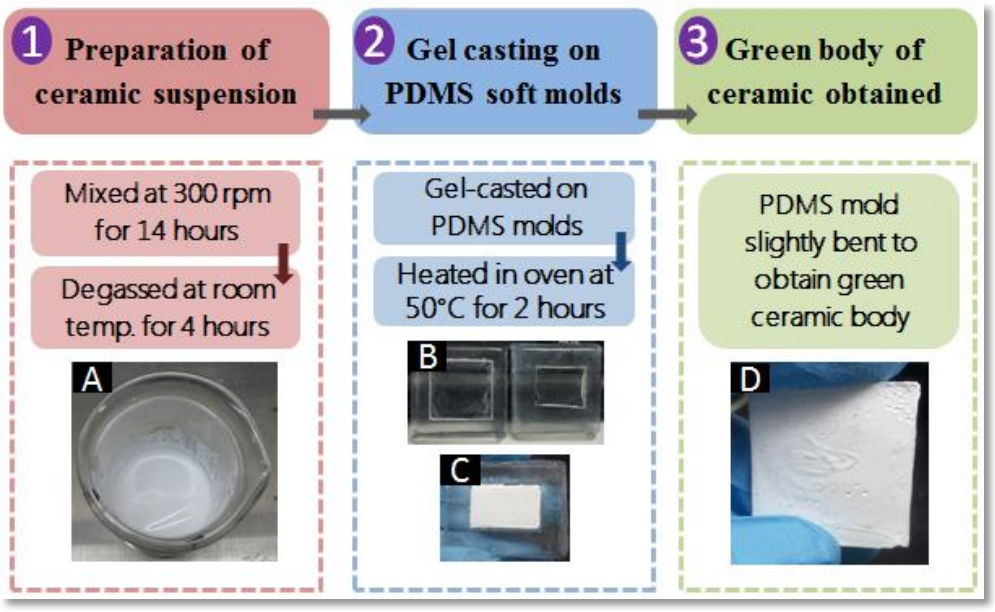

Figure 3.5: Flowchart of ATZ green body synthesis process with steps 1, 2 and 3 marked in circles (A) ceramic suspension after 14 hours of mixing and 4 hours of degassing (B) PDMS soft mold (C) PDMS soft mold gel-casted with ceramic suspension (D) green body of ATZ obtained by slightly bending PDMS soft mold.

3.2.3 Characterization techniques

All YSZ and Al_2O_3 suspensions prepared for zeta potential and rheological characterizations were free of monomer, cross-linker and initiator to prevent contamination. 70 wt. % solid loading ceramic suspensions added with different concentrations (0.3 wt. %, 0.6 wt. % and 0.9 wt. % based on weight of powder) of Dolapix CE64 was prepared in distilled water. Zetasizer 2000 (Malvern Instrument Ltd.) was used to measure the zeta potential of YSZ and Al_2O_3 suspensions as a function of pH, adjusted by adding diluted NaOH and HCl solutions. 10 readings were taken for each sample and the average was reported in this study with the standard deviation of 0.5 mV. Meanwhile, the rheological properties of the ceramic suspension were measured using Brookfield LVDV-II + Pro viscometer (Brookfield, US) at constant temperature of 28°C. Viscosity measurements were carried out as a

function of shear rate at different wt. % of the dispersant. Particle size analyser (Malvern Instrument Ltd.) was used to measure the particle size of YSZ and Al_2O_3 before and after sonication.

Characterizations were also performed on the ceramic composites. The polymer to ceramic transformation of the composite was investigated by means of thermogravimetric analysis (TGA, Mettler Toledo TGA/DSC 1, STAR* System), using <15 mg of samples in Nitrogen (N_2) atmosphere at flow rate and heating rate of 10 ml/min and 10°C/min respectively. All the ATZ composites were also investigated by means of Fourier Transform Infrared Spectrometry (FT-IR, Perkin Elmer Spectrum 2000) by potassium bromide (KBr) pellets. The spectrometer was operated at 50 scans/cm resolution within the range of 4000 to 400 cm^{-1} for each sample. All FT-IR spectra were recorded in absorbance unit. The analyses were performed by preparing a pellet from mixture of ATZ composite and KBr in the proportion of 1:20 and pressed to 5 tonnes for one minute in preparing the pellet. The accuracy of the measurement is ±4 in 4000 to 2000 cm^{-1} and ±2 in 2000 to 400 cm^{-1} region. Specific areas and pore volume of the samples were measured by BET method (Micromeitics model ASAP 2020) whereas the phases were determined by X-ray diffraction (XRD, Panalytical X'Pert Pro equipped with X'Pert HighScore Plus system) using Cu-Kα radiation (ʎ=0.15418 nm).

Vickers indentation (HVS-50Z-Digital Vickers Hardness Tester, China) was performed using a load of 9.81 N for measuring the hardness. The morphology of the samples were then analysed by scanning electron microscopy (FEI Quanta-400FESEM, U.S.A) as depicted in Figure 3.6. A minimum of six data points were averaged for each sample. Fracture toughness was calculated according to Anstis equation [158];

$$K_{IC} = 0.016(\frac{E}{H})^{0.5}\frac{P}{C^{1.5}} \quad \text{[Eq. 3.1]}$$

where, c is the crack length from centre of indentation imprint (m), E is the elastic modulus (GPa), H is the hardness (GPa) calculated from indentation load, P. Microstructural observations and fracture surfaces of samples were performed by SEM operating at 20 kV. Energy Dispersive X-Ray (EDX) microanalysis (Oxford Instruments X-Max, 20 mm^2 detector) was performed to detect the presence of silicon (Si).

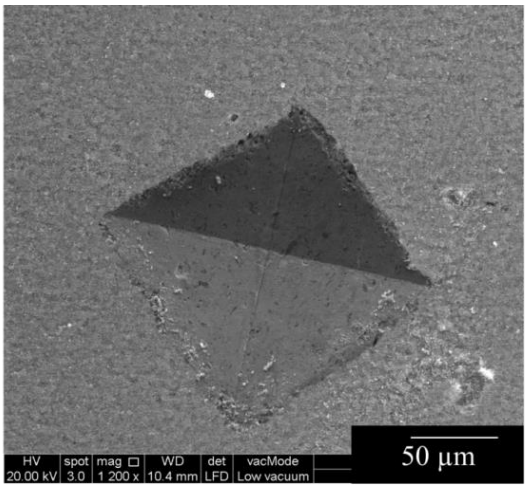

Figure 3.6: SEM micrograph of the Vickers indentation impression on ATZ composite.

The bulk density of all samples was determined via Archimedes method using a pycnometer (Laborglass, Germany). Porosity of the ceramics was determined using Eq. 3.3;

$$Porosity = \left[1 - \left(\frac{\rho_{bulk}}{\rho_{theoretical}}\right)\right] x\ 100\ \% \quad \text{[Eq. 3.3]}$$

where ρ_{bulk} is the bulk density of the ceramic composite (g/cm^3) and $\rho_{theoretical}$ is the theoretical density of the ceramic composites (g/cm^3). A contact angle goniometer (Model 250, Rame-Hart) was used to measure the contact angle between the deionized water droplets and sintered ceramic surface. The drop of deionized

water was placed on the surface of ceramic surface and oriented in such a way that the instrument's crosshair was tangent to the cross-sectional curvature of the drop. The angle between crosshair and base of drop was recorded as Young's contact angle. The measurements from imaging parameters were taken immediately after the drop was released to detect the penetration of deionized water into ceramic surface; which was used to record volume reduction of water droplets on ceramic surface over time. Morphology of the composites fabricated via different sintering mechanisms were investigated using high-resolution SEM (SEM, Quanta400F, FEI).

3.3 Results and discussion

3.3.1 Dispersion studies and processing of alumina toughened zirconia (ATZ) composites using Dolapix CE64

Dispersion of aqueous colloidal system is often achieved via control of charge on the particles by various means such as pH alteration or adsorption of charged polyelectrolytes. The proper dispersion (stability) of an aqueous colloidal system can be achieved by generating like charges of sufficient magnitude on the surface of the ceramic particles. When the particles have the same charge, dispersion occurs due to electrostatic repulsion between them. The most practical way of maintaining a stable dispersion is through the use of a chemical stabilizer called a dispersant. These dispersants are polyelectrolyte surfactants, which adsorb on the surface of the particles and modify the surface charges and electrostatic forces. The primary property of dispersant is their ability to disperse fine particles and stabilize the dispersion.

3.3.1.1 Particle size distribution

The particle size distribution of YSZ and Al_2O_3 were measured individually before and after sonication. The result in Figure 3.7 shows sonication could effectively break down the initially weak and agglomerated structures. For YSZ, the initial particle diameter of 2.26 µm was reduced to 1.3 µm upon sonication. Similarly, particle diameter of Al_2O_3 was reduced from 0.41 µm to 0.15 µm after sonication. Although both are in good agreement with the values provided by the manufacturer (ABSCO Materials, UK); particle size analysis indicates that agglomerates could not be completely broken down by dispersion in water and sonication. Therefore,

addition of chemical stabilizer such as Dolapix CE64 is desirable to prevent agglomeration and produce homogenously dispersed ceramic particles.

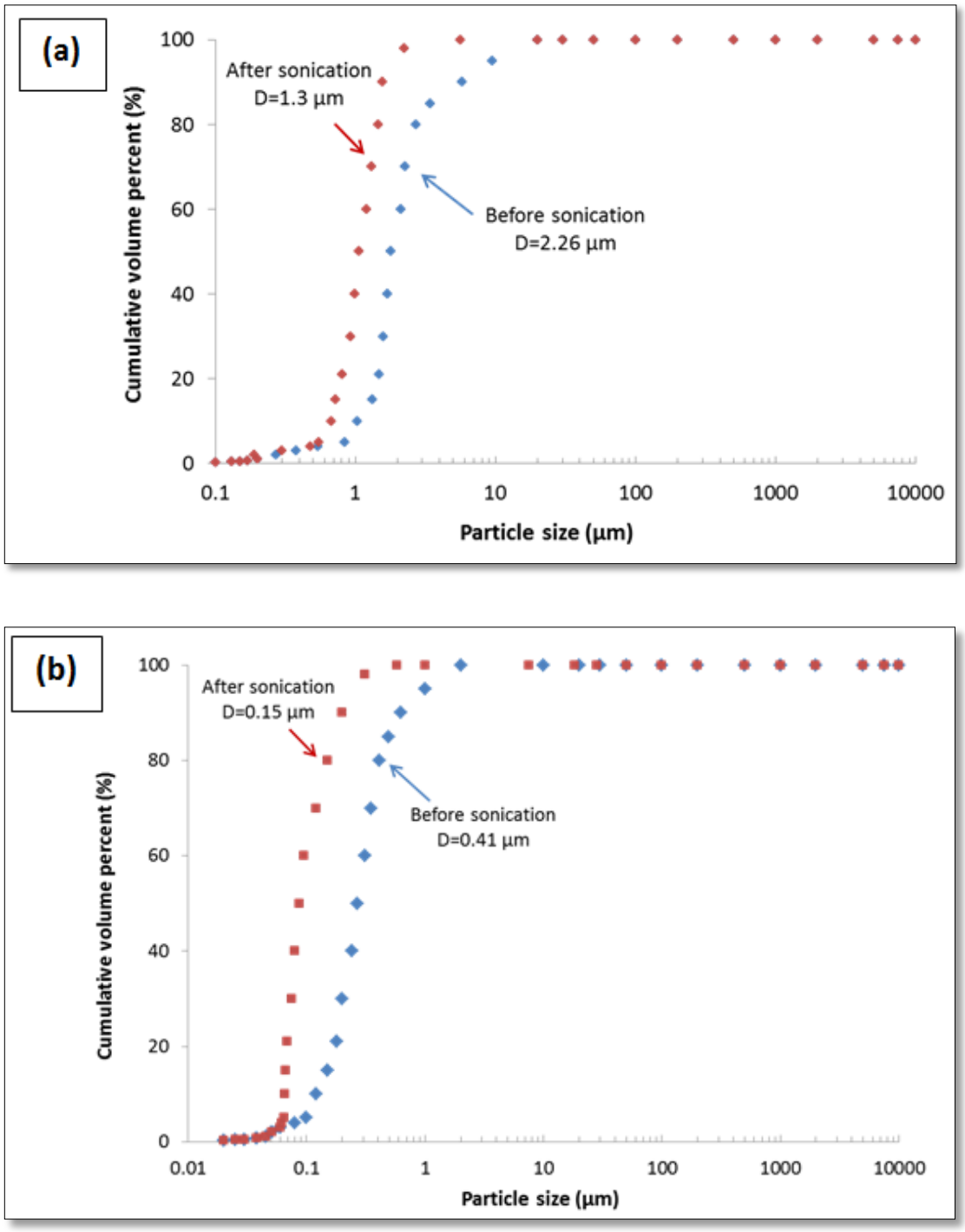

Figure 3.7: Particle size distribution of (a) YSZ and (b) Al_2O_3 powders before and after sonication.

3.3.1.2 Rheological behaviour of ATZ suspensions

To stabilize high solid loading nano-suspensions, it is necessary to achieve the optimum dispersant concentration. A schematic representation on the influence of dispersant concentration on ceramic suspension stability is shown in Figure 3.8. From Figure 3.9, the ceramic suspensions exhibit slight shear thinning behaviour, which is typical for highly concentrated slurries attributed to breakup of agglomerated structure. 0.6 wt. % of Dolapix CE64 appears to be the optimum concentration since lowest viscosities were measured throughout the various shear rates used. Low viscosity is desired as it gives better fluidity of the ceramic suspension, which would facilitate various processes such as sieving, elimination of air bubbles and casting.

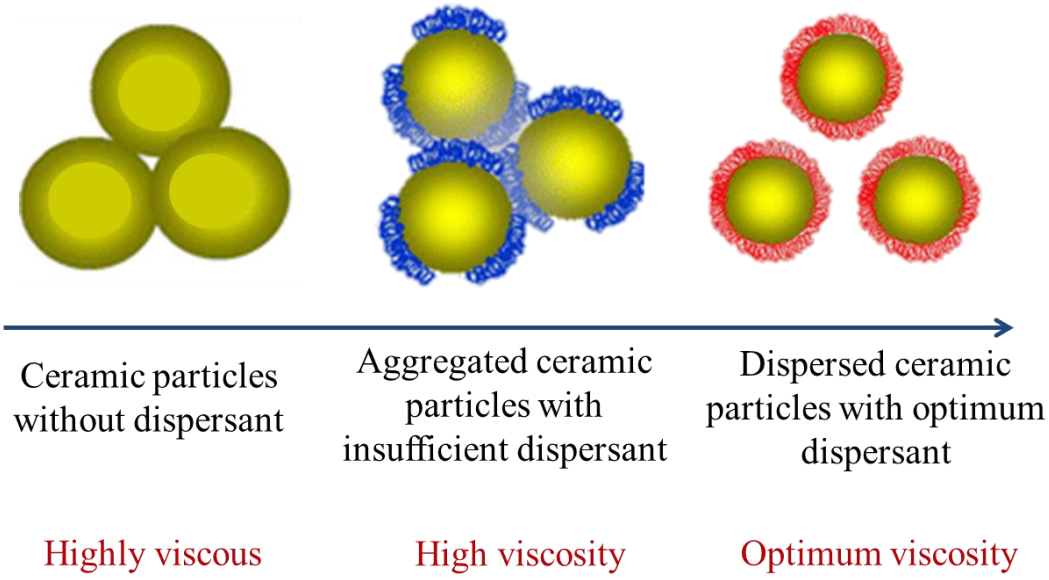

Figure 3.8: Schematic representation on influence of dispersant concentration on the dispersion stability of ceramic suspensions [159].

The dispersing mechanism of Dolapix CE64 is described as adsorption of ionized dispersant on the surface of ceramic particles. This electrosteric mechanism contributes to highly homogenous and stable ceramic suspension. It is observed that

at 0.3 wt. % of Dolapix CE64, the viscosities measured throughout the range of shear rates were higher in comparison to 0.6 wt. % of Dolapix CE64 content. This is due to the reducing amount of dispersant being absorbed on the particle surface. On the other hand, 0.9 wt. % witnessed substantial increase in viscosity for the ceramic suspensions due to micelles formation which promotes bridging flocculation [160]. 0.6 wt. % dispersant is sufficient to cover surface of ceramic particles and repel the particles to keep them apart in the suspension; which leads to increased inter-particle repulsion and stability.

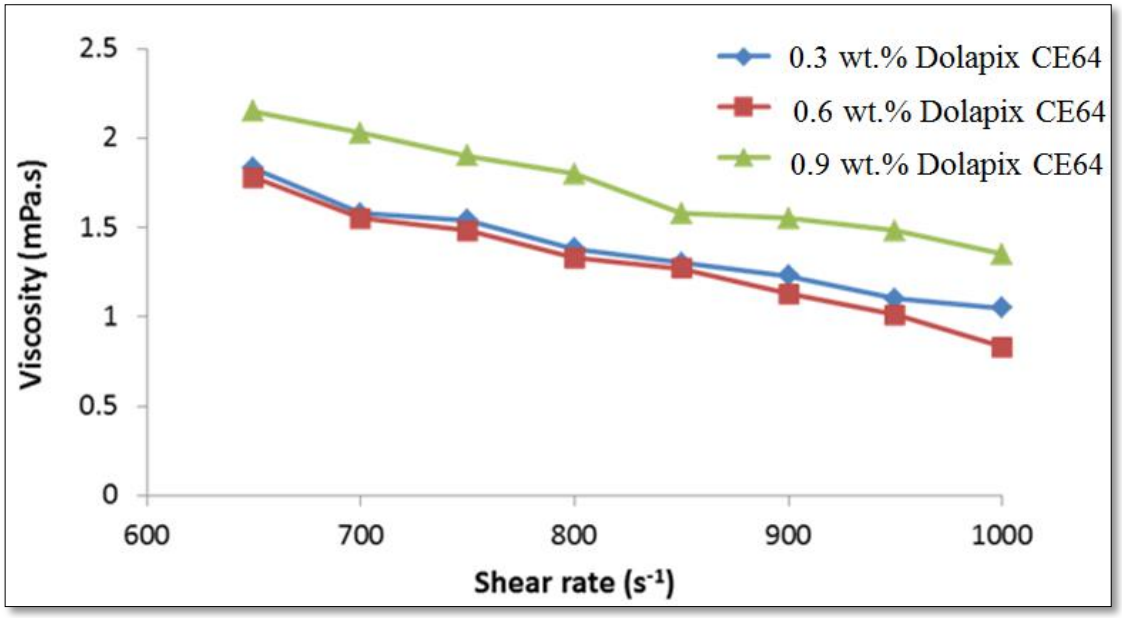

Figure 3.9: Effect of shear rate for ATZ at different concentrations of Dolapix CE64.

3.3.1.3 Colloidal stability

Zeta potential is an indicative measure on the stability of dispersion. Figure 3.10 shows the zeta potential values of YSZ dispersed in distilled water with and without dispersant (Dolapix CE64) at varying pH values from 2 to 12. In the absence of Dolapix, zirconia was positively charged below pH 4.8 and negatively charged above that. The isoelectric point, IEP (pH at which a substance is electrically neutral and molecules have net charge of 0) was about 4.8 which is slightly lower than reported in literature [161–164]. With the addition of dispersant, the zeta potential profile changed significantly and the IEP is now at pH about 2.9. Below the IEP, the surface was less positively charged in comparison to that in the absence of dispersant.

Dolapix CE64 is a carbonic acid dispersant which starts ionizing around pH 3.5 and increases with pH. It completely dissociates above pH 8.5. The zeta potential behaviour of zirconia in the presence of dispersant can be explained as follows. Below pH 2.9, although zirconia surface is still positively charged, the magnitude of the charge is lesser compared to that in absence of dispersant. This indicates that there could be some weak interaction between the un-dissociated Dolapix CE64 and zirconia surface through hydrogen bonding. Hence, some reduction in the magnitude of zeta potential is observed.

Below the IEP of zirconia (pH<2.9), the dispersant starts ionizing and adsorption takes place due to electrostatic attraction between positively charged surface of oxides and negatively charged functional groups of the dispersant. When pH is increased beyond the IEP, the surface will consist of zirconium hydroxyl complexes which can interact chemically with carboxylic group of dispersant. This leads to an overall increase in surface charge. The suspension is more stable under conditions

where charge is maximised. Similar mechanism has been proposed for zirconia-ammonium polymethacrylate system [165]. The adsorption of Dolapix on the surface of zirconia is shown schematically in Figure 3.11.

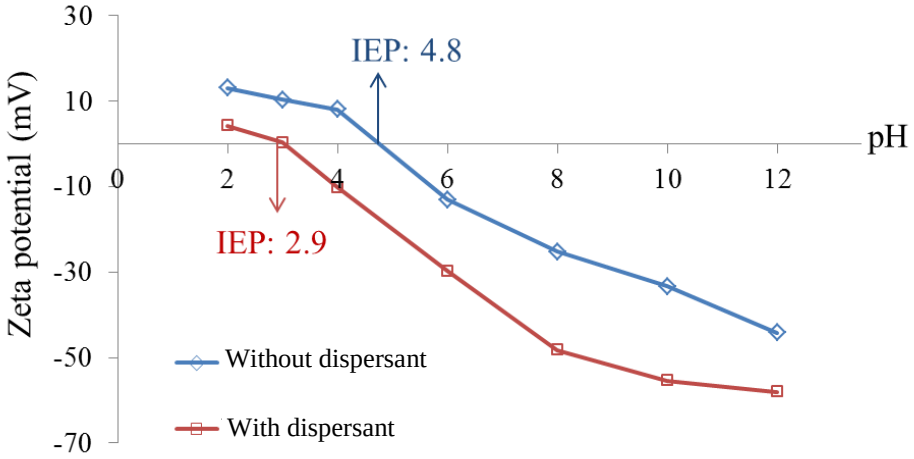

Figure 3.10: Zeta potential of YSZ with and without 0.6 wt. % dispersant.

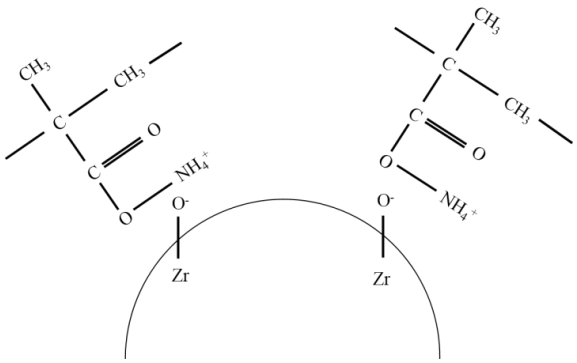

Figure 3.11: Adsorption of Dolapix on the surface of zirconia.

Figure 3.12 shows the zeta potential values of Al_2O_3 dispersed in distilled water with and without dispersant at varying pH values from 2 to 12. Surface chemical properties of alumina ceramic powder were determined by adsorption of H^+ and OH^- ions on the particle surface. In the present study, IEP of alumina was found at pH~9 which is in agreement with reported literature [166]. The surface charge is negative at pH > pH_{iep} and positive at pH< $pH_{iep.}$ Furthermore, IEP shifted to more acidic

region (pH 6.25) upon adding Dolapix CE64. The reason of shift in IEP is two-folded; (i) negatively charged carboxylic group dissociated from the dispersant, adsorbed onto positively charged alumina surface and thus makes the surface more electronegative (ii) when Dolapix CE64 was adsorbed onto surface of alumina particles, hydroxyl group associated with alumina particles reacts with carboxylic group of Dolapix CE64; thus resulting in shift to a lower IEP [166]. Adsorption of Dolapix on the surface of alumina is shown schematically in Figure 3.13.

In both alumina and zirconia suspension, the more negative zeta potential values upon adding Dolapix CE64 indicates the higher colloidal stability (less aggregation and agglomeration) of the suspension.

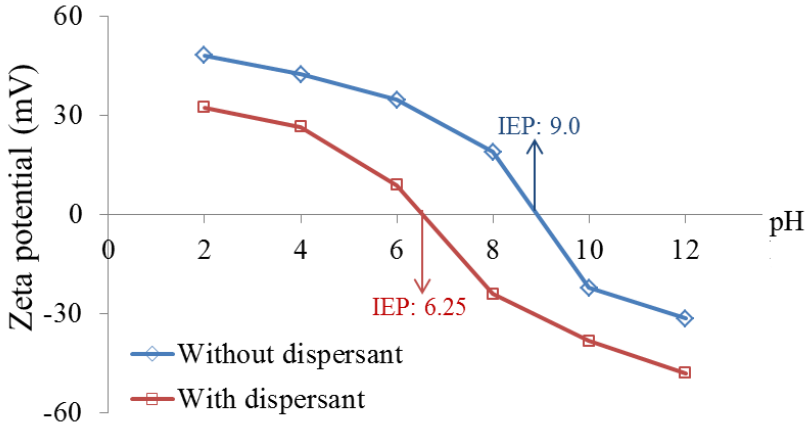

Figure 3.12: Zeta potential of Al_2O_3 with and without 0.6 wt. % dispersant.

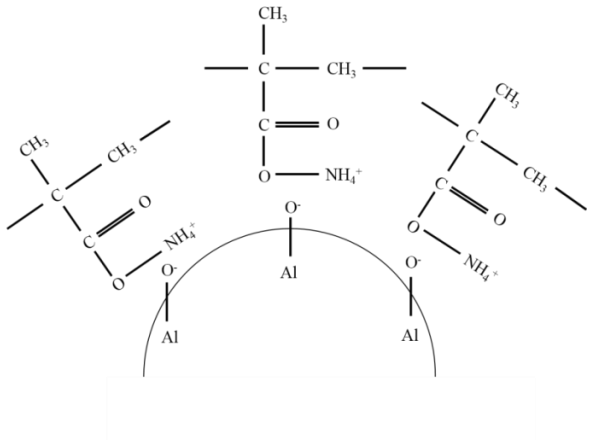

Figure 3.13: Adsorption of Dolapix on the surface of alumina.

3.3.1.4 Calculated specific energy of interaction

Specific energy of interaction is the total energy that is caused by interaction between materials being considered. It can be used to express the real interfacial phenomenon such as how strong bonds are formed at the interface. The specific energy of interaction between alumina and zirconia powder surface with Dolapix CE64 was calculated using Gibbs free energy equation [167];

$$-\Delta G^{O}{}_{SP} = -RT(ln\Delta pH_{iep} - lnC_O - ln1.0396) \qquad \text{[Eq. 3.2]}$$

where ΔpH_{iep} is the shift in IEP at the dispersant concentration C_O and $\Delta G^{O}{}_{SP}$ represents the corresponding specific free energy on interaction. R and T are the standard gas constant and temperature in K respectively. Table 3.4 shows the computed data of interaction energy ($-\Delta G^{O}{}_{SP}$) for Al_2O_3 and YSZ with Dolapix CE64. The high negative value of $-\Delta G^{O}{}_{SP}$ indicates that Dolapix CE64 adsorbs strongly onto surface of YSZ and Al_2O_3 which in turn brings about the shift in IEP. Isoelectric points of Al_2O_3 and YSZ have been brought down to pH 6.25 from 9 and pH 2.9 from 4.8 respectively. Thus, it can be concluded that Dolapix CE64 is effective in altering surface charge of YSZ and Al_2O_3.

Table 3.4: Computed value of specific free energy of interaction for alumina and YSZ with and without dispersant.

System	Concentration (ppm)	pH_{iep}	ΔpH_{iep}	$-\Delta G^{O}{}_{SP}$ (RT units)
Al_2O_3-no dispersant	-	9	-	-
Al_2O_3-Dolapix CE64	5000	6.25	2.85	7.509
YSZ-no dispersant	-	4.8	-	-
YSZ-Dolapix CE64	5000	≈2.9	2.8	7.526

However, it should be noted that amount of dispersant significantly influences stability of suspension due to electrosteric stabilization. Insufficient quantity of dispersant may result in poor distribution of charged particles to overcome the attracting Van der Waals forces. On the other hand, dispersant in excess is unfavourable for stability of ceramic suspensions as it decreases the thickness of electric double layers on ceramic particles that reduces repulsion between particles.

3.3.2 Fabrication, characterization and mechanical properties of Si-O-C cured alumina toughened zirconia (ATZ)

3.3.2.1 Optimum dosage of anti-polymerization inhibitor (PVP)

In this study, ceramic green body were formed through free radical initiated polymerization. In a free radical reaction, presence of oxygen from ambient air decreases reactivity of free radicals which inhibits polymerization. This is shown in Figure 3.14 (20 wt. % Al_2O_3), where surface exfoliation of ATZ composite was observed after exposed to ambient environment. Free radicals were slowly consumed by oxygen from surroundings; thus inhibits polymerization from occurring. To overcome this limitation, anti-polymerization inhibitor (polyvinylpyrolidone, PVP) was added which allows polymerization to occur even in normal laboratory environment. The difference in ceramic surface without and with the addition of PVP is shown in Figure 3.14.

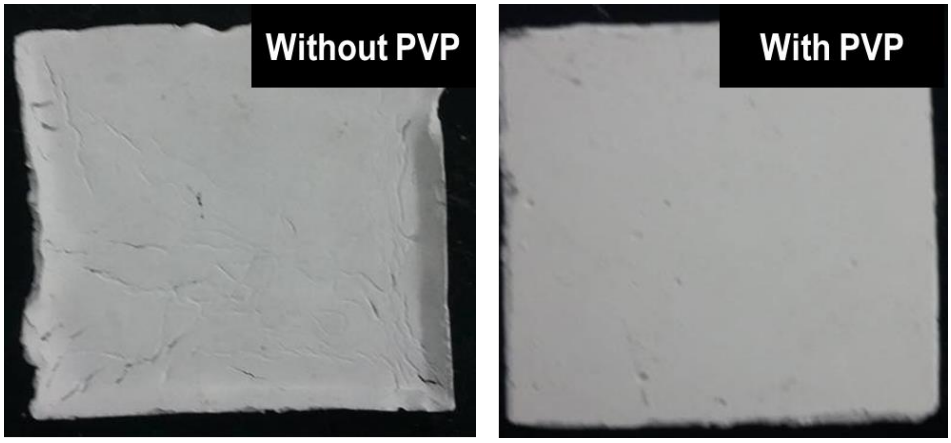

Figure 3.14: Ceramic surface without and with anti-polymerization inhibitor, PVP.

3.3.2.2 Optimum dosage of glycerol solution

Gel casted components are generally brittle which do not favour lamination of ceramic layers. Therefore, typical gel-casting formulation was modified to

accommodate the need of slightly plasticized thick ceramic layer. Plasticizers are added so that ceramic layers can be stretched and deflected during lamination. Two types of plasticizers are usually added. Type I plasticizer is used to soften polymer chains by lowering glass transition temperature, T_g of polymer [168]. Lower Tg allows polymer chain to be stretched without fracturing. Type I plasticizer is known as binder solvent since it can partially dissolve polymer chains to reduce stiffness. On the other hand, type II plasticizer works between polymer chains as lubricant for better mobility [169]. For the PAM gel used in current gel-casting process, water is playing the role of type I plasticizer. Glycerol that was water soluble and compatible with other components was added as type II plasticizer.

Studies were carried out to qualitatively determine the appropriate amount of glycerol. Different premix-to-glycerol ratios were used for the preparation of ceramic layers. Experimental results revealed that premix-to-glycerol ratio of 1:2 are sufficient to provide the required plasticity. Above the ratio of 1:2, the excessive plasticizers will prevent the formation of polymer bonds, which reduces yield strength of green body as depicted in Figure 3.15. In cases where the ceramic layers were under plasticized, the layers are strong however very brittle. Although they can survive during machining, they are susceptible to crack during lamination step.

Figure 3.15: Over-plasticized ceramic layer.

3.3.2.3 Pores elimination using different sintering strategies

Different strategies were implemented to densify the green body composite; (a) single step sintering at temperature of 1200°C for 4 hours; (b) double step sintering by ramping the temperature to 1200°C, reduced immediately to 900°C and held for 30 hours (c) partial sintering at lower temperature of 900°C for 2 hours. After natural cooling to room temperature, the ceramics were removed and immersed into a PDC for an hour followed by thermal curing of the resin at 250°C for an hour. The ceramics were re-heated for 2 hours at 900°C for conversion of the resin into SiOC ceramic.

The effect of different sintering strategies on relative density, grain size, pore size and porosity are shown in Figure 3.16. It indicates the decrease in porosity as relative density increases and inversely proportional relationship between pore size and grain size. Furthermore, porosity variation is due to ceramic grain size upon various sintering mechanisms. The porosity after double step sintering was reduced in comparison to single step or partially sintering. This phenomenon is due to the higher sintering temperature that leads to grain growth. Higher relative density was achieved at higher temperature; partial step sintering at 900°C (rel. density 93 %), single and double step sintering at 1200°C (rel. density 94.1 and 95.4 % respectively). As shown in Eq. 3.4, rate of diffusion depends on the sintering temperature. As such, denser structure is achieved at higher sintering temperature.

$$D = D_O \, exp\left(\frac{-Q}{RT}\right) \qquad \text{[Eq. 3.4]}$$

Where D is the diffusion coefficient, D_o is the constant, Q is the activation energy, R is Boltzmann constant and T is the temperature.

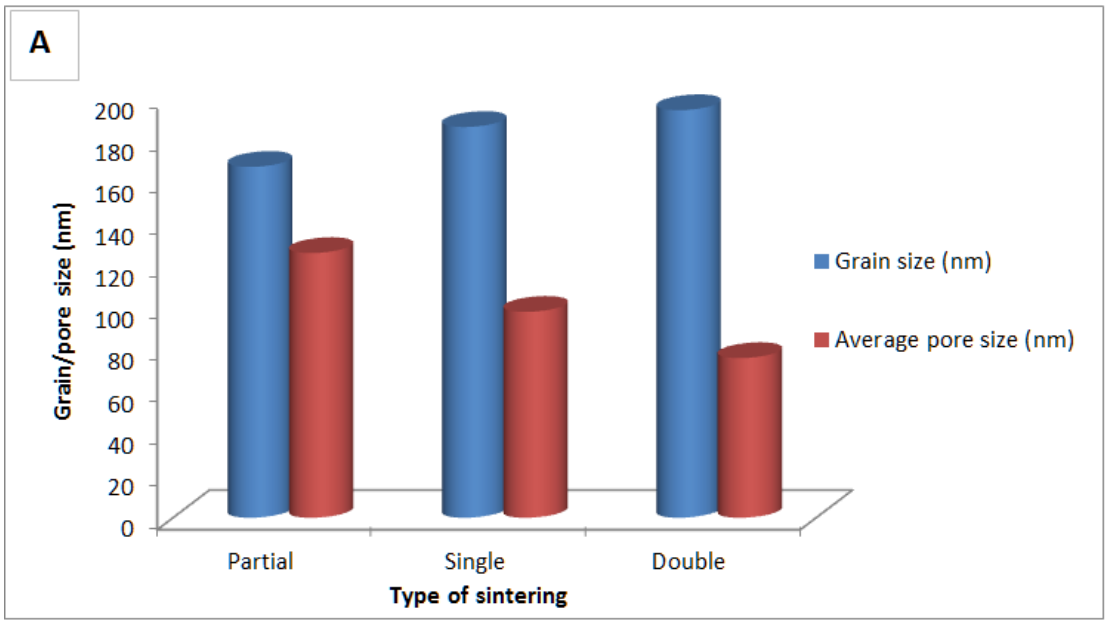

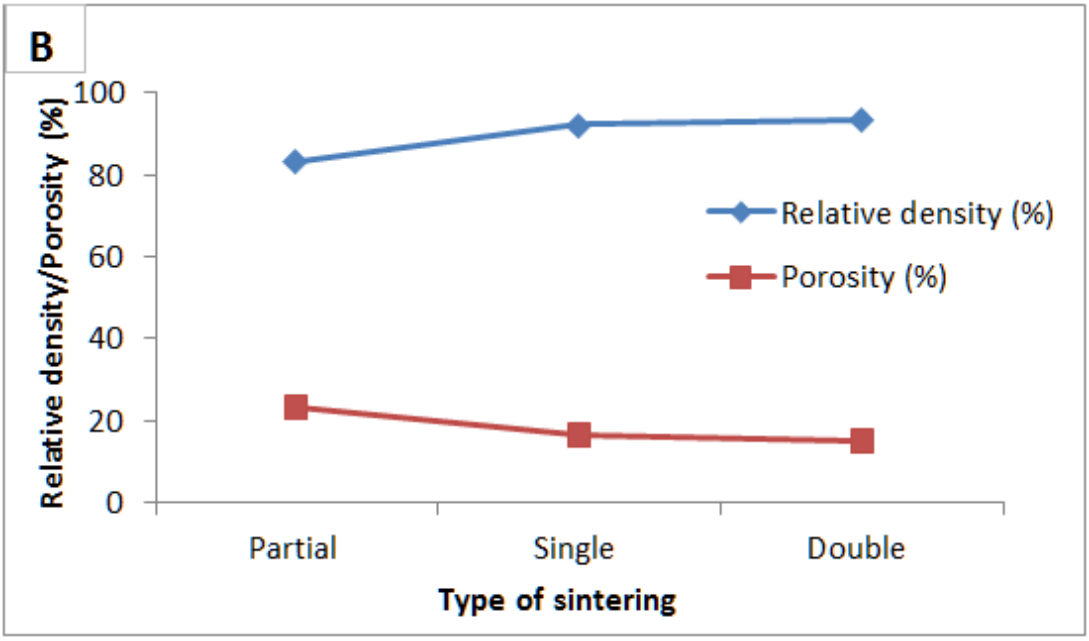

Figure 3.16: Effect of various sintering strategies on (a) relative density and porosity of ceramic (b) grain and pore size.

Besides, it should be noted that sintering time of double step sintering was relatively high (30 hours) than that of single step sintering (4 hours) and partial step sintering (2 hours). The evolution of microstructure with sintering time is as depicted in Figure 3.17. The dependence of the diffusion to time can be explained by Eq. 3.5,

$$r = 2.4\sqrt{Dt} \qquad \text{[Eq. 3.5]}$$

where r is the radical distance, D is the diffusion coefficient and t is the sintering time. It can be seen that atomic displacement is proportional to the square root of time. This is responsible for atomic diffusion which leads to grain coarsening. Thus, the manifestation of Eq. 3.5 can be seen by the changes in morphology and the size of pores and grains.

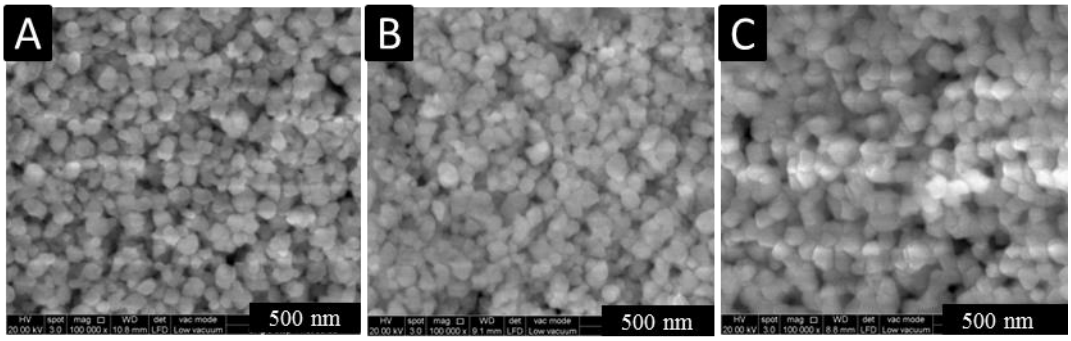

Figure 3.17: SEM images of ATZ composite after (a) partial step sintering (b) single step sintering (c) double step sintering.

Contact angle measurements on ceramic composites were used in an effort to determine the surface energies. Surface energy is important to understand the wetting and adhesion properties of materials. However, determining surface energy is not trivial whereas measuring contact angle is simpler. In this study, contact angles of deionized water droplet on ceramic surface are plotted against time for gradual decrement of angles as the liquid penetrates through surface of the composite (Figure 3.18). It is observed that composite fabricated via double step sintering has higher

contact angle (> 90°) in comparison to those via single step and partial step sintering. This is attributed by the presence of lesser pores (quantity and size) leading to contact angles greater than 90°; designated as hydrophobic surfaces. Figure 3.19 and 3.20 shows the effect of different types of sintering on volume reduction of water droplet on ceramics. It is evident that the volume decreases slowly with double step sintering compared to that of partial step sintering and single step sintering; partially sintered composites has a steeper slope in comparison to single step sintered and double step sintered composites.

$$m_{partial\ step\ sintering} > m_{single\ step\ sintering} > m_{double\ step\ sintering}$$

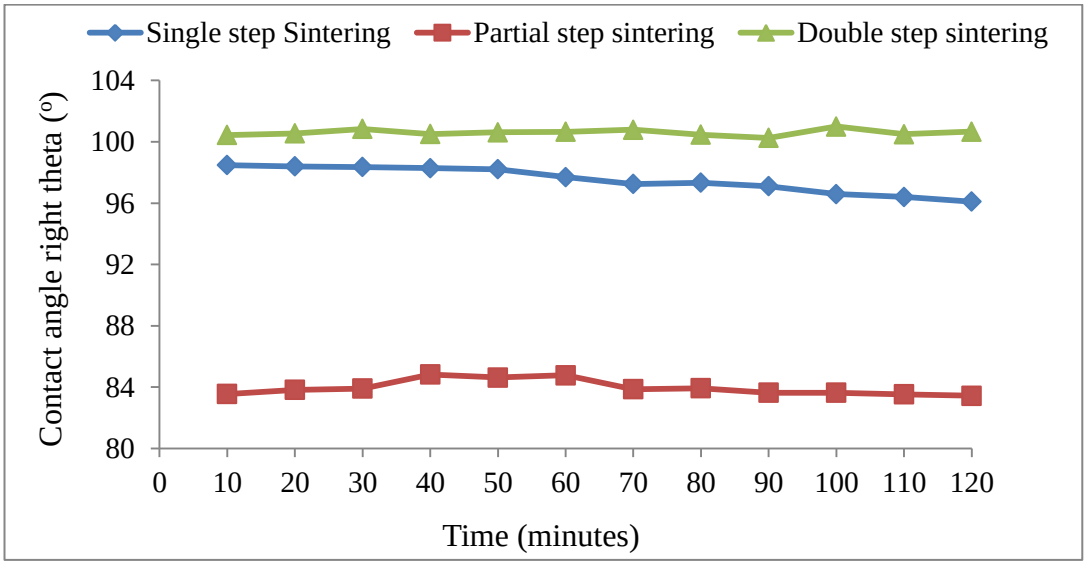

Figure 3.18: Effect of sintering on right theta.

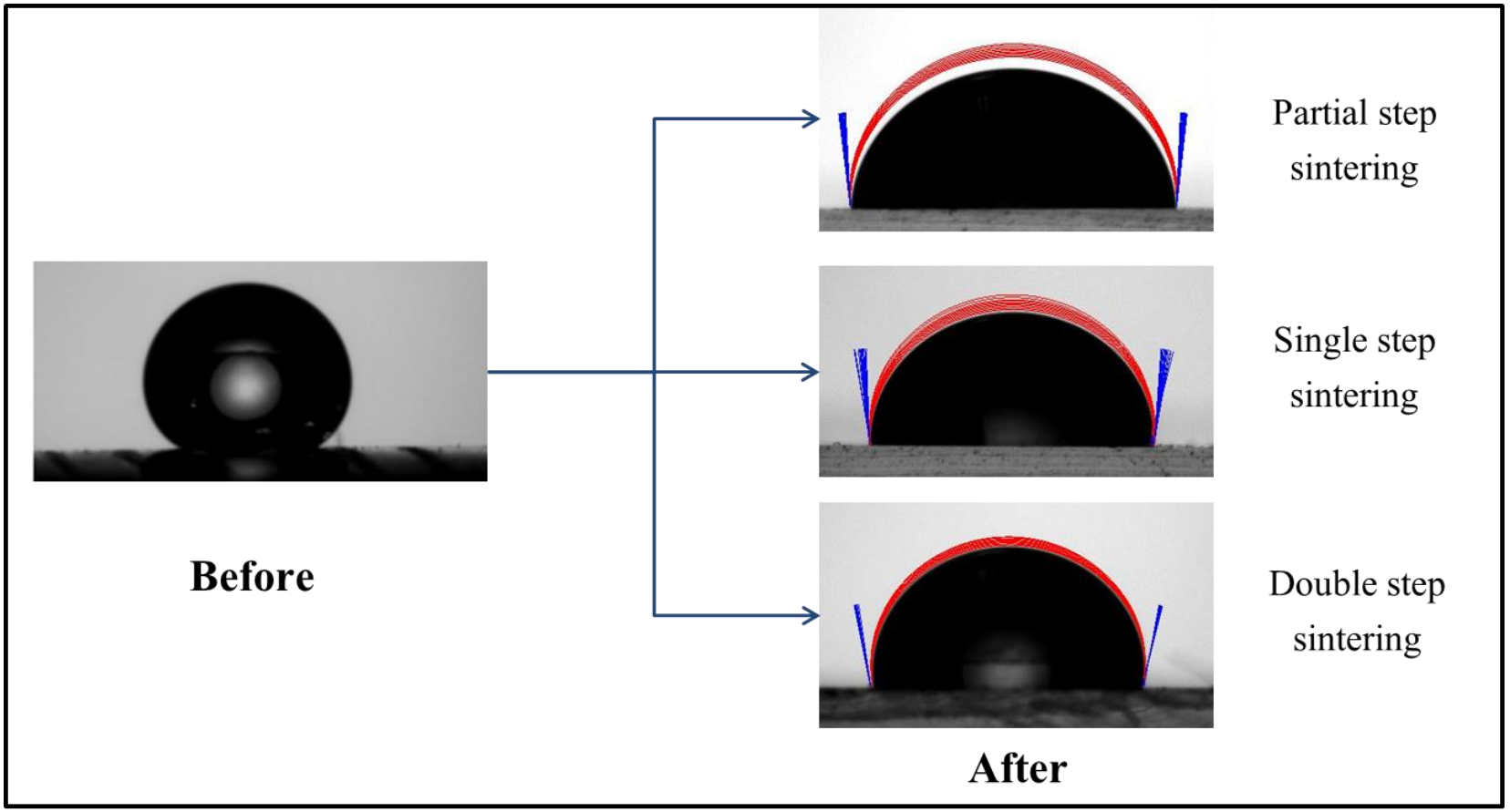

Figure 3.19: Droplet of water on ceramic surface after partial, single and double step sintering.

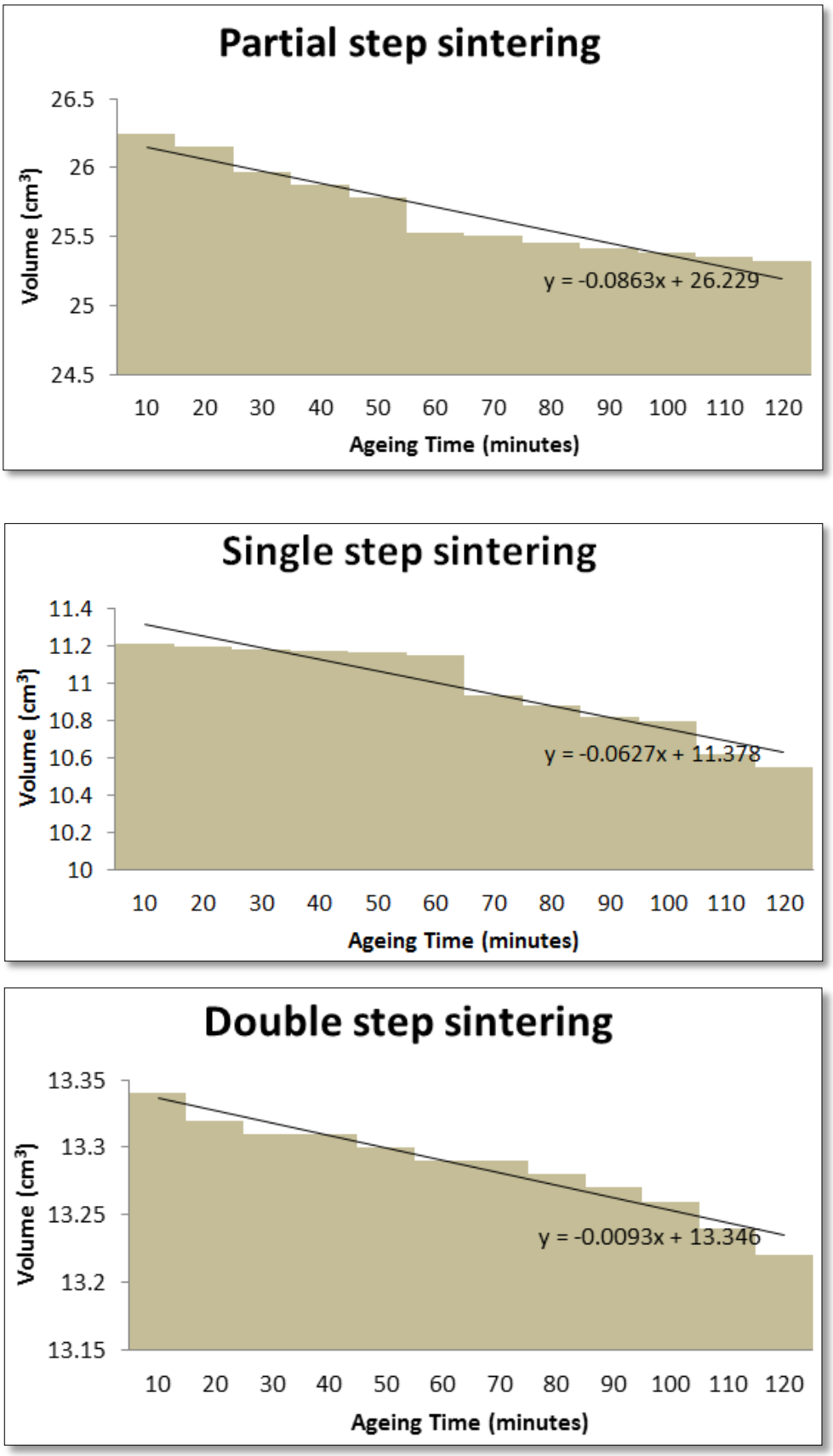

Figure 3.20: Effect of various sintering mechanism on volume reduction on ceramic surface.

3.3.2.4 Microstructure of the as-prepared ATZ sample

SEM micrographs of the composites after sintering are depicted in Figure 3.21. Dark spots represent alumina particles whereas light areas indicate YSZ matrix; similar to observation reported by Choi and Bansal [150]. The Al_2O_3 grains were dispersed uniformly within the major phase of YSZ matrix. Nevertheless, no appreciable micro cracks of adjacent grains or deformation attributed by non-elastic mismatches between YSZ matrix and Al_2O_3 particles were observed in the ceramics. The elemental compositions obtained via EDX analysis shows the element of Si present in the composites. Moreover, the compositions of C and O were significantly high; which is due to infiltration of PDC resin into the composites which consist of Si, O and C. The presence of oxygen is related to polymer synthesis and handling issues; during which materials comes in contact with air.

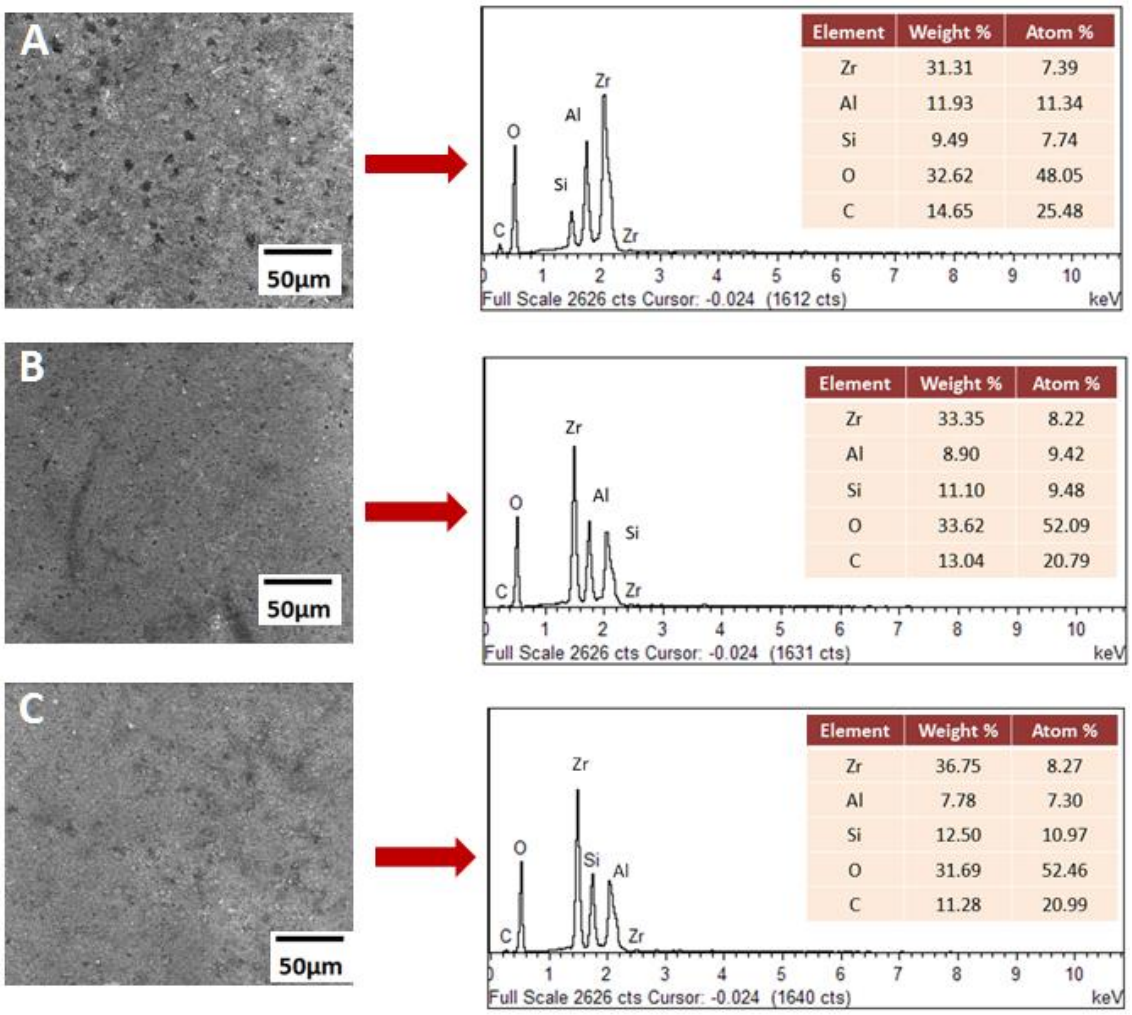

Figure 3.21: High resolution SEM images showing surface of ATZ with (A) 35 wt. % Al_2O_3 (B) 20 wt. % Al_2O_3 (C) 10 wt. % Al_2O_3.

3.3.2.5 Thermogravimetric analysis (TGA)

Figure 3.22 depicts the weight loss of non-sintered monolithic YSZ and Al_2O_3 in ambient air up to 1000°C. Major weight loss was in the range of 150°C to 450°C. The steady weight loss from room temperature to 150°C was due to decomposition of PVP (dispersant) in which the melting temperature ranges from 150°C to 180°C. Two decomposition peaks are observed in the range of 235°C to 310°C; attributed to polycondensation crosslinking reaction in the monomer and cross linker which releases water as demonstrated by Bernardo et al. [170] and removal of glycerol at

290°C. The third peak occurs in range of 410°C to 450°C due to polymer to ceramic conversion [171]. Stagnation of weight loss after 450°C is due to final breakdown of PAM polymer and end of decomposition. The weight loss at 1000°C for YSZ, Al_2O_3 and ATZ composite (20 wt. % Al_2O_3) is 0.61, 0.45 % and 0.53 % respectively indicating exceptional thermal stability of the fabricated composites at elevated temperature.

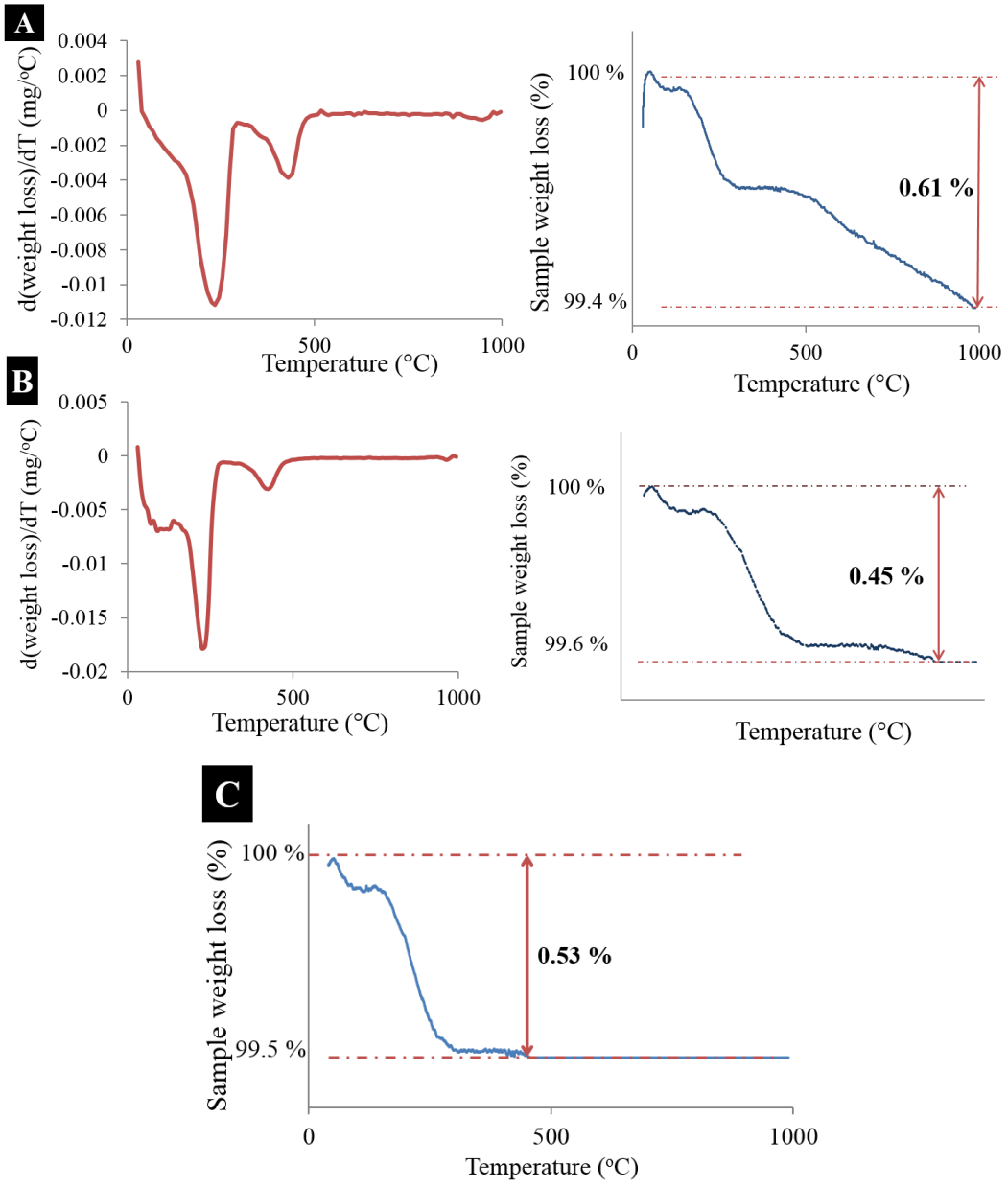

Figure 3.22: TGA analysis on weight loss of non-sintered (A) YSZ and (B) Al_2O_3 and (C) ATZ composite as a function of temperature.

3.3.2.6 FTIR analysis

The ATZ composites sintered at 1200°C were also analysed under attenuated-total-reflectance ATR-FTIR spectroscopy (Figure 3.23). FTIR analysis is most commonly used in the identification and confirmation of produced material. The information is specific in most cases, permitting discrimination of like material. In this study, the bands at ≈500 cm^{-1} are prominent and can be assigned to the stretching frequency of Zr-Y (O) as similar band for YSZ material was reported by Kaus et al. [172]. In general, aluminium atoms are bonded by four or six oxygen atoms. As such, the broad band at ≈761 cm^{-1} is related to stretching vibration mode of tetrahedral AlO_4 whereas the absorption bands recorded in spectral region between ≈575 cm^{-1} and ≈646 cm^{-1} attributed to stretching modes of octahedral AlO_6. The reduced and more differentiated peaks between 3600 cm^{-1} and 3800 cm^{-1} were assigned to the presence of silanol groups [173] , indicating infiltration of the PDC resin into the ceramic. The band at ≈2280 cm^{-1} was assigned to Si-H groups, whereas the band at ≈1629 cm^{-1} was assigned to allyl groups. An overview of spectral features with significant intensity observed in the current study was compared to literature; as depicted in Table 3.5.

Table 3.5: Characteristic IR absorption bands.

Frequency (cm^{-1})	Assignation	Ref.
≈500	Zr-Y (O) stretching	[172,174]
≈575 to 646	Absorption band for alumina	[175]
≈3600 to 3800	Presence of silanol groups	[173]
≈2280	Presence of Si-H groups	[176]
≈1629	Presence of allyl groups	[176]

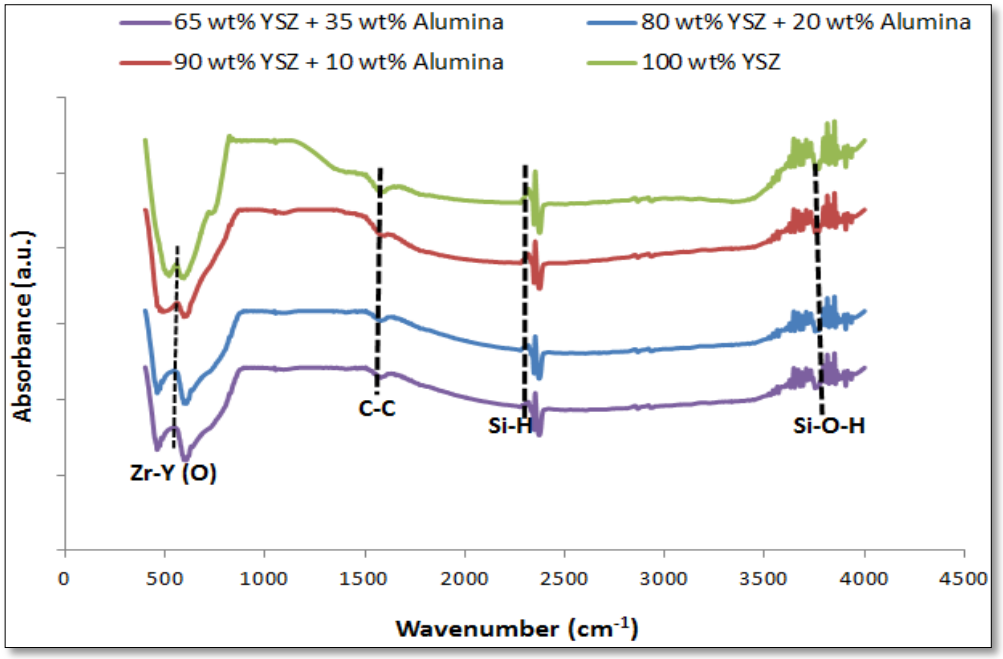

Figure 3.23: FTIR spectra of ATZ produced by gel casting and cured with PDC resin.

3.3.2.7 XRD analysis

Figure 3.24 shows the XRD patterns of the composites. The XRD results indicate that ATZ composites are comprised of Al_2O_3, tetragonal (t)-ZrO_2 and monoclinic (m)-ZrO_2 phases. It is shown that YSZ, as shown in Figure 3.24 (a-d) appears as face centered cubic structure that matches ICSD database number 82-1246 with formula $Zr_{0.8}Y_{0.2}O_{1.9}$. This finding is in agreement with analysis performed by Zalga et al. [177]. Besides, XRD results of the composite matches pattern number 30-1468 which has the formula $Zr_{0.15}Y_{0.85}O_{1.93}$. The ATZ composite consisting of 35 wt. % Al_2O_3 shows wide XRD lines that can be attributed to tetragonal (or cubic) zirconia. It is interesting to note a peak at an angle of 31° for YSZ ceramic which was not discovered in other composites. This peak is associated with presence of monoclinic zirconia. From Figure 3.24, the intensity of monoclinic zirconia phases increased upon addition of alumina. This triggers the transformation of zirconia from

metastable tetragonal phase to stable monoclinic phase. As a result, its contribution to transformation toughening mechanism predominates [178]. Besides, the presence of complete t-ZrO_2 phase can significantly improve the fracture toughness in ATZ composites [179].

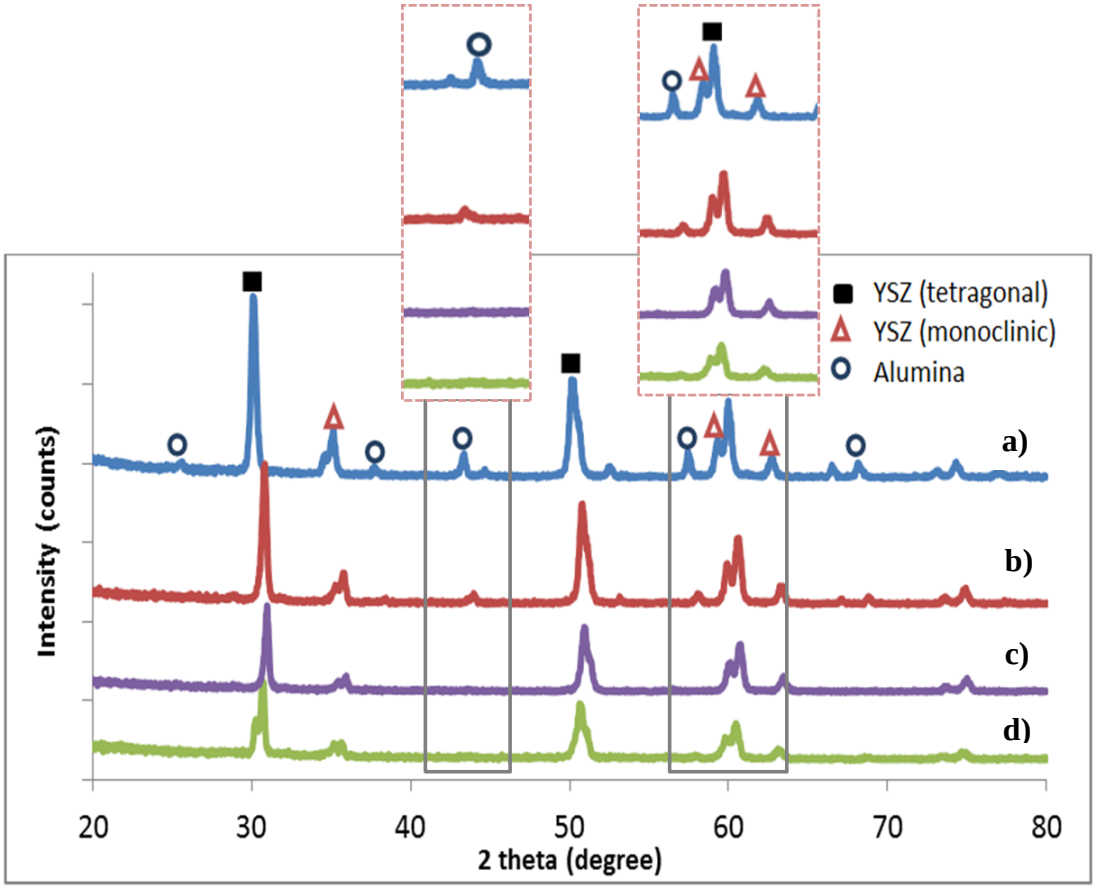

Figure 3.24: XRD patterns of ATZ ceramics cured with PDC resin (a) 35 wt. % Al_2O_3 (b) 20 wt. % Al_2O_3 (c) 10 wt. % Al_2O_3 (d) YSZ.

3.3.2.8 Mechanical, fracture properties and toughening mechanisms

The relative density and mechanical properties of ATZ composites are shown in Figure 3.25 and 3.26 respectively. Mechanical properties of the composites were enhanced upon addition of Al_2O_3. The most significant improvement was observed in ceramics of YSZ reinforced with 20 wt. % Al_2O_3 where hardness and fracture toughness increased by 16.29 % and 25.26 % respectively. Fracture toughness (≈ 5

$MPam^{0.5}$) of ATZ composite is higher than reported fracture toughness which ranged from 1.6 to 3 $MPam^{0.5}$ [150]. These results indicate that the proposed processing route is an improvement from previous work. In the present study, YSZ reinforced 20 wt. % Al_2O_3 exhibited the highest toughness value and relative density.

The fracture toughness of composites in this work were determined by three factors; (i) toughening mechanism (enhanced crack interactions with alumina grain), (ii) mechanical/frictional interlocking of YSZ with Al_2O_3 grains and (iii) properties of YSZ itself (via phase transformation mechanism). In Al_2O_3 reinforced ceramic, high strength of Al_2O_3 is important because once the matrix crack is initiated; load will be transferred from matrix (YSZ) to fillers (Al_2O_3). As such, if the matrix-fillers adhesion is weak, the initiated crack will be deflected along the matrix-filler interface, leaving the fillers intact; thus toughening the composite material. However, if the matrix is too strong, matrix crack penetrates through grains and results in brittle ceramics.

Generally, Vickers hardness of composites are affected by intrinsic deformability of ceramic and microstructural features such as multiphase, porosity, boundary constitution, grain size and orientation [4,180]. In this study, mechanical properties of the ATZ composites do not show proportional improvement with the rising Al_2O_3 content, where further increase above 20 wt. % (i.e. 80 wt. % YSZ) resulted in degradation of composite hardness. It should be noted that hardness of YSZ- Al_2O_3 composites is significantly influenced by its density [2]. The higher values of density indicate good dispersion of Al_2O_3 and lesser presence of pores in the ceramic matrix. As a result, stronger and denser interface bonding occurs between matrix and filler which results in higher mechanical properties of the composite. In the present study, lower hardness value obtained for composite reinforced with 10 wt. % Al_2O_3 may be

due to its lower relative density in comparison to other ceramic composites. Kim and Khalil reported that hardness of Al_2O_3-YSZ ceramics increased from 12 GPa to 17 GPa when density increased from 96 % to 100 % [181]. The decrease in fracture toughness with increasing YSZ content in the ceramic composites is similar to study performed on yttria tetragonal zirconia polycrystals (Y-TZP) ceramics which was correlated to transformability of the composites with increasing yttria content [182]. Simultaneous consideration on hardness and fracture toughness ascertains that optimum composition for ATZ composites produced by gel casting and infiltrated with PDC resin is at 20 wt. % (i.e. 80 wt. % YSZ).

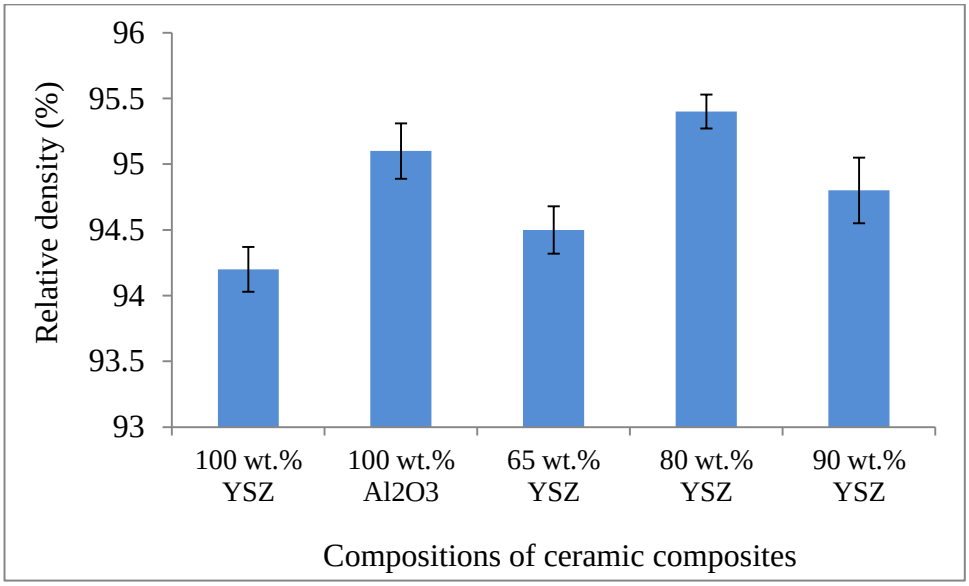

Figure 3.25: The relative density of YSZ, Al_2O_3 and ATZ composites.

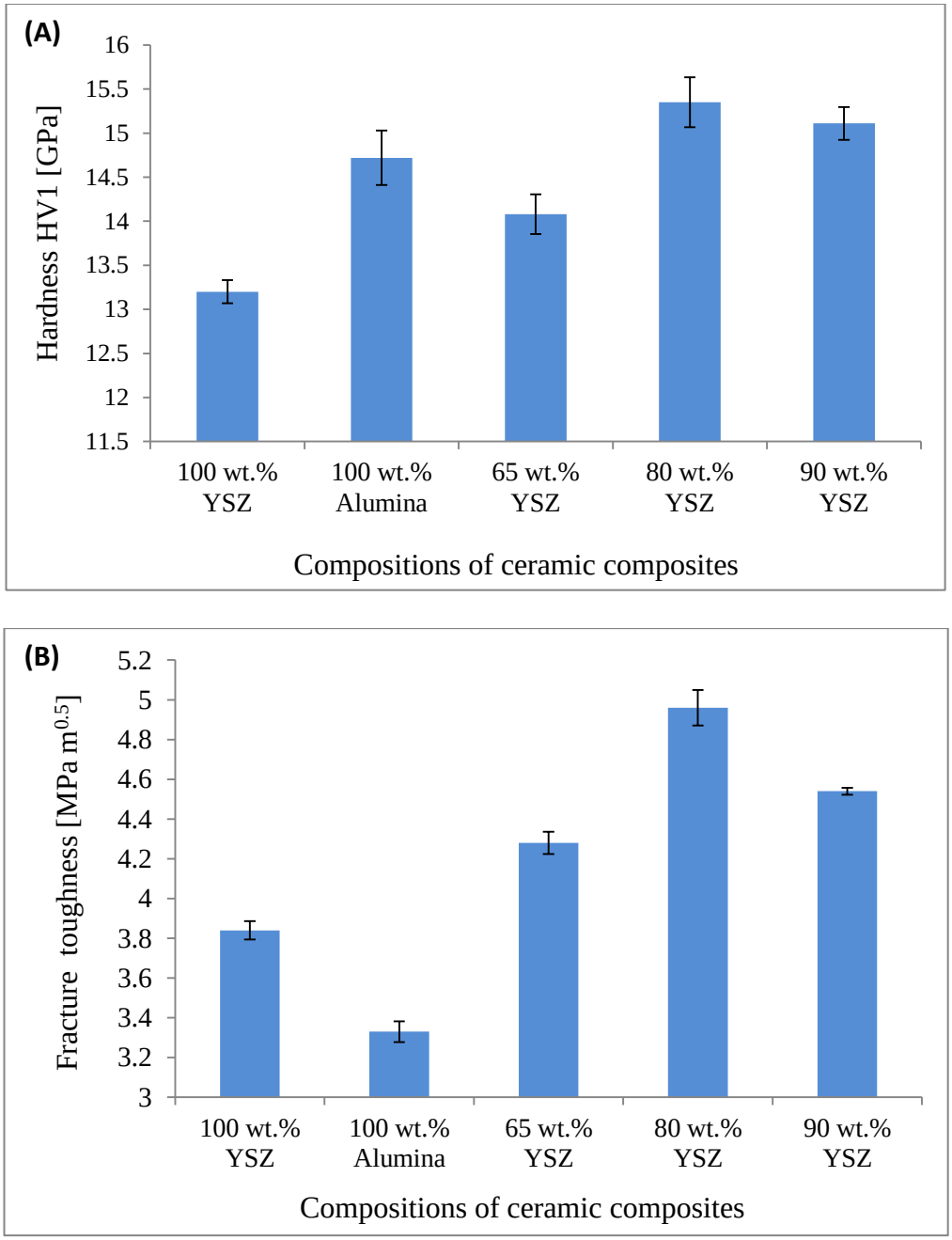

Figure 3.26: The (a) hardness chart and (b) fracture toughness chart of YSZ, Al_2O_3 and ATZ composites.

The toughening mechanisms of ceramics were analysed by fracture patterns generated by Vickers indentation. Toughening mechanisms such as grain bridging and deflection were observed on the fracture surfaces of ceramics reinforced with Al_2O_3. Figure 3.27 depicts the SEM images of the fractured surfaces of monolithic

YSZ and ATZ composites respectively. Swanson et al. reported that grain bridging toughens ceramics as grains become “pinned” behind and advancing crack tip [183]. In the present study, cracks penetrated through the agglomerated grains (Figure 3.27d), in which crack bridging or deflection does not lead to toughening mechanisms. During grain agglomeration toughening mechanism occurs when cracks penetrate through the local residual compressive zone without going around them [157]. As such, stress intensity factor of the crack tip becomes reduced in the agglomerated structures.

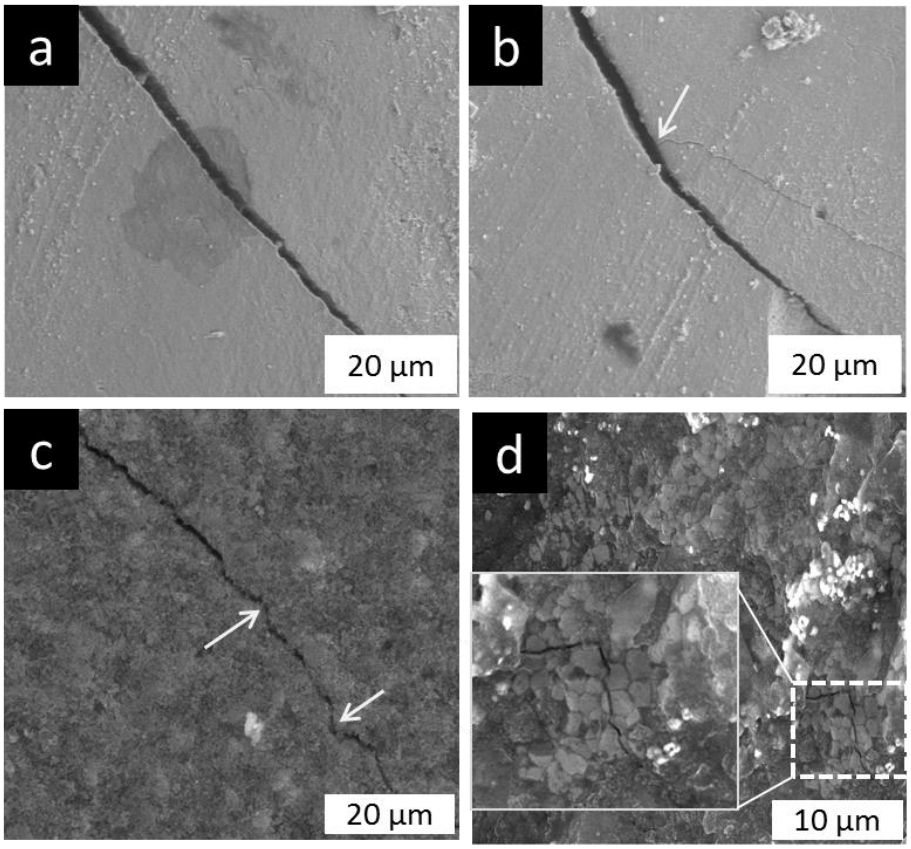

Figure 3.27: High resolution SEM micrographs of reinforcement mechanism of ATZ composites: (a) straight crack path for monolithic YSZ (b) crack bridging for matrix reinforced with 20 wt.% Al_2O_3 (c) crack deflection for matrix reinforced with 10 wt.% Al_2O_3 (d) crack penetration through agglomerated structures for matrix reinforced with 35 wt.% Al_2O_3.

3.4 Conclusions

In conclusion, alumina toughened zirconia (ATZ) were successfully prepared by gel casting method on PDMS soft mold. Well dispersed ATZ composites were obtained by using 0.6 wt. % of Dolapix CE64 as dispersant. SEM analysis has shown uniform distribution of alumina particles in the YSZ matrix. ATZ composite reinforced with 20 wt. % Al_2O_3 showed increase in hardness and toughness by 16.29 % and 25.26 % respectively in comparison to monolithic YSZ. These findings establish Al_2O_3 particles as an effective reinforcing agent to prepare tough ceramics in future, which can be exploited for use in harsh and high temperature environments.

Chapter 4

Characterization and properties of YSZ - graphene ceramic composites

4.1 Introduction

The useful characteristics of yttria stabilised zirconia (YSZ) such as high biocompatibility, low density and good resistance against corrosion have received more commercial attention in hip and join knee replacements [100,184]. However, coarse-grained zirconia particles have considerably low resistance to wear and abrasion owing to their low hardness and fracture toughness when the material is below ductile-brittle transition temperatures. The most promising approach to overcoming this deficient is by adding a second phase into the ceramic matrix [100,101,185]. For example, there is a growing interest to explore graphene nanoplatelets as filler in ceramic matrix due to their exceptional mechanical and electrical properties. The 2-D structure of graphene is expected to provide higher interfacial interactions between filler and ceramic matrix; which are rather difficult to achieve via addition of 0-dimensional nanoparticles [121]. However, homogenous dispersion of graphene platelets in ceramic matrix will be the major challenge.

The technical challenges that need considerable attention are: (i) achieving homogenous dispersion of graphene in the ceramic matrix owing to different surface chemistry and insoluble characteristics of ceramics (ii) porosity induced in ceramic-graphene composites (iii) deterioration of mechanical properties above optimum filler content or processing parameters. Therefore, the major aim of this chapter was

to investigate the influence of graphene loading in YSZ matrix to achieve the best mechanical properties. Optimum graphene loading was used to study the effect of processing parameters (stirring speed and duration) to achieve uniform distribution of graphene in the matrix. Main attention was addressed to measure the hardness and fracture toughness using Vickers Indentation method. The crack propagation of YSZ and YSZ-Gr composites were compared and reinforcement mechanism of graphene platelets within YSZ matrix was studied by scanning electron microscopy. Effect of graphene loading on electrical properties of YSZ-Gr composite was also studied.

4.2 Experimental Procedure

4.2.1 Materials and reagents

The details of ceramic powder (YSZ) and other materials used for gel casting have been described in Section 3.2.1. CTAB (EMD Chemicals) was used as surfactant to disperse graphene. Graphene platelets of 6-8 nm in thickness and 15-25 µm in level dimensions were used as nano-fillers and were purchased from Graphene Industries Ltd, U.K.

4.2.2 Graphene preparation

Graphene platelets were dispersed in 300 ppm CTAB solution and sonicated (Elma Sonic 30H, Singen/Htw Germany) at 60°C for 1.5 hours, followed by vacuum filtration. The filtered graphene was washed with large amount of distilled water to remove excess CTAB. Graphene flakes were filtered from graphene suspension using 125 mm filter discs.

4.2.3 Gel casting of ceramic layers

The YSZ-Gr composite was prepared according to the procedure illustrated in Figure 4.1. In section 4.3.1, graphene loading in YSZ matrix was varied from 0.2, 0.3, 0.5,

1.0 and 2.0 wt. %. The suspension was stirred at 300 rpm for 14 hours. The suspension was stirred at varied durations (10, 14, 18 and 22 hours) and speeds (300, 400, 500, 600 and 700 rpm) to achieve deagglomerated and stable suspensions. All the suspensions were then kept in a vacuum desiccator to remove entrapped gas bubbles. Polymerization was initiated by APS and catalyst which was added at 2 µl/g and 1 µl/g respectively. Polymerization was accelerated by further heating in the oven at 50°C for 2 hours.

4.2.4 Sintering and sealing of pores

YSZ-Gr composites were sintered using tubular furnace (CWF1200, Carbolite, UK) at temperature elevation of 15°C/min to 320°C for 2 hours, followed by further heating at 1200°C and held for 30 hours in presence of argon gas to achieve densification of ceramic. After natural cooling to room temperature, the ceramic composites were removed and immersed into a polymer derived ceramic (PDC) resin (RD-212a, Starfire Systems Inc.) for an hour followed by thermal curing of the resin at 250°C for an hour. The ceramic composite was re-heated for 2 hours at 900°C for conversion of PDC resin into SiOC based ceramic.

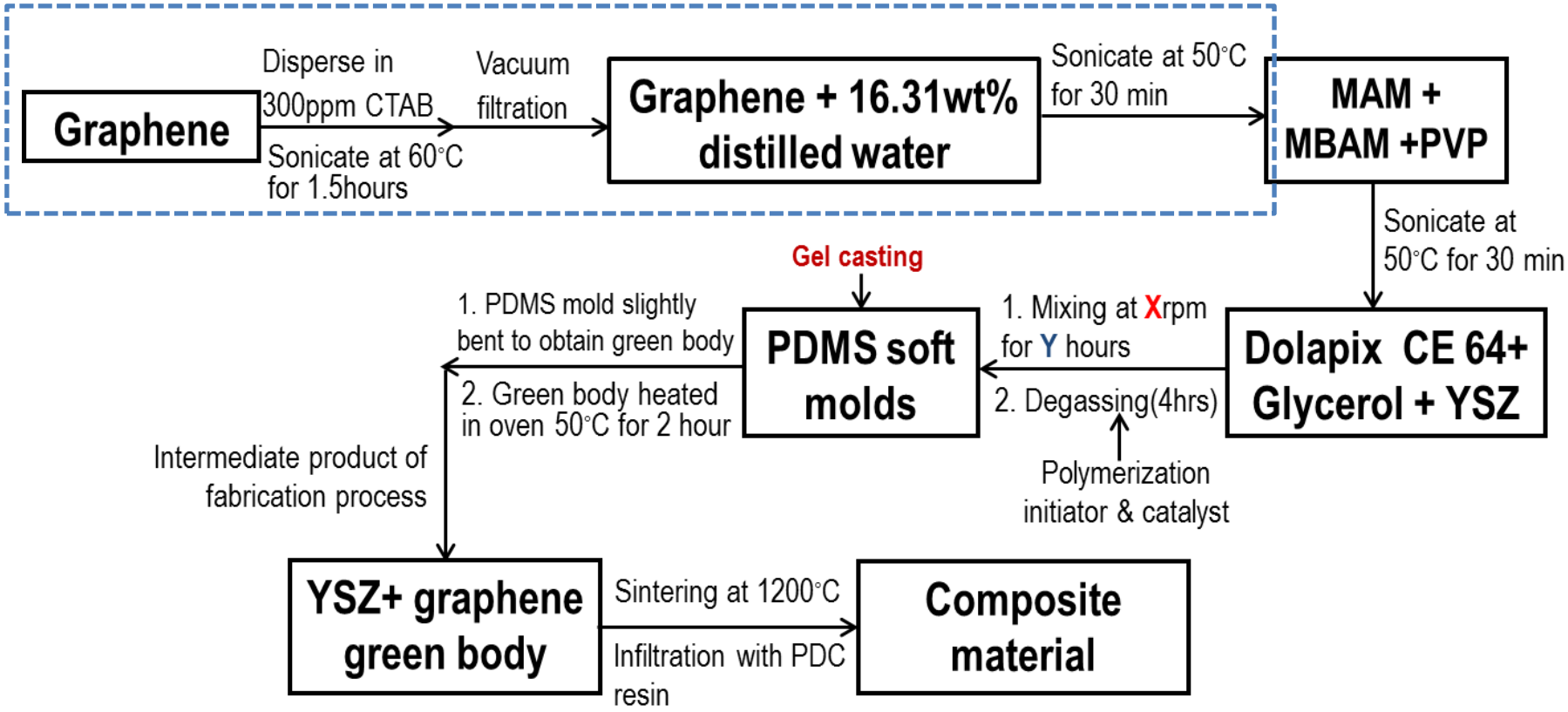

Figure 4.1: Expansion of Figure 3.3 to prepare YSZ-Gr composites where; X and Y represent the variation in stirring speed and time respectively.

4.2.5 Characterization

Hardness, fracture toughness and microstructural analysis procedures are similar to Section 3.2.3. Density of the sintered composites was measured using Archimedes method by a pycnometer (Lenz Laborglas, Germany). Porosity of the ceramics was determined using the equation 4.1;

$$Porosity = \left[1 - \left(\frac{\rho_{bulk}}{\rho_{theoretical}}\right)\right] x\ 100\ \% \qquad \text{[Eq. 4.1]}$$

where ρ_{bulk} is the bulk density of the ceramic composite (g/cm^3) and $\rho_{theoretical}$ is the theoretical density of the ceramic composites (g/cm^3). Bulk density was determined using Archimedes principle while theoretical density was calculated using the rule of mixture (with values of 2.1 g/cm^3 and 5.68 g/cm^3 for graphene and YSZ respectively) using equation 4.2;

$$\frac{1}{\rho_c} = \frac{W_f}{\rho_f} + \frac{W_m}{\rho_m} \qquad \text{[Eq. 4.2]}$$

where ρ_c is the density of ceramic composite, ρ_f is the density graphene and ρ_m is the density of YSZ. On the other hand, electrical resistance was measured using multimeter and the conductivity was calculated using equation 4.3;

$$R = \frac{1}{\sigma}\frac{l}{A} \qquad \text{[Eq. 4.3]}$$

Where σ is the conductivity of the material, l is the length and A is the cross sectional area of the material. A minimum of six measurements were averaged for each sample. Dynamic mechanical analysis was conducted using Perkin Elmer DMA 8000 instrument. The specimens were prepared in a dimension of 25x 6x 3 mm using PDMS soft molds and tests were performed with the dynamic load frequency set at 25, 50, 75 and 100 Hz.

4.3 Results and Discussion

4.3.1 Effect of graphene loading on mechanical and electrical properties of YSZ ceramic

4.3.1.1 XRD analysis

XRD patterns of the sintered YSZ-Gr composites depicts that all diffraction patterns matched with ZrO_2 (JCPDS #42-1164); where the phenomena of tetragonal to monoclinic phase transformation were not observed during consolidation (Figure 4.2). Typical peaks of ZrO_2 are without detectable carbide phases, indicating absence of significant reaction between YSZ and graphene during sintering. Furthermore, a new peak was observed at $2\theta \approx 27°$ for graphene content of 2 wt. % due to the significance of crystalline graphite; whilst an almost negligible graphitic peak was observed for composite containing 0.2 wt. % graphene. The graphitic peaks were observed through XRD analysis due to the platelet structure of graphene which enables (002) planes dominant and detectable by XRD analysis.

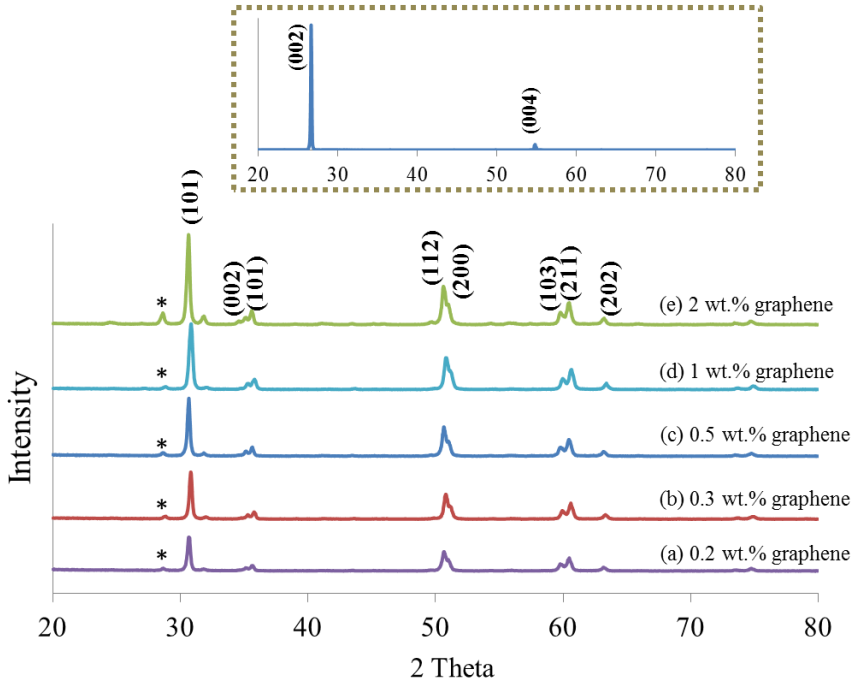

Figure 4.2: XRD patterns of YSZ- graphene nanocomposites and an insight showing XRD of as obtained graphene platelets.

4.3.1.2 EDX/Microstructural analysis

EDX analysis was carried out to determine its elemental composition and verify presence of Si elements from the infiltration of PDC resin into ceramics. Figure 4.3 depicts the spectrum from EDX analysis on the ceramic surface of YSZ reinforced with 1 wt. % graphene. As expected, the element of Si was detected in the analysis. Moreover, composition of C was significantly high due to infiltration of PDC resin into ceramic composite that consist of Si, O and C.

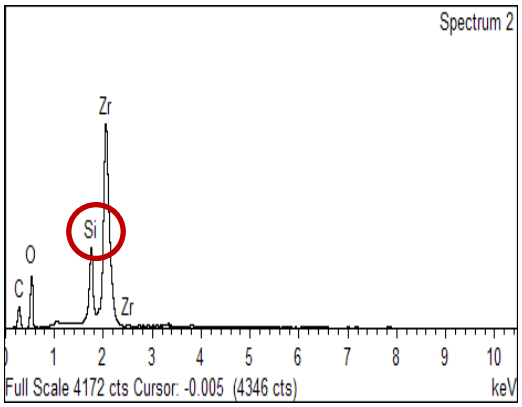

Figure 4.3: EDX spectrum of YSZ reinforced with 1 wt. % graphene and infiltrated with PDC resin (RD-212a).

A challenge associated with the preparation of YSZ-Gr composite is to develop processing route that ensures homogenous distribution of graphene platelets within the host matrix and embedment of thin graphene sheets within the ceramic matrix due to the unique properties of graphene associated with single or few layer sheets [186]. The objectives were achieved as shown in SEM analysis in Figure 4.4, in which graphene platelets were well distributed within the ceramic matrix and their overall thickness were generally below 50 nm (marked by white arrows). The thinnest graphene sheet is 21.87 nm and approximately 0.5 µm in length in the 1 wt. % YSZ-Gr composites. These results proves the proposed processing route is an improvement from previous work reported, in which most pulled out sheets were exceeding 50 nm in thickness [132].

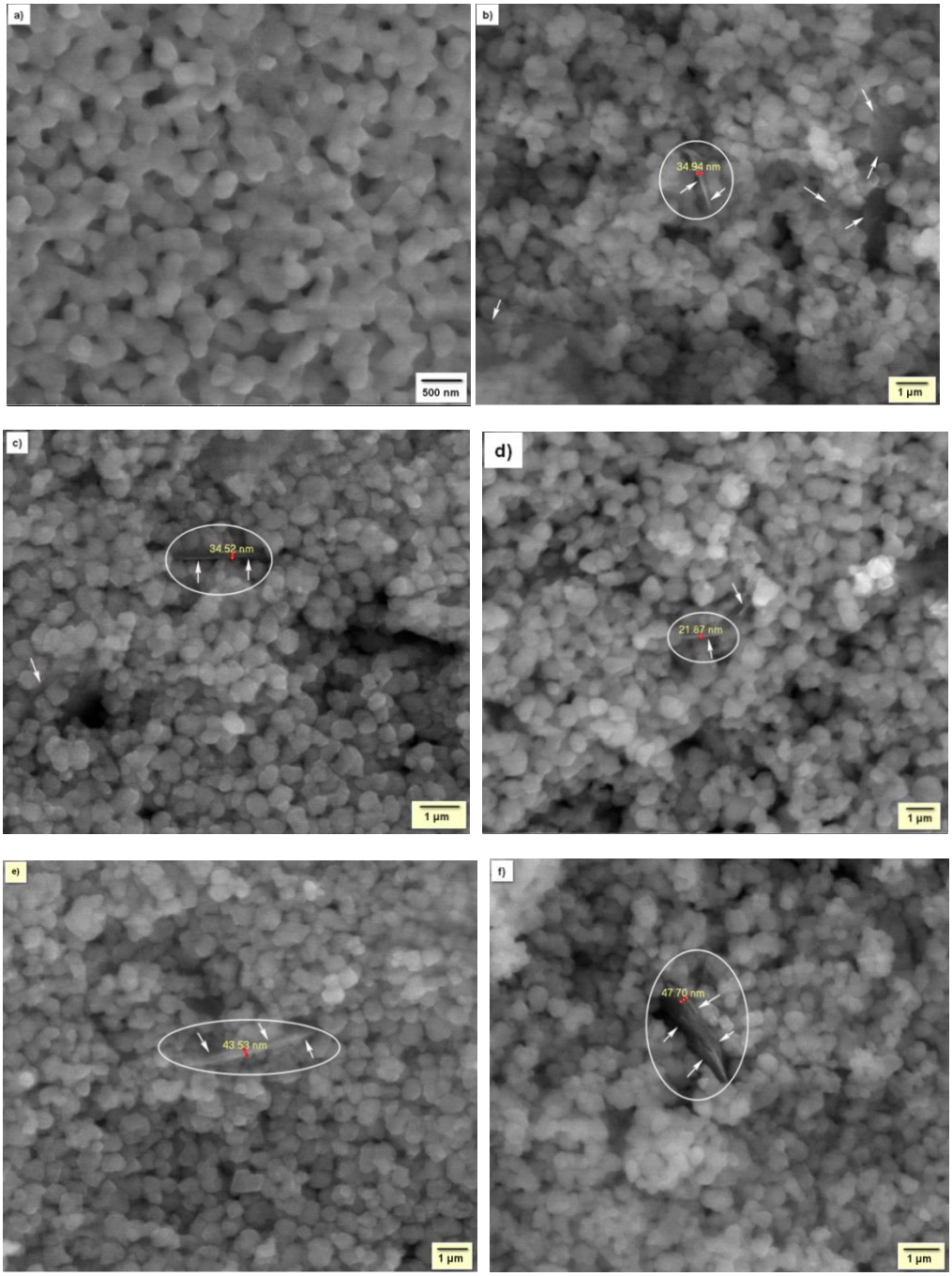

Figure 4.4: High resolution SEM images showing surface microstructure of YSZ reinforced with different wt.% graphene (a) monolithic YSZ (b) YSZ + 0.2 wt.% graphene (c) YSZ + 0.3 wt.% graphene (d) YSZ + 0.5 wt.% graphene (e) YSZ + 1 wt.% graphene (f) YSZ + 2 wt.% graphene. White arrows indicate graphene platelets were embedded within ceramic host matrix.

4.3.1.3 Mechanical, fracture properties and toughening mechanism

Mechanical properties of YSZ reinforced with graphene platelets is compiled in Table 4.1, in which mechanical properties of the composites have been enhanced upon addition of graphene platelets. The most significant improvement in mechanical properties was observed in composites of YSZ reinforced with 1 wt. % graphene platelets; where fracture toughness and hardness of composites increased by 20.31 % and 25.78 % over monolithic YSZ with maximum values of 4.62 $MPa^{1/2}$ and 16.6 GPa respectively (Figure 4.5). The increment in fracture toughness was higher in comparison to the study performed by Chintapalli et al. where YSZ reinforced with 2 vol. % carbon nanotubes (CNT) reported approximately 15 % higher fracture toughness in comparison to the monolithic ceramic [187].

Table 4.1: Mechanical properties of the YSZ-Gr composites and monolithic YSZ.

Material	Grain size (nm)	Hardness HV1 (GPa)	Fracture toughness K_{IC} (MPa $m^{0.5}$)
YSZ	145±17	13.20±0.52	3.84±0.21
YSZ + 0.2 wt.% graphene	146± 12	14.38±0.45	4.16±0.29
YSZ + 0.3 wt.% graphene	190±19	15.20±0.54	4.39±0.26
YSZ + 0.5 wt.% graphene	173±16	16.10+0.52	4.42±0.23
YSZ + 1 wt.% graphene	186±21	16.60±0.47	4.62±0.28
YSZ + 2 wt.% graphene	166±23	14.90±0.53	4.49±0.25

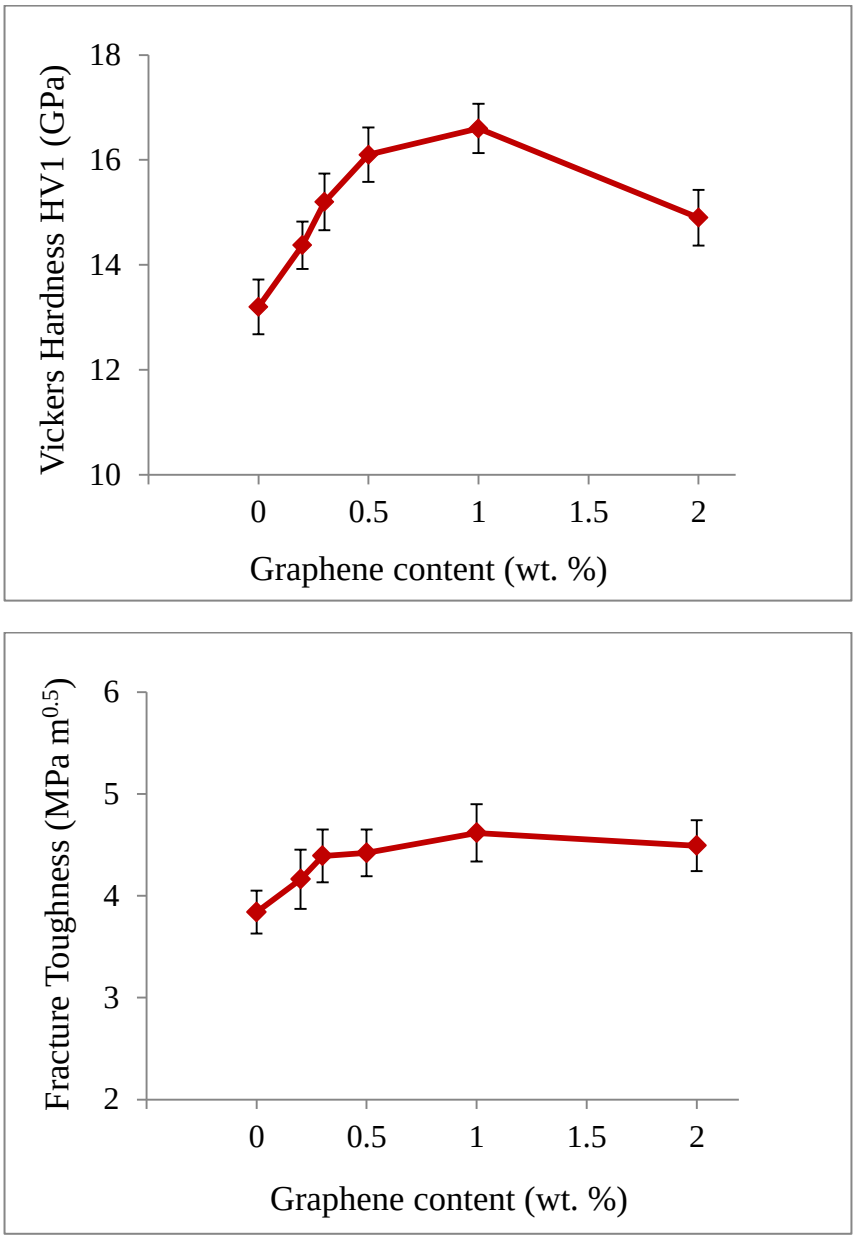

Figure 4.5: Mechanical properties of YSZ-Gr composite.

This work revealed the ability of graphene to effectively toughen YSZ with small amount of graphene as filler. Through the proposed processing route, mechanical properties were improved in comparison to other studies (132). The fracture toughness of YSZ-Gr composite in this work was determined by three factors; toughening mechanisms (crack bridging, crack deflection, crack branching and graphene pull-out), mechanical/frictional interlocking between YSZ-Gr and the

excellent properties of graphene as reported in Section 2.2.1 of this thesis. The differences in toughness between monolithic ceramic and graphene reinforced composites can be explained as follows; in nanofiller reinforced ceramic, high strength of reinforcing fillers is important because once the matrix crack is initiated, load will be transferred from the matrix to fillers during initiation of crack. As such, if the matrix-fillers adhesion is weak, the initiated crack will be deflected along the matrix-filler interface leaving the fillers intact thereby toughening the composite. However, if the matrix is too strong irreversible crack penetration through ceramic grains results in the brittle composites as exemplified by monolithic ceramics.

The mechanical properties of YSZ-Gr composites do not show proportional improvement with the rising graphene content, where further increase above 1 wt. % resulted in degradation of both fracture toughness and hardness. Figure 4.6 shows YSZ matrix reinforced with 2 wt. % graphene platelets where overlapping of graphene platelets was observed. Similar finding was reported by Liu et al. [119]. The overlapped platelets were considerably thick ranging from 60-120 nm. This indicates the agglomeration of graphene where increase in amount of pores is likely to be formed between agglomerated graphene platelets and ceramic matrix interface. The presence of these pores inevitably reduces contact area of ceramic matrix with graphene platelets and initiates cracks in which stresses are released in an inefficient way. For example, if a crack propagates and meets the graphene platelets, it will be arrested and deflected in plane. Such crack deflection mechanism will create a complex pathway to release stress which helps to increase toughness of ceramic composite. Besides, pores also reduce the interfacial friction during graphene pull-out from the ceramic matrix. As such agglomeration of graphene platelets leads to degradation of strengthening and toughening of graphene in their host matrix. In the

present study, simultaneous consideration on hardness, fracture toughness and porosity effects upon graphene reinforcement reveals that optimum level of graphene addition for YSZ ceramics produced via gel casting route is at 1 wt. %.

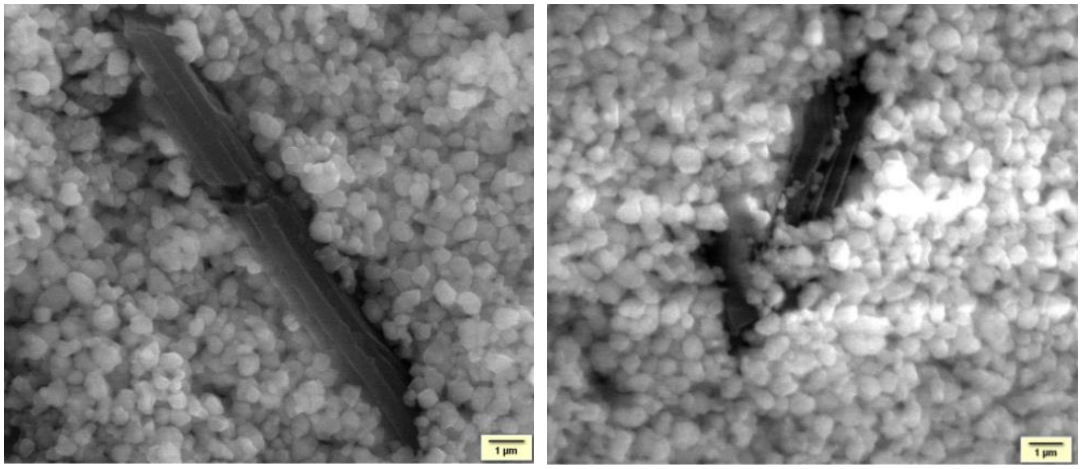

Figure 4.6: SEM images of YSZ composites reinforced with 2 wt. % graphene.

The toughening mechanisms of the composites were studied by analysing the fracture patterns generated by Vickers indentation. Similar to many reported literatures on graphene reinforced ceramics, toughening mechanisms such as crack bridging, crack deflection, crack branching and graphene pull-outs were observed on the fracture surfaces of the ceramic composite reinforced with graphene platelets. Table 4.2 depicts the SEM images on fracture surfaces of YSZ reinforced with different loadings of graphene.

The toughening by crack bridging, crack deflection and crack branching in this study were majorly observed at low graphene loadings (0.2 and 0.3 wt. %). Toughening by graphene pull-out mechanism is more significant at high graphene loading (1 and 2 wt. %). These graphene pull-outs were different in dimensions, orientation to plane of fracture surface and different pulled out lengths. From the images, graphene platelets were either tucked or semi-wrapped around the host matrix grains. The

orientation of graphene fillers within the matrix resulted in greater energy requirement to pull-out the platelets. This is attributed by the graphene "platelet wrapping" around grain boundaries which enhances its contact area with the host matrix. Such finding is in agreement with work reported by Walker et al. and Dusza et al. [77,114].

Table 4.2: Characteristic toughening mechanism on the fracture surface of YSZ-Gr composites reinforced with different wt. % graphene.

wt.% graphene	Toughening mechanisms
0.2 and 0.3	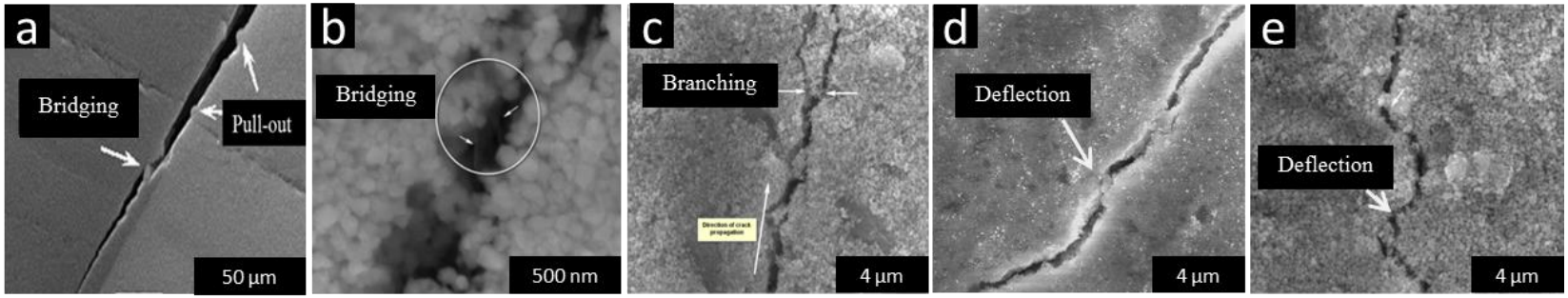 Crack bridging, crack deflection and crack branching are the main toughening mechanisms observed in YSZ reinforced with 0.2 and 0.3 wt. % graphene platelets.
0.5	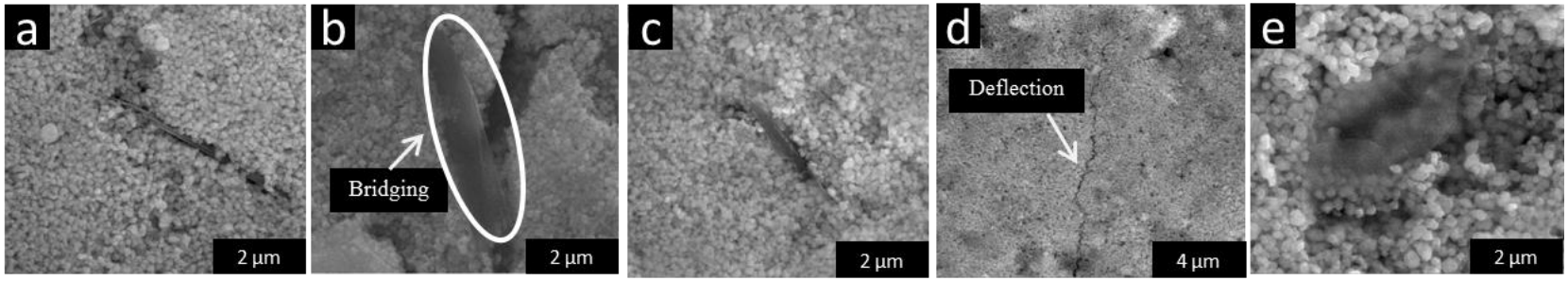 Crack bridging and crack deflection is the main toughening mechanisms observed in YSZ reinforced with 0.5 wt. % graphene platelet although some minor graphene pull-outs is also noticed (e).

1

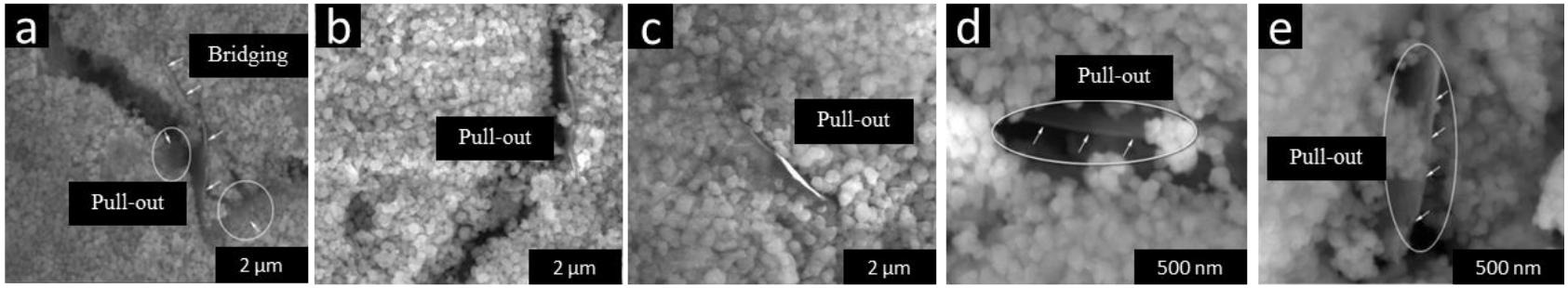

Graphene pull-outs are the major toughening mechanisms observed in YSZ reinforced with 1 wt. % graphene although crack bridging phenomenon where observed in some cases.

2

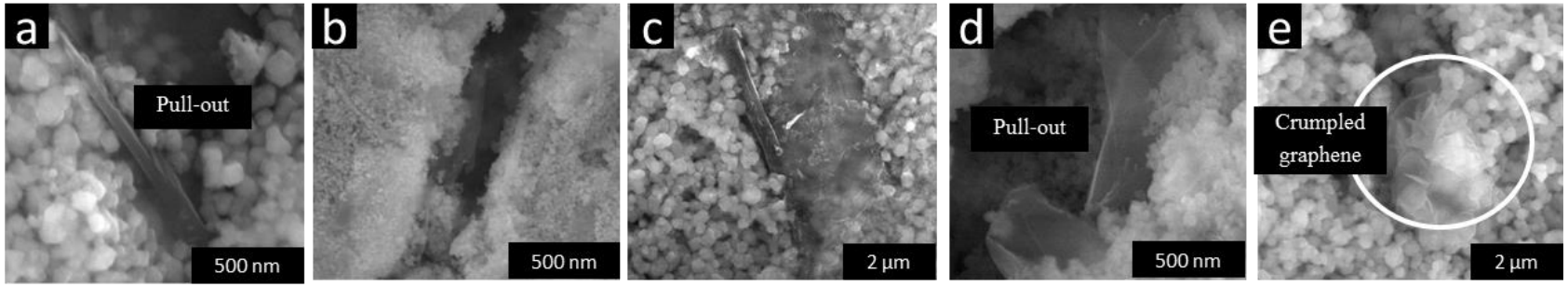

Graphene pull-outs are the major toughening mechanisms observed in YSZ reinforced with 1 wt. % graphene. However, formation of pores in the grain boundaries between graphene platelets and YSZ matrix were significant.

4.3.1.4 Densification behaviour

The variation in relative density of YSZ-Gr composites is depicted in Figure 4.7. Relative density refers to density achievable compared to the theoretical density of the composite, which is also a measure of amount of pores. A higher relative density is desirable to develop ceramics with high mechanical strength. In identical processing conditions, the average relative densities of monolithic YSZ and composites below 0.5 wt. % of graphene are approximately 89 %. However, the relative densities of YSZ reinforced with 1 wt. % and 2 wt. % graphene exhibit the highest relative densities of approximately 94.2 % and 95.1 % respectively. SEM micrographs from the surface of YSZ and YSZ-Gr composites, as depicted in Figure 4.12, shows that monolithic YSZ exhibited uniform porosity (relative density $\approxeq$ 88 %) with average grain size of 145 nm while all the YSZ composites reinforced with 0.2, 0.3 and 0.5 wt. % graphene have comparable density of approximately 90 % and average grain size of approximately 170 nm (Table 4.1). The YSZ-Gr composites reinforced with 1 and 2 wt. % graphene exhibits dense microstructure and various grain pull-out depressions from fracture surface of composites as shown in Table 4.2 with the average grain size of approximately 190 nm. SEM micrographs have depicted the distribution of graphene pull-outs at the grain boundaries and the reinforcement of graphene platelets for 1 and 2 wt. % in YSZ. In Figure 4.7, all ceramic composites cured with PDC resin displayed higher relative density than that of without curing with PDC resin, suggesting PDC resin plays a role in sealing pores within ceramic composite.

Although the exact nature of densification mechanism in ceramic composites contain graphene is not fully understood, it is nonetheless plausible to claim that graphene promotes early stage particle rearrangement of YSZ attributed by its self-lubricating

effects. In the later stages of sintering the composites, graphene functions as a sintering aid which assists in densification of ceramics [76].

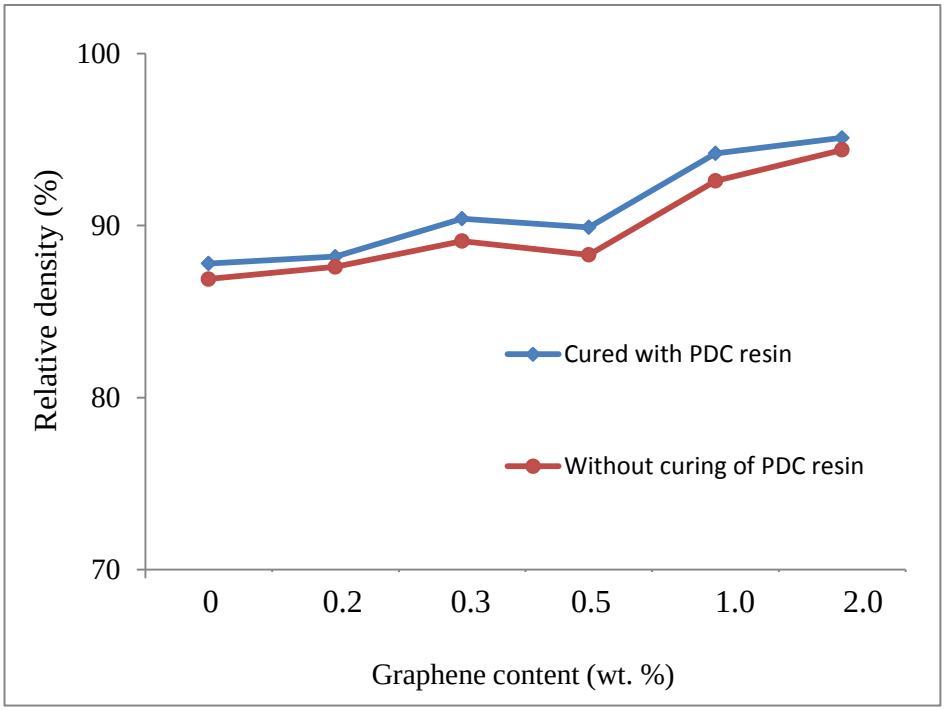

Figure 4.7: Variation in relative density of YSZ-Gr composites (cured and non-cured with PDC resin) with different wt. % graphene.

4.3.1.5 Electrical conductivity

In the present study, electrical conductivity of YSZ sintered at 1200°C measured at room temperature is 2.8 x 10^{-9} S/cm. Upon incorporation of 0.2 wt. % graphene, the conductivity increased by 3 orders of magnitude to 10^{-6} S/cm. As apparent from Figure 4.8, the composite displays a percolation threshold below 0.5 wt. % and achieved maximum value of 2.8 S/cm for filler content of 2 wt. %. Table 4.3 shows the comparison of electrical conductivity values for different nanofiller content obtained in this study with the published literature.

Table 4.3: Electrical conductivity value obtained in this study and that reported in published literatures.

Matrix material	Nanofiller type	Nanofiller content (wt. %)	Electrical conductivity (S/cm)	Ref.
Si_3N_4	Graphene platelets	17.6*	40	[138]
SiC	Few layer graphene	2.8*	1.02	[70]
ZrO_2	Graphene platelets	3	0.98	[100]
YSZ	Graphene platelets	2	2.8	Current study

(*when loading was reported in volume percent, the density of bulk graphite (2.2 g/cm^3) was used to convert to a weight percent loading)

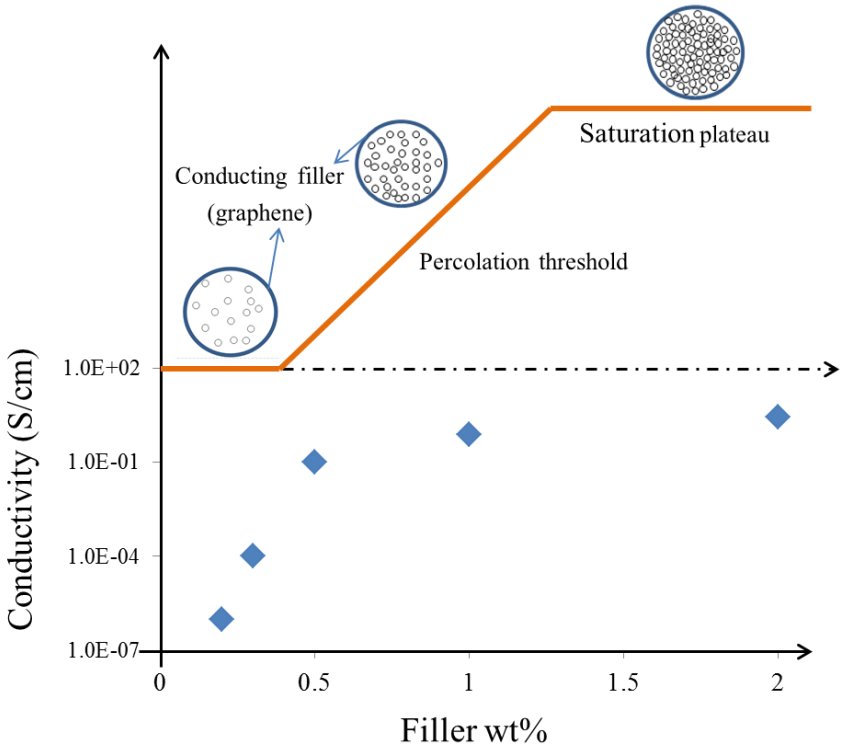

Figure 4.8: Electrical conductivity of YSZ-Gr at varied graphene loading.

The electrical conducting behaviour of ceramics incorporated with conducting fillers, such as graphene can be explained using the percolation theory and conducting mechanism. As graphene content is gradually increased, the resultant YSZ composite will experience an insulator to conductor transition. At certain graphene content,

referred to as the critical filler content, the measured electrical conductivity will increase significantly up to several orders of magnitude due to the formation of continuous/conducting paths. This critical point is known as percolation threshold and conducting networks in ceramics will be formed only when the content of conducting fillers is above this threshold. Referring to Figure 4.8, the percolation threshold for YSZ-Gr composite was below 0.5 wt. %. The conductivity nears saturation and attained a maximum electrical conductivity value of 2.8 S/cm for filler content of 2 wt. %. The incorporation of graphene into YSZ enables the ceramic composite to be electroconductive due to graphene's large specific area and exceptional electrical conductivity [36]. Presence of graphene facilitates formation of conducting networks and transforms the insulating YSZ ceramic to a conducting composite at low graphene content.

4.3.2 Influence of stirring speed and time on distribution and mechanical properties of YSZ reinforced graphene composite

The optimum graphene loading for preparation of YSZ-Gr composite was obtained from Section 4.3.1; where the composites were prepared using 1 wt. % graphene platelets.

4.3.2.1 *Effect of stirring speed and time on microstructure*

For most applications, homogenous distribution of graphene within the ceramic matrix is desirable for optimum mechanical properties. To achieve homogenous distribution of graphene within the ceramic matrix, process parameters associated with stir casting method must be studied. Thus, it is essential to investigate the influence of stirring speed and time on distribution of graphene within the ceramic matrix. The stirring speeds have been varied from 300, 400, 500, 600 and 700 rpm whereas stirring time was varied from 10, 14, 18 and 22 hours. Samples for microstructure analysis were taken for each varied parameter to show the graphene distribution. Microstructural characterization revealed the distribution of graphene in YSZ and the presence of porosity. From the microstructural analysis, it was ascertained that stirring speed has considerable effect on distribution of graphene platelets. Homogenous distribution of graphene was achieved at higher stirring speeds. This may be due to the additional energy applied by the stirrer at higher rpm, where increase in speed resulted in higher kinetic energy applied over the ceramic matrix. The energy transferred by the stirrer to the ceramic matrix is sufficiently high to forcefully disperse graphene platelets within the ceramic matrix against the effect of agglomeration. Besides, stirring time is another deciding factor for distribution of graphene platelets within the ceramic matrix. From the SEM analysis shown in

Figures 4.9-4.13, clustering of graphene has been identified in some localized region in the matrix after 10 hours of stirring. It should be noted that even after increasing stirring speed, 10 hours of stirring was ineffective to produce homogenous graphene dispersion. Increasing stirring time to 14, 18 and 22 hours witnessed better graphene distribution in comparison to 10 hours of stirring. Therefore, higher stirring time with increasing speed resulted in better distribution of graphene platelets within the YSZ matrix.

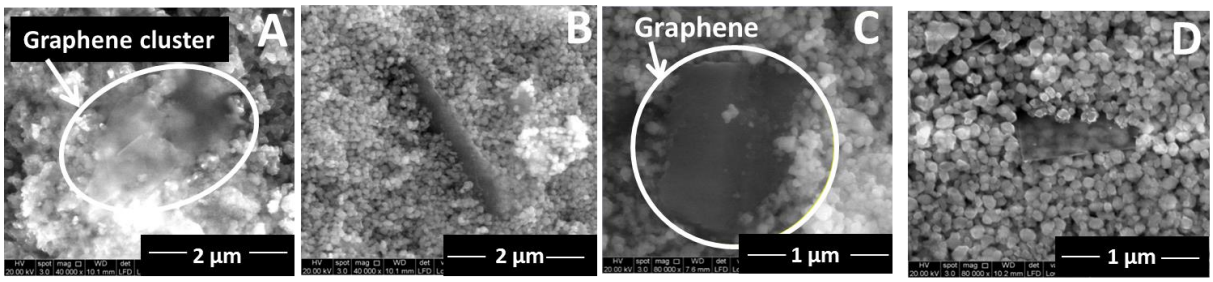

Figure 4.9: Microstructure of YSZ-Gr composites fabricated at 300 rpm and varied stirring durations of (A) 10 hours (B) 14 hours (C) 18 hours and (D) 22 hours.

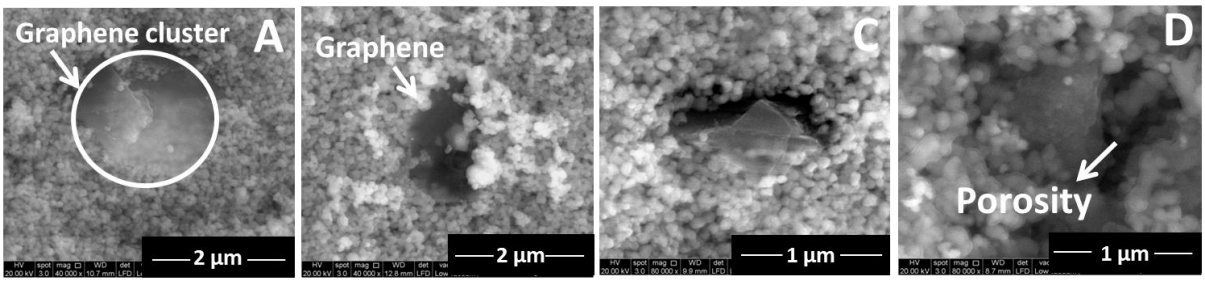

Figure 4.10: Microstructure of YSZ-Gr composites fabricated at 400 rpm and varied stirring durations of (A) 10 hours (B) 14 hours (C) 18 hours and (D) 22 hours.

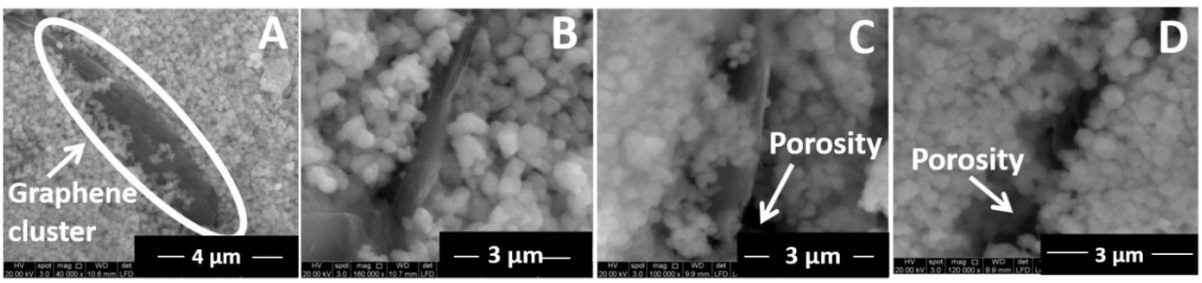

Figure 4.11: Microstructure of YSZ-Gr composites fabricated at 500 rpm and varied stirring durations of (A) 10 hours (B) 14 hours (C) 18 hours and (D) 22 hours.

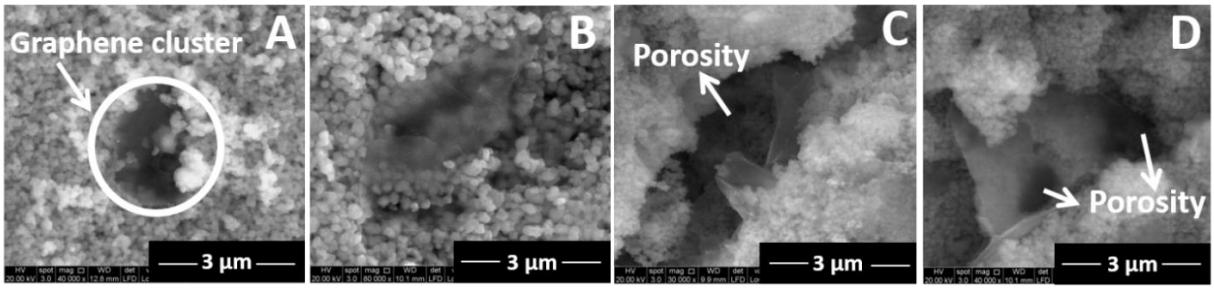

Figure 4.12: Microstructure of YSZ-Gr composites fabricated at 600 rpm and varied stirring durations of (A) 10 hours (B) 14 hours (C) 18 hours and (D) 22 hours

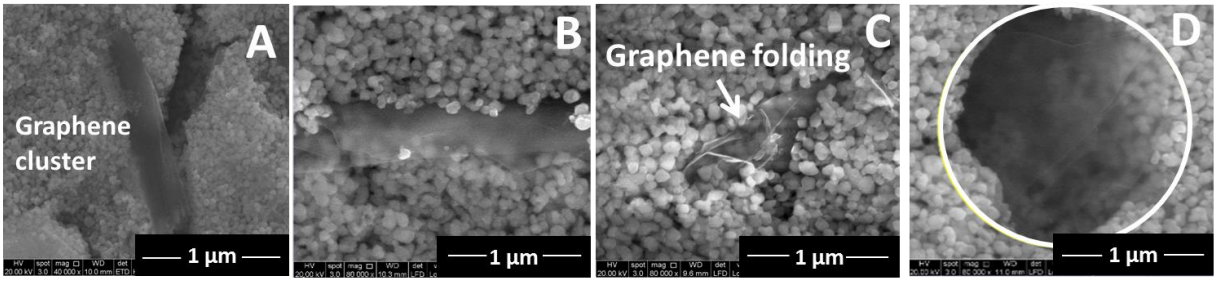

Figure 4.13: Microstructure of YSZ-Gr composites fabricated at 700 rpm and varied stirring durations of (A) 10 hours (B) 14 hours (C) 18 hours and (D) 22 hours.

However, it was observed that increasing stirring speed (>500 rpm) and stirring duration (>14 hours) resulted in porosity formation within the composite. Three types of porosity were identified: (a) porosity associated with ceramic particle (b) porosity associated with graphene clusters and (c) gas porosity (Figure 4.14). These porosities occur due to the following reasons:

i. Shrinkage during solidification; where pressure gradient is insufficient to overcome resistance to fill the voids
ii. Pre-porosity due to incomplete infiltration (with PDC resin, RD212a)
iii. Air bubbles entering the slurry and gas entrapment during stirring of ceramic suspension

Further analysis showed that stirring speed exhibited linear correlation with porosity content of the ceramic composite (Figure 4.15). The increased porosity with increasing stirring time is due to the increased gas entrapment and oxidation of ceramic suspension.

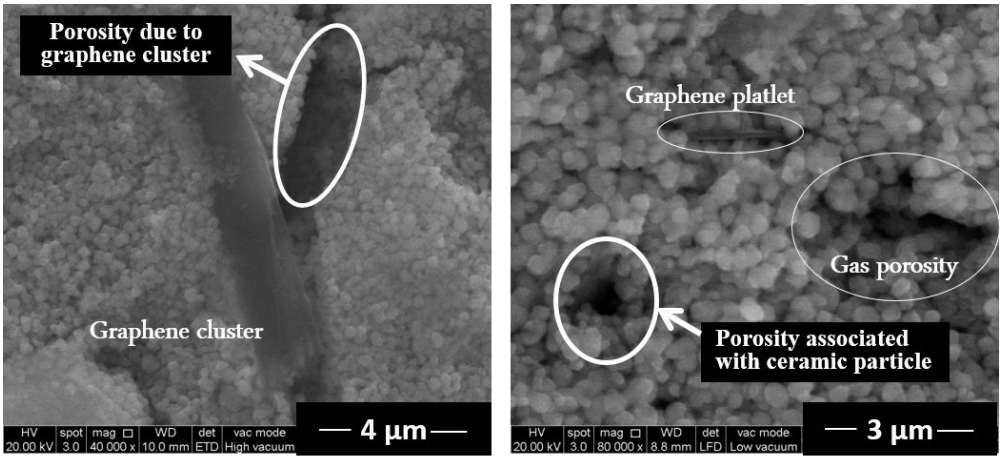

Figure 4.14: SEM micrograph of typical porosities in YSZ-Gr composites.

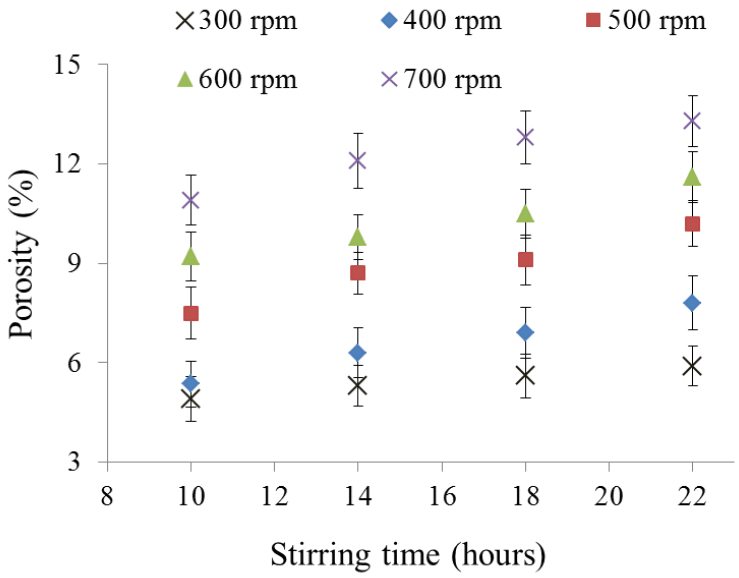

Stirring speed (rpm)	Stirring duration (hours)	Porosity (%)
300	10	4.91± 0.68
	14	5.32±0.61
	18	5.61±0.66
	22	5.94±0.59
400	10	5.35±0.69
	14	6.32±0.75
	18	6.91±0.78
	22	7.83±0.81
500	10	7.51±0.78
	14	8.73±0.64
	18	9.10±0.76
	22	10.21±0.69
600	10	9.22±0.73
	14	9.83±0.68
	18	10.51±0.72
	22	11.64±0.77
700	10	10.91±0.76
	14	12.14±0.83
	18	12.83±0.79
	22	13.33±0.76

Figure 4.15: Porosity as a function of stirring speed and duration.

4.3.2.2 *Effect of stirring speed and time on mechanical properties*

Figure 4.16 shows the effect of stirring speed and time on hardness and fracture toughness values. At lower stirring speed (300 rpm), hardness and fracture toughness values were minimal due to graphene agglomeration. When stirring speed was increased to 500 rpm, agglomeration of graphene platelets was prevented and optimum mechanical properties were achieved. Increasing stirring speed to 700 rpm induced higher porosity formation which results in weaker mechanical properties of ceramic composites. The dependence of mechanical properties such as fracture toughness (K_{ic}) and hardness (H) on porosity can be described using Eq. [4.4] and Eq. [4.5] respectively [188,189];

$$K_{ic} = K^{o}{}_{ic} e^{1/2AP} \quad [4.4]$$

$$H_x = H_o(1-P)^2 e^{-BP} \quad [4.5]$$

where P is the porosity, A and B are the constants associated with the surface energy, K_{ic} and H are the fracture toughness and hardness of specimen while $K^{o}{}_{ic}$ and H_o are the fracture toughness and hardness of fully dense material respectively. Eq. [4.4] and [4.5] ascertains that the hardness and fracture toughness generally decreases with increasing porosity within the material.

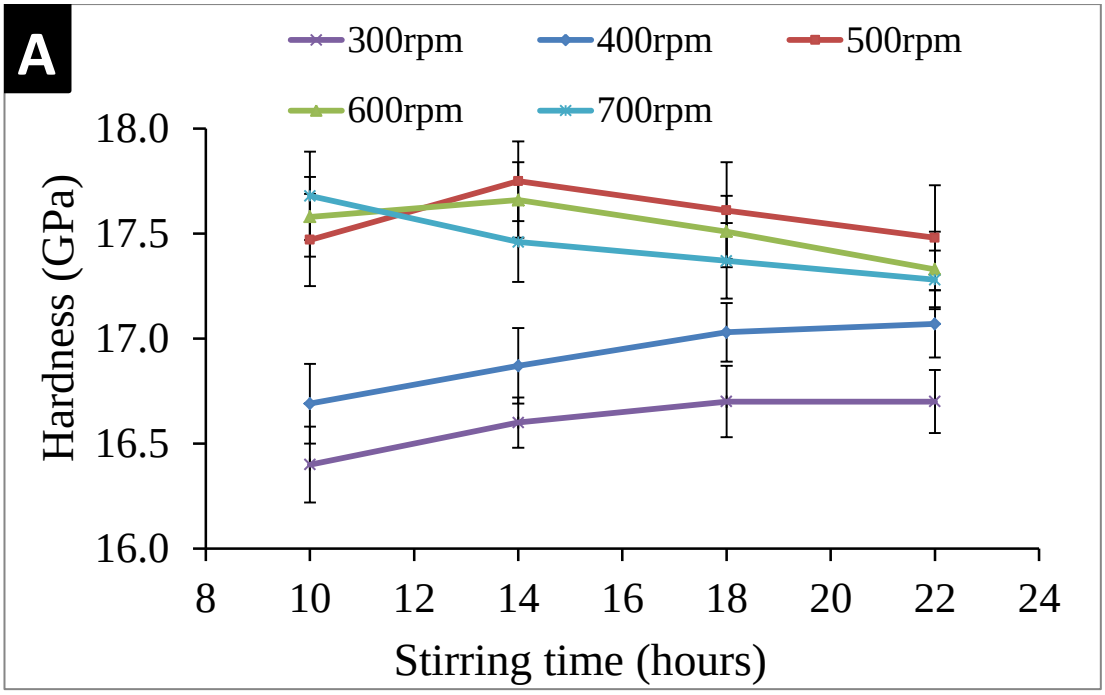

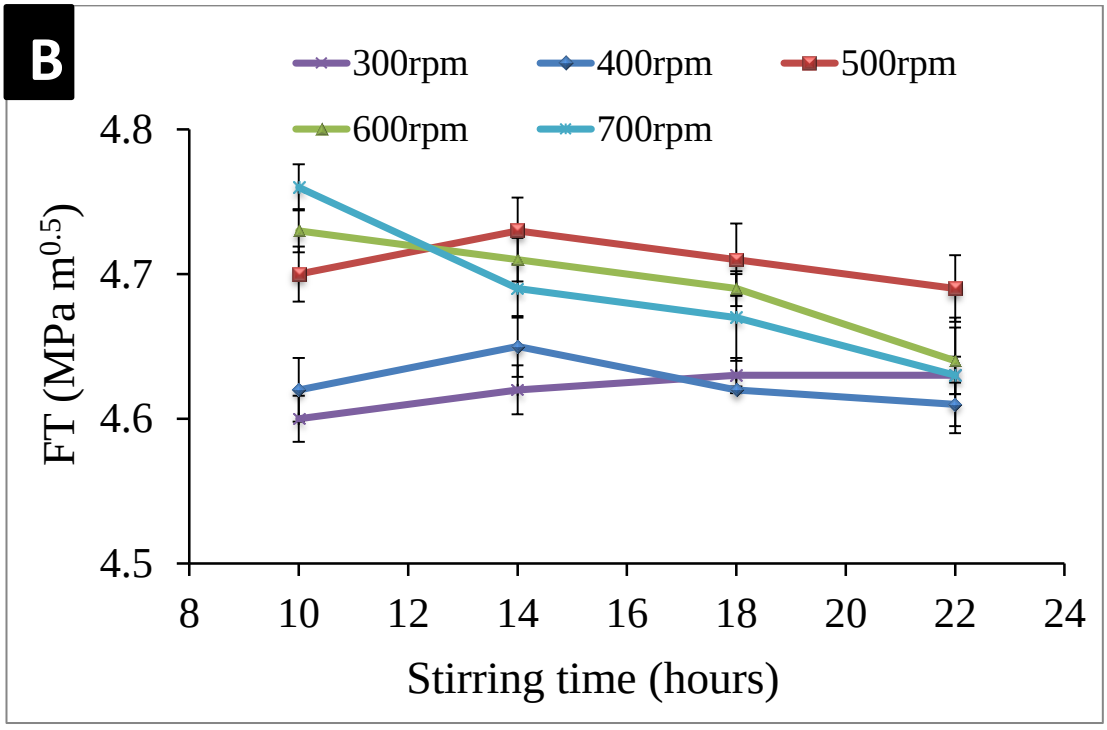

Figure 4.16: Mechanical properties of ceramic composites reinforced with 1 wt. % graphene at different stirring times and speeds: (A) hardness, H and (B) fracture toughness, FT.

The inverse proportion relationship between hardness and porosity content is described in Figure 4.17. If the hardness values obtained in the present study was extrapolated asuming zero porosity, the hardness equals 19.37 GPa (500 rpm), 19.25 GPa (600 rpm) and 19.21 GPa (700 rpm). These values are larger than the the samples with porosities after 14 hours of stirring (17.75 GPa at 500 rpm, 17.66 GPa at 600 rpm and 17.46 GPa at 700 rpm). Similar findings have been made in relation to hardness and porosity content of yttria tetragonal zirconia polycrystal (Y-TZP) by Lin et al. [190]. The measured hardness or toughness values for highly toughened materials is dependent on the porosity distribution within the composite. Since the same function (f) of porosity (P) controls most mechanical properties (M) of ceramic composites, a general form of these equations can be proposed as below where M_o is the mechanical property of the fully dense material;

$$M = M_o f(\mathrm{P})$$

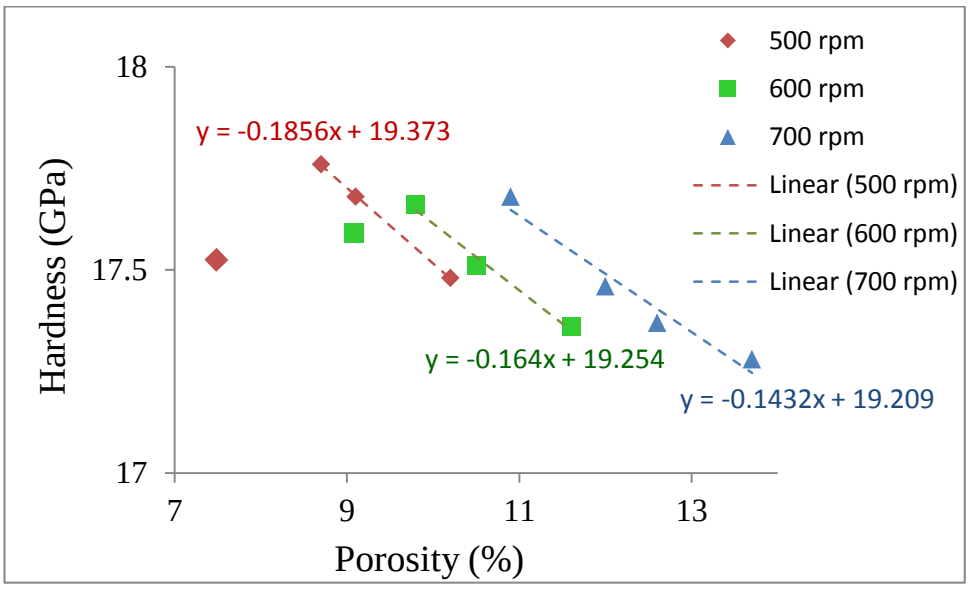

Figure 4.17: Influence of porosity on the hardness of ceramic composites at higher stirring speeds (500, 600 and 700 rpm).

In graphene based ceramic composites, specimen failure arises from the formation and growth of pores at the reinforcement-matrix interface (Figure 4.18) during solidification process [191]. These pores are the first step in formation of fatigue cracks. In hardness test, porosity develops in a particular region of ceramic composite when stress is applied. This leads to decrease in hardness and toughness of graphene based ceramic composites.

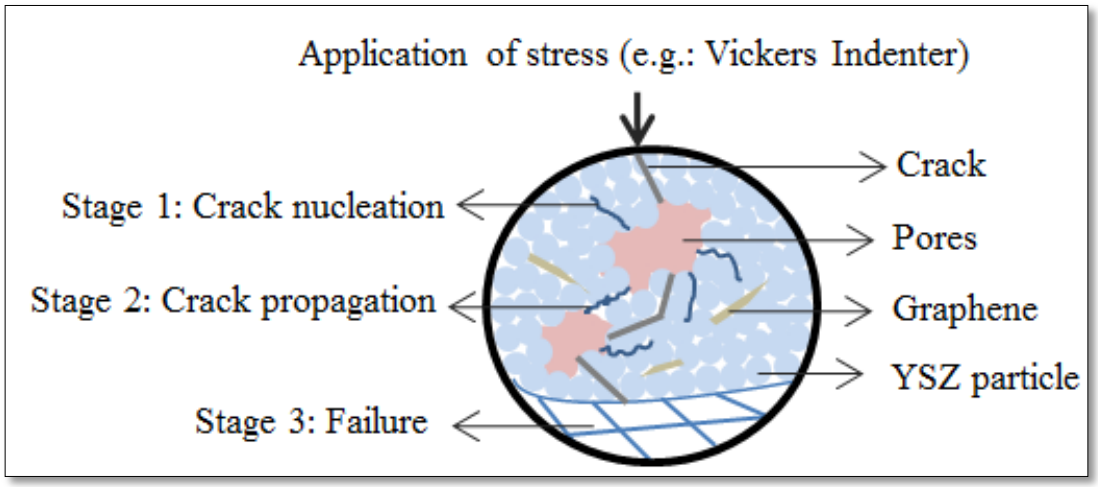

Figure 4.18: Schematic illustration on failure due to crack (from pore formation) in graphene based ceramic composites.

Figure 4.19 (a-d) shows in plane crack paths originating from Vickers indentations on the composites after stirring at 500 rpm. The crack paths of the nanocomposite shows both straight and tortuous regions which indicates that the fracture is a mixture of intergranular and transgranular modes. Graphene platelets showed higher tendency to agglomerate and overlap at shorter stirring duration (10 hours). As a result of agglomeration, the amount of large pores between matrix grains and thick graphene platelets increased which leads to poor interfacial bonding and reduced mechanical properties. This finding is in agreement with Liu et al. who have reported that large pores are origins of fracture and reduced strength of ceramic composites

[118]. In composites prepared after stirring at 500 rpm for 14 hours, crack deflection and graphene pull-out were observed as the main toughening mechanism and presence of graphene agglomerates were significantly reduced. Increasing the stirring speed to 600 and 700 rpm led to a more wider crack path and toughening mechanism such as crack bridging were discovered. However, these composites showed structural defects such as narrowing and breakage of graphene platelets (Figure 4.19d) which led to degraded mechanical strength of the composite. The defects may originate during processing of the composite; where high stirring speed provided substantial kinetic energy which produced defective graphene platelets.

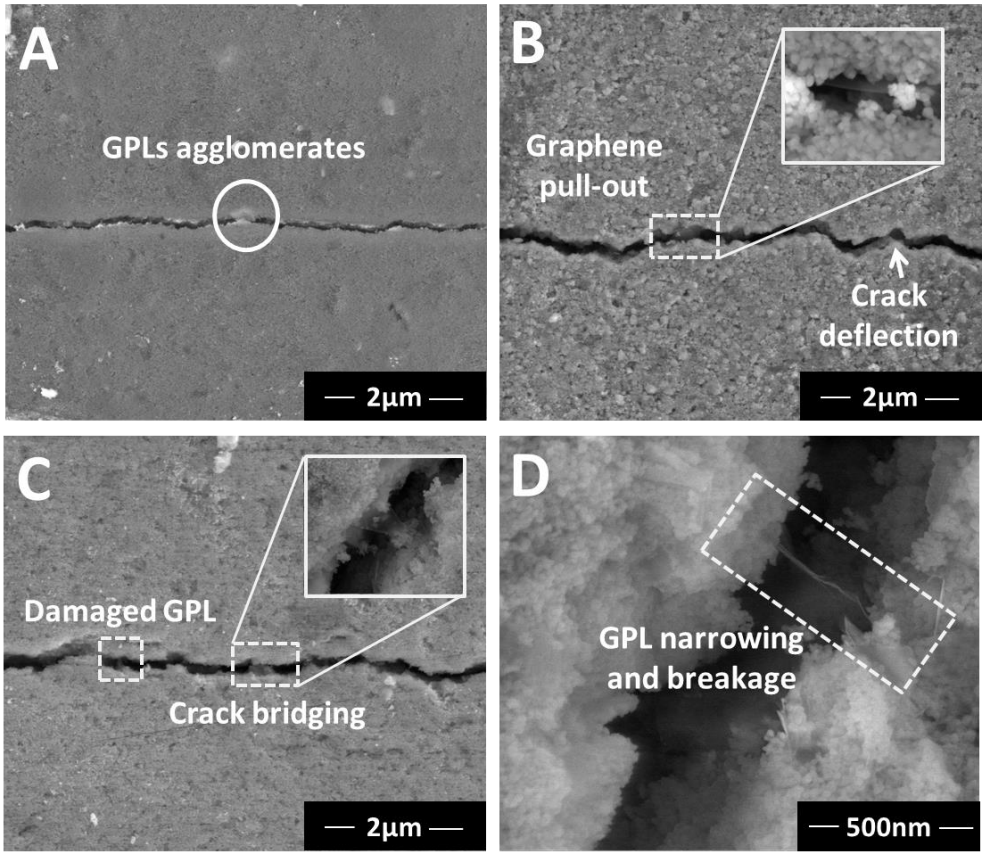

Figure 4.19: SEM images of crack paths (created by indentation) of YSZ-Gr prepared after stirring at 500 rpm for (a) 10 hours (b) 14 hours (c) 18 hours and (d) damaged GPL by narrowing and breakage after stirring for 18 hours. (Insights correspond to respective toughening mechanism)

4.3.3 Suitability of material in space system

4.3.3.1 *Dynamic mechanical analysis (DMA)*

YSZ ceramics have excellent refractory properties and high strength which make them ideal candidate for aerospace systems. One of the factors impeding the implementation of this material is their poor damping behaviour. Ceramics that are utilized in propulsion devices are subjected to a barrage of shock waves. These shock waves are unsteady phenomena which impart impulse forces onto the surface generating them. As such, damping of such impulsive forces is vital to prevent accumulative damage. Dynamic mechanical analysis (DMA) is a useful tool to study the damping behaviour of ceramics.

DMA was performed on YSZ ceramic reinforced with graphene platelets. The addition of graphene platelets enhanced damping behaviour (tan δ) at frequencies of 25 Hz and 50 Hz by up to 280 %. Our approach utilized addition of graphene platelets as reinforcement for YSZ to enhance the damping behaviour. The damping behaviour was improved through energy dissipating mechanism such as GNP pull-outs which has been reported previously. The motive behind using graphene as a dampening phase was due to the excellent damping behaviour of multi-layer graphene. The values of tan δ for different YSZ-Gr composite are presented in Figure 4.20. It can be seen that graphene platelets improved the damping behaviour of all composites at all frequencies used except at 100 Hz. This phenomenon is due to the frequency (100 Hz) exceeding the recovery time needed for damping behaviour to be effective. The effect of 0.5 wt. % graphene platelets in YSZ ceramic is negligible since there is not enough graphene to make an impact. The YSZ reinforced with 1 wt. % graphene platelets show significant improvement in damping behaviour. This composite demonstrated damping improvement of ≈280 % over monolithic YSZ at a

frequency of 25 Hz. The values of tan δ obtained are affected by the distribution of graphene platelets within the YSZ matrix. In our previous study, scanning electron microscopy images revealed that YSZ reinforced with 1 wt. % graphene platelets are widely dispersed and distributed uniformly throughout the sample; forming a networked structure. However, YSZ reinforced with 2 wt. % graphene platelets were poorly distributed and many agglomerates were identified. Therefore, it should be noted that mere addition of graphene platelets is not enough to improve the damping behaviour if the amount and dispersion of graphene is not adequate.

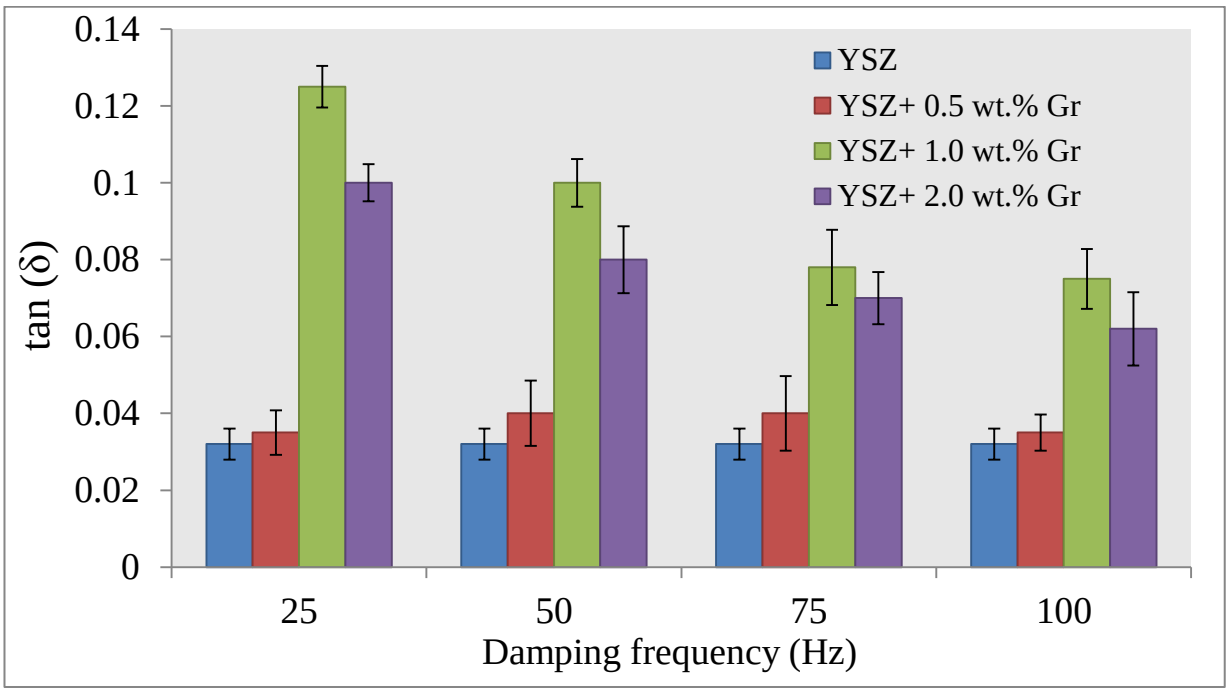

Figure 4.20: Damping behaviour (tan δ) of YSZ–graphene platelets composites at different frequencies.

4.4 Conclusion

In conclusion, YSZ reinforced graphene ceramics were successfully prepared by gel casting method. Using CTAB as surfactant for dispersion, well-dispersed graphene-ceramic composites were achieved. Experimental results show that 1 wt. % of well-dispersed graphene prepared after stirring at 500 rpm for 14 hours successfully enhanced mechanical properties of YSZ; where fracture toughness and hardness of the composites increased by 20.31 % and 25.78 %. Various toughening mechanism including crack deflection, crack bridging and crack branching were observed in the composites. Besides, DMA analysis has shown the feasibility of YSZ-Gr as a material for space applications owing to their exceptional damping behaviour. These findings establish graphene as an effective reinforcing agent to prepare tough, electro conductive and shock resistant ceramic composites that can be exploited for use in micropropulsion devices.

Chapter 5

Design, fabrication and performance evaluation of ATZ-graphene based MEMS scale microthruster

5.1 Introduction

Microelectromechanical system (MEMS) technology has initiated the miniaturization of conventional propulsion system by reducing system mass and volume significantly. Three motivations behind the miniaturization and development of micro-spacecraft are [143,192]:

I. Reduce mission cost and increase launch rates by reducing launch mass
II. Reduce mission risk and increase mission flexibility [launching clusters of micro-spacecraft rather than a large conventional space craft]
III. Discover new application areas of space technology

In fact, various MEMS based micropropulsion systems have been investigated. For example, bi/monopropellant microthruster, cold gas microthruster, decomposed monopropellant and solid propellant microthruster [143,192–195]. Although development of micropropulsion systems through MEMS technology was considerably well established, it was not free from limitations. Their efficiency was low due to the high thermal conductivity of silicon- the main structural material commonly used in MEMS fabrication technique (Table 5.1). Initiative was taken to improve thermal insulation of the system by reducing contact area with combustion area; however, it incurred more complex fabrication steps.

Table 5.1: Properties of materials (silicone and ceramics) used for developing micropropulsion devices.

	Silicone	Ceramic (alumina)
Compressive strength (MPa)	30	5500
Fracture toughness (MPa.$m^{1/2}$)	0.7	5
Modulus of rupture (MPa)	5.5	800
Maximum service temperature (K)	225	2114
Thermal conductivity (W/mK)	130	38.5
Corrosion resistance	✓	✓
Design freedom	X	✓

In this chapter, we demonstrate the feasibility to develop a chemical microthruster through a new fabrication route. Alumina toughened zirconia (ATZ) was used as the structural material to fabricate microthruster while addition of graphene provided conductive paths to combustion chamber to decompose propellant. The fabrication procedures are described in Section 5.2. The design, characterization and testing of microthruster at different propellant flowrates are also detailed. To the best of our knowledge, the use of ATZ and graphene to fabricate a MEMS scale microthruster has not been reported in open literature.

5.2 Fabrication of thick ceramic layers

5.2.1 Micro-molding and gel casting

PDMS is an elastomer which is flexible and soft with low interfacial energy; where parts can be released easily. Besides, the soft-lithography technique allows fabrication of microstructures in μm scale. A master mold was required to produce PDMS molds in soft-lithography. Master molds were produced via a non-conventional technique, xurography. The design patterns were drawn in graphic

design software (CorelDraw, X8). It was then sent to a cutting plotter (CE5000-60, Graphtec, U.S.A) equipped with razor knife to cut geometric design on adhesive film of 125 μm thickness. The film thickness determined depth of microstructures to be replicated onto micro-mold. Removal of unwanted parts on the film left behind a negative pattern that served as a master mold (Figure 5.1).

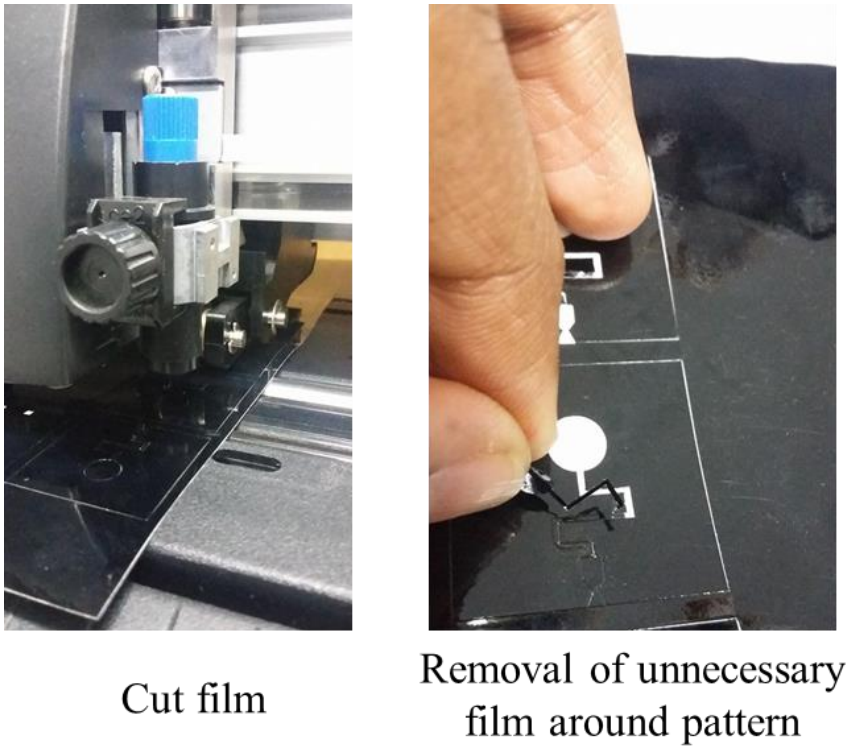

Figure 5.1: Preparation of vinyl master mold using cutting plotter.

5.2.2 Fabrication process flow

The procedure of fabricating ceramic-graphene based micropropulsion device is shown schematically in Figure 5.2;

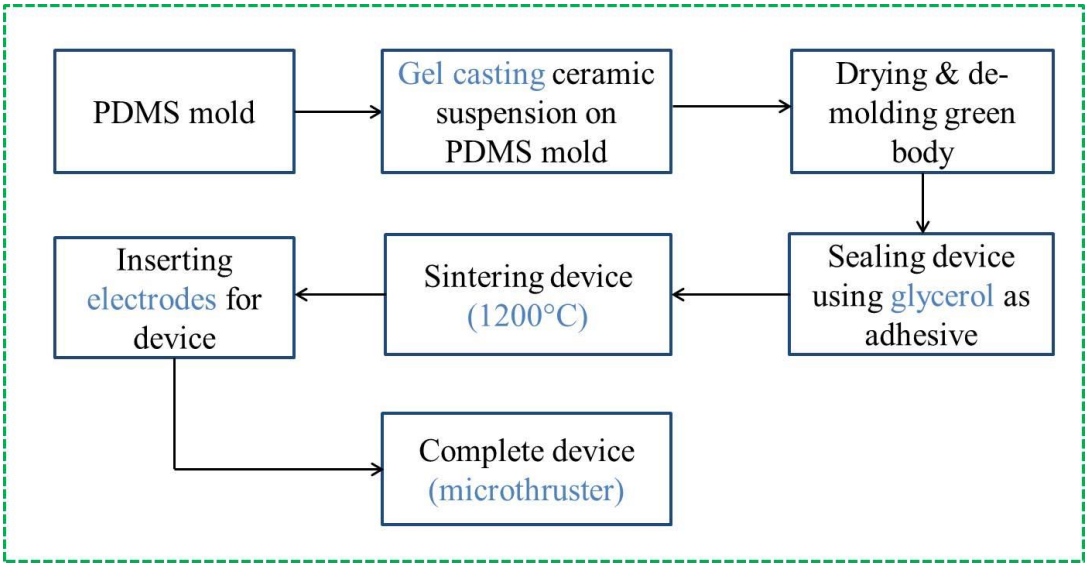

Figure 5.2: Fabrication process of MEMS scale ceramic microthruster.

- ***Preparation of PDMS soft molds***. An identical procedure as described in Chapter 3 was used to prepare PDMS soft mold. Vinyl film master mold and the replicated PDMS soft mold with microthruster design are shown in Figure 5.3.

Figure 5.3: Vinyl film master mold with geometry of microthruster design and replicated PDMS soft mold.

- ***Gel casting of ceramic suspension***. Identical procedures were used in preparation of ATZ and YSZ-Gr for gel casting. Compositions for ATZ and YSZ-Gr suspensions for gel casting are summarized in Sections 3.2.2 and 4.2.3 of this report. ATZ suspension (20 wt. % Al_2O_3) was prepared by stirring at 300 rpm for 14 hours. YSZ-Gr suspension (1 wt. % GNP) was prepared by stirring at 500 rpm for 14 hours. Polymerization initiator and catalyst were then added to initiate gelation. The ceramic suspensions were casted onto PDMS molds and heated to 50°C to accelerate gelation process.

- ***Drying and de-molding of green body***. Dried green bodies can be de-molded easily by slightly bending the PDMS molds. PDMS molds can be cleaned using ultrasonic cleaner and reused. Upon drying, holes were drilled on three selected locations as shown in Figure 5.4. These holes functions to provide connections between the macro and micro worlds. The central hole functions as inlet for propellant reservoir whereas the other two holes serve as connectors between the conductive paths and external electric pads.

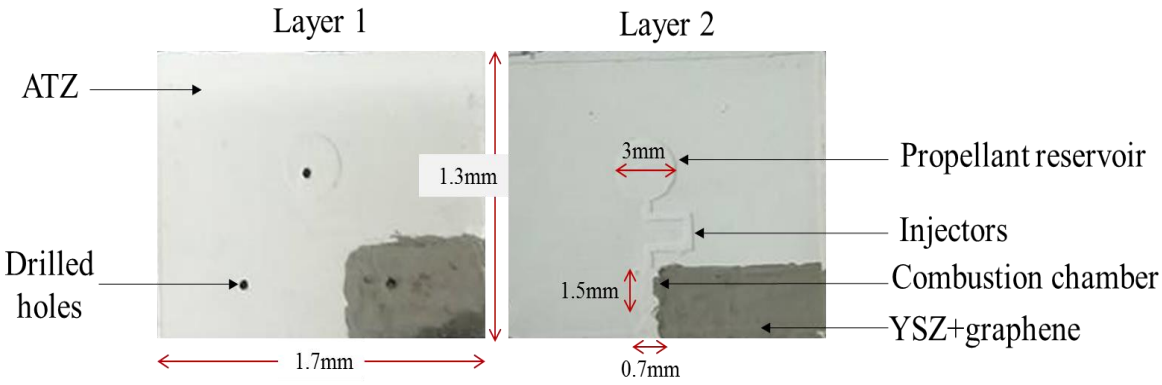

Figure 5.4: An overview of ATZ green layers after demoulding (a) layer 1 drilled with three holes (b) layer 2 depicting the successful replication of microthruster components from PDMS soft mold onto ceramic body.

- ***Sealing of device using glycerol as adhesive solution***. 85 % aqueous glycerol solution was applied as adhesive to laminate the ceramic green layers. Current ceramic layers are polyacrylamide (PAM) gels impregnated with large amount of ceramic powder. When glycerol solution was applied on the surface of ceramic, water functions as a solvent to dissolve the PAM gel; thus releasing the ceramic particles. At this stage, rearranging and particle packing occurs at the joint regions when pressed together. The subsequent heating re-initiates polymerization where PAM gel regains its binding capability. As replicated in Figure 5.4, all design patterns were replicated onto the ceramic green layer and was laminated to another flat ceramic layer to form the microthruster.

- ***Sintering and inserting electrodes.*** The laminate was loaded into a furnace (CWF1200, Carbolite, U.K), heated to 320°C and held for 1 hour to remove the binding gel. The ceramic green body were sintered via double step sintering by first ramping the temperature to 1200°C, reduced to 900°C and held for another 30 hours. Then, electrodes were inserted into the propellant reservoir and electric vials; where holes were drilled earlier in previous stage. Figure 5.5 depicts the sealed ceramic microproplsion system with a clear opening view of the micronozzle exit.

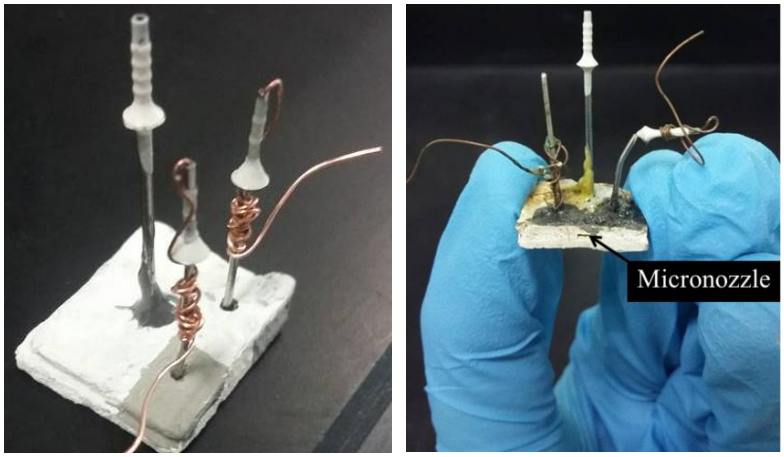

Figure 5.5: Sealed microthruster with clear opening view of micronozzle exit.

5.3 Design, concept and fabrication of microthruster

5.3.1 Prototype of microthruster

The layout of ceramic microthruster design is shown in Figure 5.6. The proposed ceramic microthruster comprises of five major components which includes the propellant reservoir, injector, electrodes, micronozzle and combustion chamber. The inlet provides the fluidic connection site between the micro and macro world. In this design, propellant is externally pumped into the reservoir which then flows through a series of microchannel (90° bends) prior entering the combustion chamber. Two conductive paths are connected to the chamber which functions to supply electrical energy to decompose propellant into its component gases. In this work, YSZ-Gr functions as the conductive paths since graphene has excellent electrical conductivity. Accelerating hot gases through the designed micronozzle creates a small thrusting force. Dimension of the microthruster was 1.7 cm × 1.3 cm.

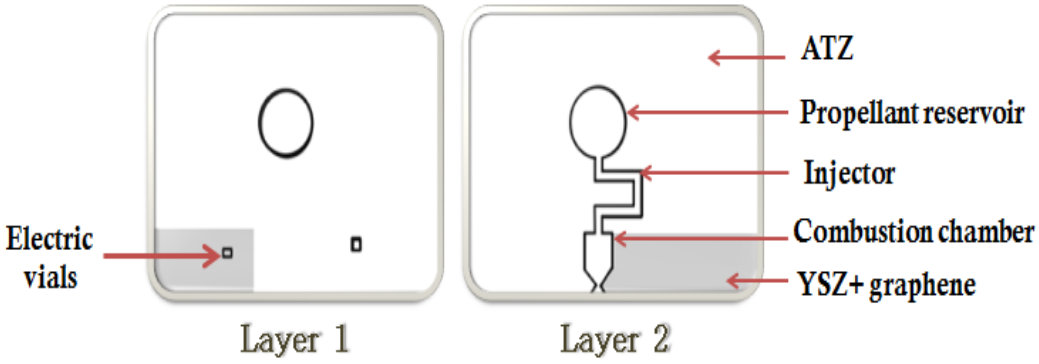

Figure 5.6: Layout of microthruster design

5.3.2 Surface contour of patterned green layer

Figure 5.7 shows the SEM images of different ceramic microthruster sections. All design features which includes; propellant reservoir, combustion chamber, injector and micronozzle were successfully molded. Besides, a closer inspection on micronozzle sidewalls revealed the ability of this technique to produce vertical sidewalls. Several geometrical irregularities were observed in the microthruster as shown in Figure 5.7a. The presence of irregularities in non-critical components of the thruster along with the significantly lower cost of xurography technique makes the irregularities to be within the tolerance limit.

Figure 5.8 shows the photographs of the master mold and ceramic microthruster at different processing steps. The dimensional shrinkage of the microthruster components after drying and sintering were clearly evident. However, to show the shrinkage ratios more explicitly, quantifying measurements on the thruster height were made and presented in Table 5.2. The relatively small shrinkage is attributed to the ability of colloidal processing route in packing ceramic particles to relatively high solid loading (70.38 %).

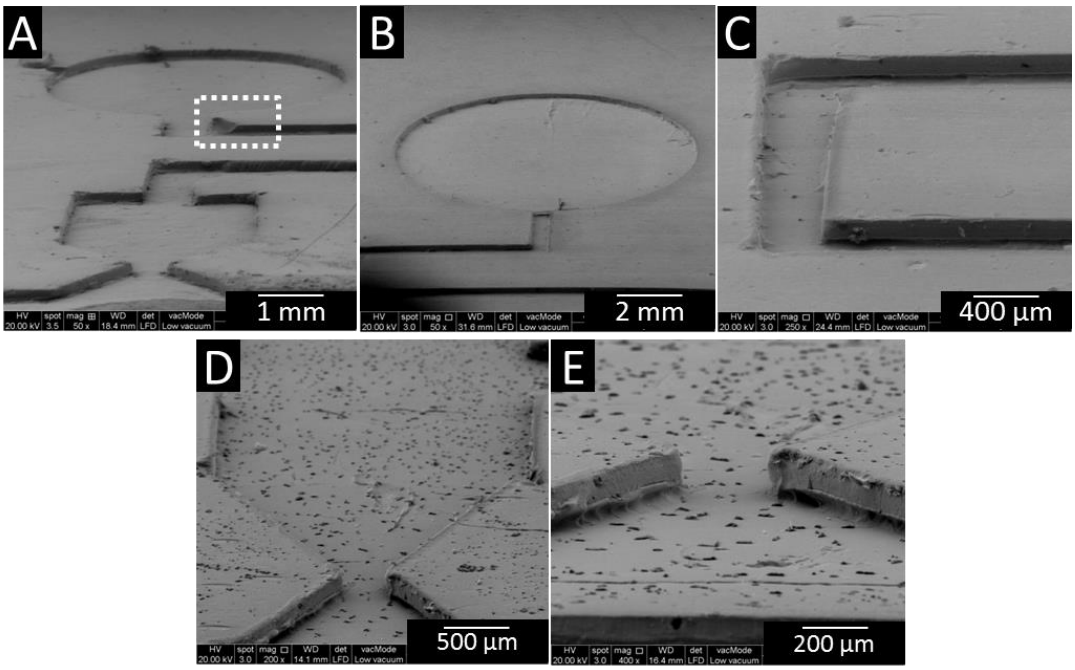

Figure 5.7: SEM images of microthruster sections (a) overall microthruster (b) propellant reservoir (c) microchannels (d) combustion chamber (e) micronozzle.

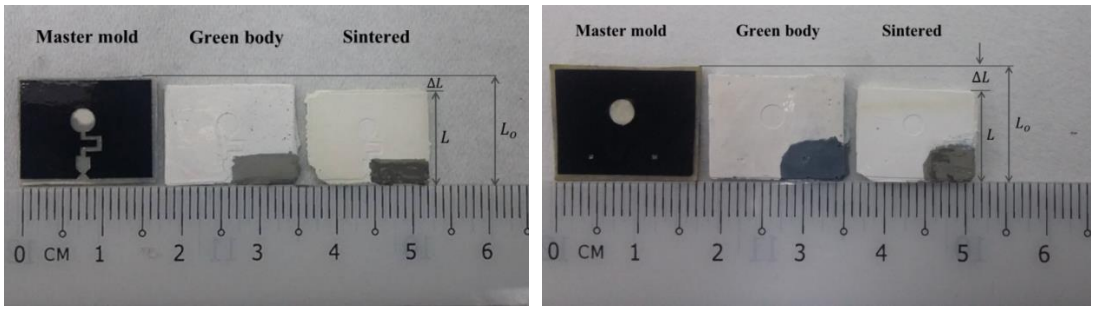

Figure 5.8: Images of master mold and ceramic microthruster after different processing stages.

Table 5.2: Measurement of the thruster height after different fabrication stages.

	Height, cm (L_o)	L/ L_o (%)
Vinyl master mold	1.30	100.00
Ceramic green body	1.24	95.38
Sintered ceramic	1.19	91.54

Drying and shrinkage of ceramic occurs in several steps; schematically shown in Figure 5.9. The as-casted body dries at a constant rate, controlled by partial vapour pressure and temperature. At this stage, the surface of the as-casted body during drying is wet since liquid flow from the interior to surface during drying. The volume fraction of ceramic particles increases continuously with evaporation of solvents until particles touch each other and no more shrinkage can occur. During this critical point, the liquid vapour interface starts to recede into the pores and drying rate decreases significantly; since transport of fluid to surface of ceramic becomes rate-limiting. When liquid in large pores has evaporated, drying rate decreases even more since diffusion of vapour from fluid trapped inside the green body becomes rate limiting. It should also be noted that although fast drying is desired in the ceramic industry, quick drying may cause cracks.

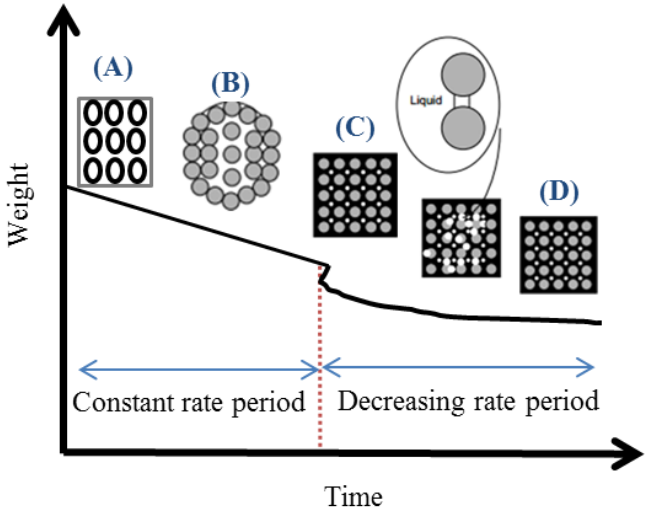

Figure 5.9: Schematic representation of ceramic layers after drying and sintering showing weight loss with time. (A) As cast (B) green body shrinkage and deformation (C) particle in contact with liquid filling the pores (D) completely sintered.

The ceramic micropropulsion system is illustrated in Figure 5.10 where comparison of size was made with respect to Malaysian 5 cent coin of 1.6 cm in diameter.

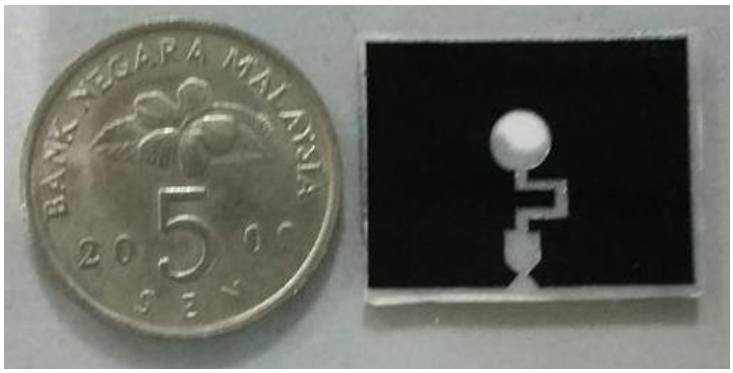

Figure 5.10: Size of ceramic micropropulsion device in comparison to a Malaysian 5 cent coin (diameter approximately 1.6 cm).

5.4 Evaluation of microthruster performance

Electrical power was supplied by DC adapter (Elektro Automatik, Malaysia) at 80 V and 0.1 A. 3 ml syringe pump was used to supply fuel (hydroxylammonium nitrate, HAN) to the microthruster at required flowrates (20, 40, 60 and 80 µl/min). Omega K-type thermocouple connected to data logger (Graphtec, U.S.A) at 100 ms sampling rate was used to obtain temperature profiles. Thrust profiles were obtained by Futek miniature load cell at 100 ms sampling rate. The load cell is sensitive and capable of sampling rate up to 0.1 ms and accuracy up to 0.0001 g; thus helping to record ambient noise under normal conditions. The load cell were placed 2 mm from the microthruster exhaust and used individually at a time. Cushion pads were used to reduce ambient noise. Blank test (load cell data without supplying fuel and electricity) was performed to collect ambient noise. Later, actual experiments were carried out to collect raw thrust data. The final readings were obtained by subtracting noise graph from thrust graph. An illustration of the experimental setup is shown in Figure 5.11.

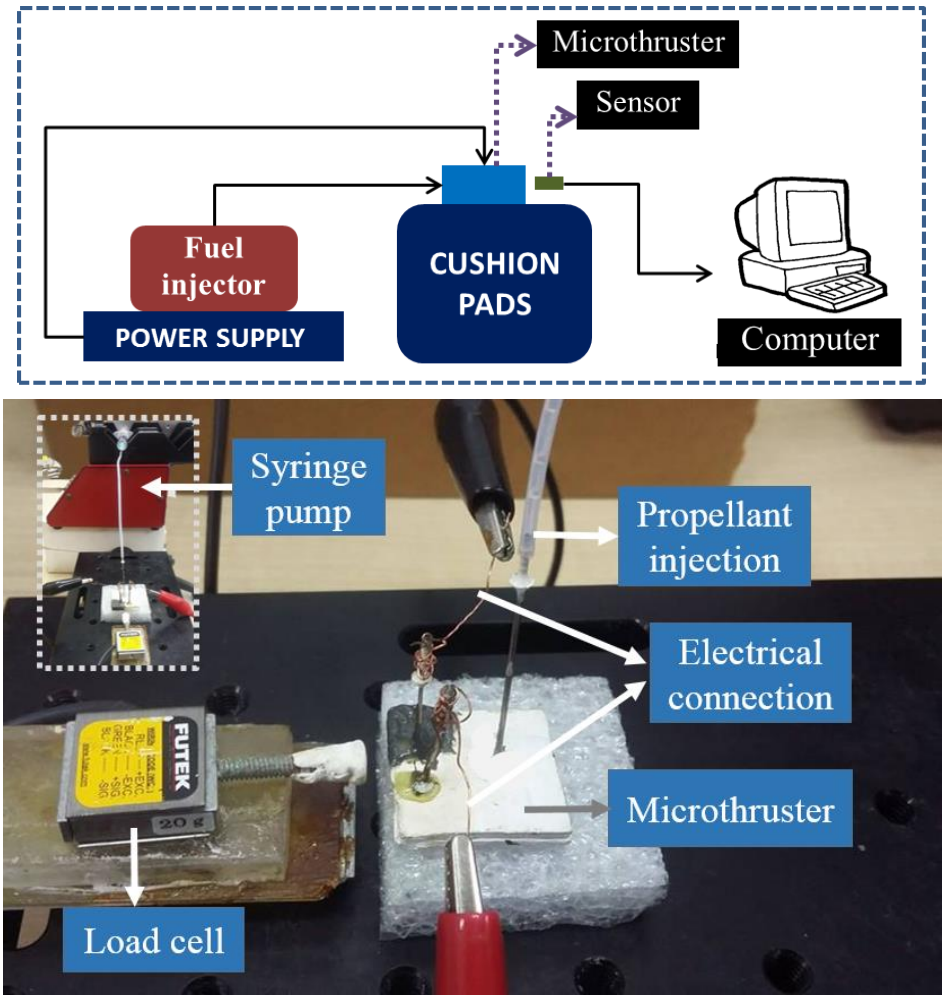

Figure 5.11: Experimental setup for thrust and exhaust temperature measurements.

5.4.1 Effect of varying propellant flowrate on thrust produced

Flowrate is an important parameter that influences the thruster performance as it impacts the decomposition phenomena of propellant (HAN). For example, optimum flowrate increases contact time between HAN and conductive YSZ-Gr surface, thereby increasing efficiency of thruster. Besides, performances of thrusters are usually evaluated in terms of thrust produced and specific impulse. Each of these measurements is dependent on the mass flowrate of propellant injected into the thruster. For example, specific impulse is a measure of thruster efficiency and is defined as the ratio of thrust to propellant flowrate;

$$I_{sp} = \frac{F}{\dot{m}} \qquad \text{[Eq.5.1]}$$

where Isp is the specific impulse measured in seconds, F is the measured thrust (N) and $\dot{m}$ is the mass flowrate of propellant (kg/s). On the other hand, the thrust produced will be equal and opposite to the rate of change of momentum of the propellant;

$$F = -\frac{d}{dt}(m_p V_{ex}) = -V_{ex}\left[\frac{d_{mp}}{dt}\right]$$

where $d_{mp}$the rate of change of propellant mass and Vex is the propellant exit velocity. Thus, by determining the optimum propellant flowrate, it will be possible to establish the trade-off between propellant requirements for enhanced thruster efficiency.

The thrust profile of ceramic microthruster obtained at different propellant flowrates (20, 40, 60 and 80 µl/min) is shown in Figure 5.12. In this study, five measurements were performed for each setting of flow rate conditions and then data were averaged to obtain mean thrust value. Moreover, the thrust measurements were repeated with other fabricated microthruster having same geometry to confirm the repeatability of measured results. The average thrust values obtained over five measurements have a variation of ± (11.12 to 16.3) mN. Maximum thrust of 180.53 mN was achieved at 60 µl/min. It is observed from Figure 5.12 that thrust force increases linearly with propellant flow rate for fixed thruster dimensions. However, maximum thrust obtained decreases at flowrate above 60 µl/min. This nature of variation is explained by the fact that at lower flow rate conditions, the amount of propellant is sufficient in respect to its exposure to the YSZ-Gr surface during its stay in the combustion chamber for reaction to complete. This condition ensures complete decomposition of

HAN in the chamber resulting in an increase of total amount of reaction product and hence the thrust force increases. However, at higher propellant flow rate, the entire propellant may have less reaction time with the conductive YSZ-Gr surface leading to incomplete decomposition. This generates constant amount of reaction products irrespective of propellant flowrate, resulting in lower thrust force. Besides, the maximum thrust at each flowrate was only obtained 60 seconds after the start of decomposition. The slow ignition is due to the time consumption of electrical power supply to reach the designated voltage upon turning on.

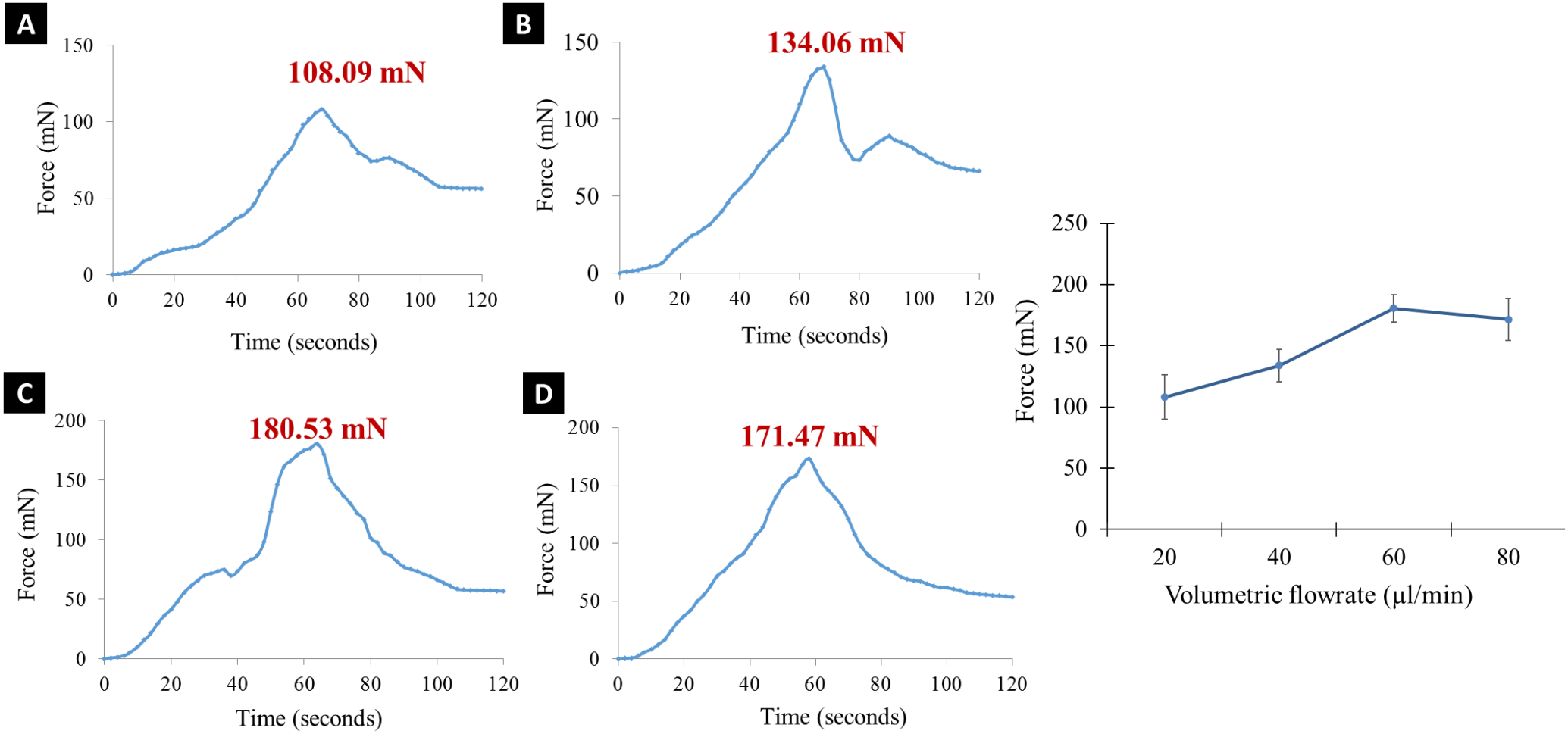

Figure 5.12: (Left) Thrust profiles of ceramic microthruster obtained at different propellant flowrates (A) 20 µl/min (B) 40 µl/min (C) 60 µl/min and (D) 80 µl/min. (Right) Maximum attainable thrust at different propellant flowrates. Thrust obtained increased with propellant flowrate (from 20 to 60 µl/min) and maximum thrust of 180.5 mN was achieved at 60 µl/min. At 80 µl/min, thrust obtained decreased to 171.4 mN.

5.4.2 Temperature profile of microthruster

Exhaust temperature is a measure of heat in the combustion chamber during propellant decomposition process where high exhaust temperature indicates efficient propellant decomposition in the combustion chamber [196]. As such, monopropellant propulsion system uses the energy from decomposition process to produce high temperature exhaust gases that are then expanded through the nozzle to obtain high velocity.

The temperature profiles of ceramic microthruster obtained for 20, 40, 60 and 80 µl/min is shown in Fig 5.13. In these temperature profiles, it was noticed that the temperature distribution was nearly uniform for all flowrates (20, 40 and 60 µl/min); however fluctuated for 80 µl/min. Approximately 30°C temperature raise from room temperature occurred within initial 25 seconds for 20, 40 and 60 µl/min. The temperature raise is due to the exothermic reaction where propellant is decomposed. As the decomposition process proceeds, the reaction rate decreases resulting in slowdown of exothermic heat generation. The temperature profile also shows that higher flowrate (80 µl/min) generates lower temperature raise due to incomplete decomposition process (improper combustion of propellant) resulting in lower exothermic heat generation [197]. The incomplete decomposition process was ascertained by the thrust profiles where maximum thrust obtained at 80 µl/min was lesser than 60 µl/min. However, it should be noted that the exhaust temperature measurement in the present study is only an indication (proof of concept) of the decomposition process occurring in the ceramic microthruster. Quantitative measurements can be performed in future by integrating temperature sensors to achieve precise control of the decomposition process.

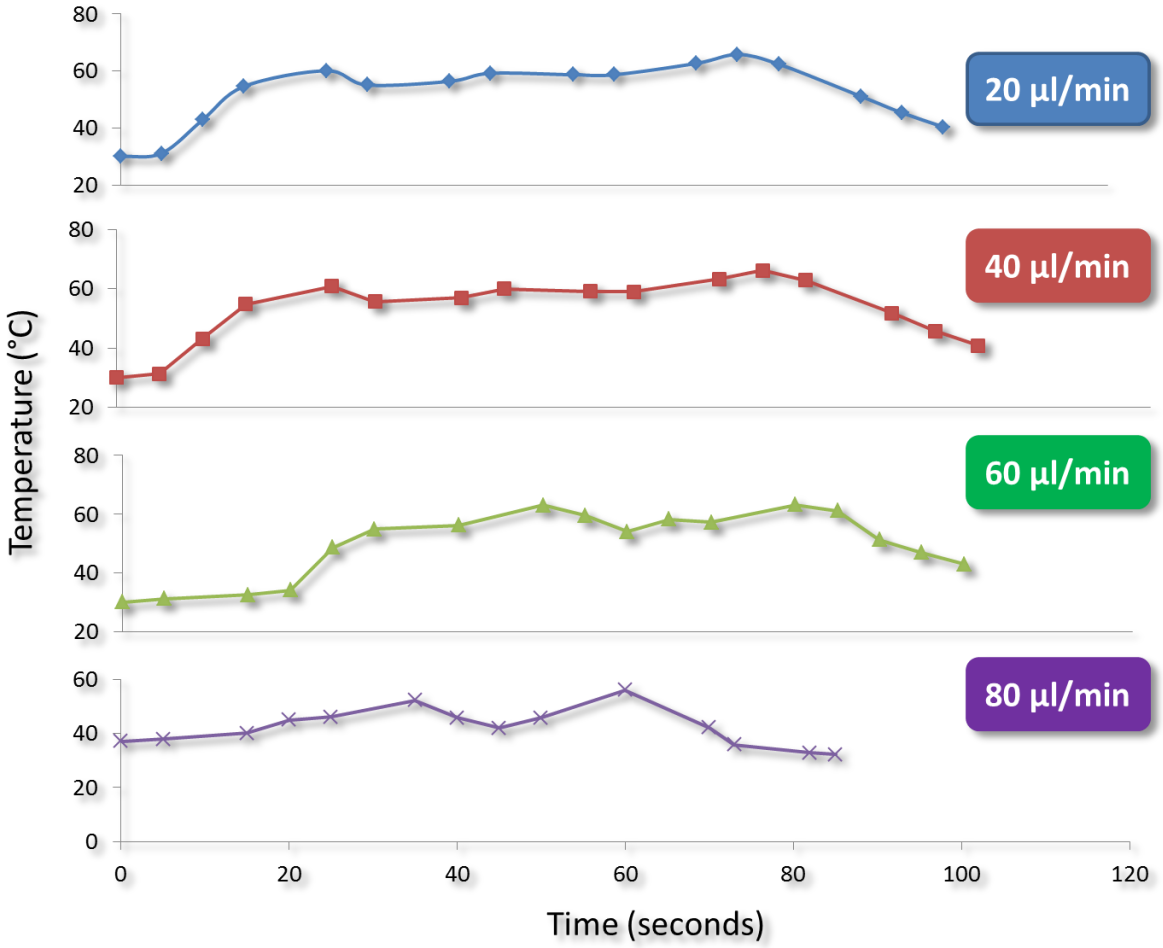

Figure 5.13: Temperature profile of microthruster at different propellant flowrate.

5.5 Conclusions

In conclusion, MEMS scale ATZ- graphene microthruster was successfully fabricated. To achieve a balance between affordability and performance, non-conventional fabrication approaches were adapted. Xurography or razor writing was used to produce the master mold in a rapid and inexpensive way. The gel-casting technique was selected to provide a rapid consolidation of the ceramic suspension. SEM analysis indicated that all design features of microthruster were successfully molded with minimal shape distortion using this technique.

In this study, thrust produced increased with flowrate of propellant (HAN). However, thrust values decreased when flowrate was increased above 60 µl/min. This was ascertained by temperature profile where higher flowrate (80 µl/min) generates lower temperature raise due to incomplete decomposition process in comparison to lower flowrates (20, 40 and 60 µl/min). This implies that sufficient contact time between HAN and YSZ-Gr surface is required for efficient decomposition of HAN. On the other hand, the proposed thruster design and its testing were successful as optimum thrust (180.5 mN) was achieved at a propellant flowrate of 60 µl/min. Although the obtained thrust values signifies the successful decomposition of propellant in the combustion chamber, more accurate thrust values can be obtained provided measurements are conducted in vacuum chamber to measure even the small changes of mass to high degree of accuracy. Nevertheless, the current efforts allow the use of simple and inexpensive equipment for the fabrication process under normal laboratory environment.

Chapter 6

Conclusions

In the present research, various problems associated with fabrication of ATZ and YSZ-Gr composites were investigated and conditions for preparing these ceramic composites were optimised. The prepared composites were used to fabricate and test the performance of a MEMS scale microthruster. The major factor that restrains further development of chemical micropropulsion system was the lack of suitable microfabrication techniques for refractory materials. To address this issue, the current research has successfully demonstrated the potential of gel casting on PDMS soft molds as a new route for fabricating MEMS scale microthruster.

6.1 Alumina toughened zirconia (ATZ) composites

- The conditions for preparing well dispersed ATZ composites using gel casting technique were optimised. Zeta potential and rheological test confirmed that 0.6 wt. % dispersant (Dolapix CE64) was the optimum amount to be used. The lowest viscosities were measured at this concentration. Low viscosity was desired in this case as it provides better fluidity of ceramic suspension and facilitated the gel casting process. Optimized dispersant amount was used to fabricate ATZ ceramic composites.
- Optimum amount of glycerol was identified to overcome brittleness of ceramics; thus favourable for lamination of ceramic layers. Experimental results revealed that premix-to-glycerol ratio of 2:4 are sufficient to provide required plasticity for ceramic layers. Below these ratio, ceramic layers are

strong however brittle and susceptible to crack during lamination. Above the ratio of 2:4, yield strength of ceramic green bodies was reduced.

- Various types of sintering were investigated to densify the ceramic. Double step sintering was shown to be an effective sintering mechanism at low temperature yet achieving relative density above 95 % and low porosity (0.15) in comparison to partial or single step sintering. Besides, contact angles of composites sintered via double step sintering was higher (indicating lesser pores) in comparison to partial or single step sintering.
- There was an improvement of ~25.3 % in fracture toughness of ATZ composites produced with the addition of only 20 wt. % Al_2O_3. Al_2O_3 was found to be anchored in between zirconia grains and different toughening mechanisms were observed including crack bridging and deflection. The results and observation of this work suggests that Al_2O_3 produced good reinforcement and improved fracture resistance of zirconia matrix.

6.2 Yttria stabilised zirconia (YSZ) - graphene composites

- Well dispersed YSZ-Gr composites were obtained by optimizing the processing conditions. Different factors such as stirring speed, stirring time and graphene loading were investigated. YSZ-Gr composites were prepared by gel casting on PDMS soft mold and sintered using tubular furnace at 1200°C in presence of argon gas. The processing conditions include stirring at 500 rpm for 14 hours. Longer stirring duration and higher stirring speed led to graphene narrowing and breakage. XRD analysis confirmed presence of graphene on all samples at $2\theta=27°$. Anchoring of graphene platelets in the zirconia matrix were observed.

- There was an improvement of ~26 % in the fracture toughness of the composite with the addition of 1 wt. % graphene platelets. Various toughening mechanisms including graphene pull-out, crack bridging, crack deflection and crack branching were observed. Graphene increased electrical conductivity of monolithic zirconia by ~9 orders of magnitude. The present study suggests that graphene is a good reinforcement for improving both mechanical and electrical properties of monolithic ceramics.
- The damping behaviour of YSZ at various frequencies and wt. % graphene platelets were investigated. It was discovered that addition of 1 wt. % graphene platelets improved damping behaviour of YSZ by ~280 % at a frequency of 25 Hz. This behaviour is useful for ceramics utilized in propulsion devices to overcome the barrage of shock waves.

6.3 Fabrication of MEMS scale microthruster

- MEMS scale microthruster have been successfully fabricated using ATZ and YSZ-Gr composite. Prototype of microthruster consisting of five major components (propellant reservoir, injector, electrodes, micronozzle and combustion chamber) was proposed and tested for its performance. Since graphene has very good electrical properties, it provided the conductive paths needed to decompose propellant and thus generate thrust. SEM analysis indicated that all design features of microthruster were successfully molded with minimal shape distortion.
- Optimum flowrate for the current microthruster was at 60 µl/min as decrease in thrust was observed above this flowrate. Optimum flowrate indicates optimum contact time of HAN with the conductive YSZ- Gr surface which is

required for efficient decomposition of HAN. The thruster design proposed in the present study and its testing were successful as maximum thrust (180.5 mN) was achieved at a propellant flow rate of 60 µl/min.

6.4 Future works

- Different gel systems may be investigated to search for a more stable gel system since the current acrylamide based gel system is moisture sensitive. The gel casted layers need to be kept in closed container to prevent absorption of moisture from environment which will over plasticize ceramic green layers. The original gel casting system used an aqueous solution of two monomers; methacrylamide (MAM) and methacrylamide (MBAM) for crosslinking. Although this system has been used extensively to produce ceramics, new ceramics can be produced that uses only one mono-functional monomer, hydroxymethylacrylamide (HMAM) and a special initiator. HMAM is available commercially, produces lower viscosity slips at comparable solid loadings and has superior mold release characteristics.
- Since graphene based ceramic composites are electrically conductive, they can be explored in future for use as electrodes to study the decomposition of propellants such as HAN.
- Issues associated with dispersing high graphene loading and deterioration of mechanical properties have been least investigated. To further address this issue, fundamental idea of stress transfer (interfacial bond strength) between ceramic and graphene are needed. For example; prediction and measuring interfacial adhesion of ceramic-graphene composites.

- Microthruster prototypes with better dimensional control can be achieved with better microfabrication facilities. For example, master molds can be prepared using advanced techniques such as soft lithography to improve dimensional resolution.
- Embedding temperature sensors into the microthruster will enable the measurement of temperature profile during propellant decomposition. However, this system will add complexity as it requires proper data acquisition system (DAQ); thus incur more cost.
- Current work has demonstrated thruster performance at one specified dimension. Effect of varying thruster dimensions (e.g.: nozzle size, exit to throat ratio, converging and diverging angle) can be investigated. The results obtained can be verified by simulation results.
- The sensitivity of the load cell and hence thrust produced under varied propellant flowrate conditions in an open atmosphere presents an area of concern for the overall robustness of the ceramic microthruster. Therefore, vacutherm (vacuum heating and drying) ovens can be used for testing thruster under rough vacuum conditions.

6.5 Research contributions

Current research work contributes to materials and processing field in three areas:

1. *Materials*: Alumina toughened zirconia (ATZ) is used as main structural material for microthruster body. Performance of ceramic microthruster is expected to be better than conventional silicon based systems due to its high hardness values and resistance to fracture.
2. *Design*: A new design has been proposed for the microthruster. Graphene will provide conductive paths to decompose propellant and produce thrust.
3. *Processing*: Gel casting on PDMS soft molds can be considered as the novel fabrication route for micropropulsion system after the state of art silicon microfabrication technology.

REFERENCES

1. A. Nevarez-Rascon, A. Aguilar-Elguezabal, E. Orrantia, and M. H. Bocanegra-Bernal: On the wide range of mechanical properties of ZTA and ATZ based dental ceramic composites by varying the Al_2O_3 and ZrO_2 content. *Int. J. Refract. Met. Hard Mater.* **27**(6), 962 (2009).
2. L.F. He, Y.W. Bao, and Y.C. Zhou: Zirconium Aluminum Carbides: New Precursors for Synthesizing ZrO_2-Al_2O_3 Composites. *J. Am. Ceram. Soc.* **92**(11), 2751 (2009).
3. D. Casellas, M. . Nagl, L. Llanes, and M. Anglada: Fracture toughness of alumina and ZTA ceramics: microstructural coarsening effects. *J. Mater. Process. Technol.* **143**–**144**, 148 (2003).
4. M. Abden, M. Islam, and J. Afroze: Microstructure and Mechanical Properties of 3YSZ Ceramics Rainforced with Al_2O_3 Particles. *Int. J. Mater.* **4**(4), 129 (2014).
5. F. Raether: Ceramic Matrix Composites – an Alternative for Challenging Construction Tasks. *Ceram. Appications* **1**(1), 45 (2013).
6. D. Schawaller, B. Clauß, and M. R. Buchmeiser: Ceramic filament fibers - A review. *Macromol. Mater. Eng.* **297**(6), 502 (2012).
7. S. Pfeifer, P. Demirci, R. Duran, H. Stolpmann, A. Renfftlen, S. Nemrava, R. Niewa, B. Clauß, and M. R. Buchmeiser: Synthesis of zirconia toughened alumina (ZTA) fibers for high performance materials. *J. Eur. Ceram. Soc.* **36**(3), 725 (2016).
8. C. Gómez-navarro, M. Burghard, and K. Kern: Elastic Properties of Chemically Derived Single Graphene Sheets 2008. *Nano Lett.* **8**(7), 2045 (2008).
9. V. Singh, D. Joung, L. Zhai, S. Das, S. I. Khondaker, and S. Seal: Graphene based materials: Past, present and future. *Prog. Mater. Sci.* **56**(8), 1178 (2011).
10. Koller A: Structure and Properties of Ceramics (Elsevier Publishing Company, Amsterdam, 1994).
11. M. Sternitzke: Review : Structural Ceramic Nanocomposites. *J. Eur. Ceram. Soc.* **17**, 1061 (1997).
12. S.M. Choi and H. Awaji: Nanocomposites—a new material design concept.

Sci. Technol. Adv. Mater. **6**(1), 2 (2005).

13. V. Lekholm, A. Persson, K. Palmer, F. Ericson, and G. Thornell: High-temperature zirconia microthruster with an integrated flow sensor. *J. Micromechanics Microengineering* **23**(5), 55004 (2013).
14. T. Yuan and A. Li: in *45th AIAA/ASME/SAE/ASEE Jt. Propuls. Conf. Exhib.* (American Institute of Aeronautics and Astronautics, 2009).
15. J. Huh and S. Kwon: Design, fabrication and thrust measurement of a micro liquid monopropellant thruster. *J. Micromechanics Microengineering* **24**(10), 104001 (2014).
16. K. H. Cheah and K.-S. Low: Fabrication and performance evaluation of a high temperature co-fired ceramic vaporizing liquid microthruster. *J. Micromechanics Microengineering* **25**(1), 15013 (2015).
17. D. W. Richerson: Modern Ceramic Enginnering: Properties, Processing and Use in Design, 3rd ed. (CRC Press, Boca Raton, 2006).
18. B. Basu and K. Balani: Advanced Structural Ceramics (John Wiley & Sons, Inc, New Jersey, 2011).
19. V. Srdi and L. Radonji: Transformation Toughening in Sol–Gel-Derived Alumina– Zirconia Composites. *J. Am. Ceram. Soc.* **60**(192258), 2056 (1997).
20. J. Schneider, S. Begand, R. Kriegel, C. Kaps, W. Glien, and T. Oberbach: Low-temperature aging behavior of alumina-toughened zirconia. *J. Am. Ceram. Soc.* **91**(11), 3613 (2008).
21. S. W. Kim, W. S. Chung, K.S. Sohn, C.Y. Son, and S. Lee: Improvement of flexure strength and fracture toughness in alumina matrix composites reinforced with carbon nanotubes. *Mater. Sci. Eng. A* **517**(1–2), 293 (2009).
22. O. G. and F. G. Leriche A, Moortgat G, Cambier F, Homerin P, Thevenot F: Science and technology of zirconia III. *Adv. Ceram.* **B24**, 1033 (1988).
23. G. M. C. Piconi: Zirconia as a ceramic biomaterial. *Biomaterials* **20**(1), 1 (1999).
24. K. S. Novoselov, K. Geim, S. V Morozov, D. Jiang, Y. Zhang, S. V Dubonos, I. V Grigorieva, and A. Firsov: Electric field effect in atomically thin carbon films. *Science* **306**(5696), 666 (2004).

25. K. S. Novoselov, D. Jiang, F. Schedin, T. J. Booth, V. V Khotkevich, S. V Morozov, and A. K. Geim: Two-dimensional atomic crystals. *Proc. Natl. Acad. Sci. U. S. A.* **102**, 10451 (2005).
26. K. Geim and K. S. Novoselov: The rise of graphene. *Nat. Mater.* **6**(3), 183 (2007).
27. A. Balandin, S. Ghosh, W. Bao, I. Calizo, D. Teweldebrhan, F. Miao, and C. N. Lau: Superior thermal conductivity of single-layer graphene. *Nano Lett.* **8**(3), 902 (2008).
28. J. Cho, A. R. Boccaccini, and M. S. P. Shaffer: Ceramic matrix composites containing carbon nanotubes. *J. Mater. Sci.* **44**(8), 1934 (2009).
29. D. M. Wilson and L. R. Visser: High performance oxide fibers for metal and ceramic composites. *Compos. Part A Appl. Sci. Manuf.* **32**(8), 1143 (2001).
30. F. Chastel, E. Flahaut, A. Peigney, and A. Rousset: Carbon nanotube – metal – oxide nanocomposites : microstructure , electrical conductivity and mechanical properties. *Acta Mater.* **48**, 3803 (2000).
31. R. Verdejo, M. M. Bernal, L. J. Romasanta, and M. A. Lopez-Manchado: Graphene filled polymer nanocomposites. *J. Mater. Chem.* **21**(10), 3301 (2011).
32. T. Kim, H. Lee, J. Kim, and K. S. Suh: Synthesis of phase transferable graphene sheets using ionic liquid polymers. *ACS Nano* **4**(3), 1612 (2010).
33. J. Wang, Z. Li, G. Fan, H. Pan, Z. Chen, and D. Zhang: Reinforcement with graphene nanosheets in aluminum matrix composites. *Scr. Mater.* **66**(8), 594 (2012).
34. E. Bekyarova, M. E. Itkis, P. Ramesh, C. Berger, M. Sprinkle, W. Heer, and R. C. Haddon: Chemical modification of epitaxial graphene: spontaneous grafting of aryl groups. *J. Am. Chem. Soc.* **131**(4), 1336 (2009).
35. J. Jiang, J. Wang, and B. Li: Young's modulus of Graphene: a molecular dynamics study. *Sci. York* **2**(1), 3 (2009).
36. Z.S. Wu, G. Zhou, L.C. Yin, W. Ren, F. Li, and H.-M. Cheng: Graphene/metal oxide composite electrode materials for energy storage. Nano Energy 1(1), 107 (2012).
37. L. Tang, Y. Wang, Y. Li, H. Feng, J. Lu, and J. Li: Preparation, Structure, and Electrochemical Properties of Reduced Graphene Sheet Films. *Adv. Funct. Mater.* **19**(17), 2782 (2009).

38. T. Ramanathan, a a Abdala, S. Stankovich, D. a Dikin, M. Herrera-Alonso, R. D. Piner, D. H. Adamson, H. C. Schniepp, X. Chen, R. S. Ruoff, S. T. Nguyen, I. a Aksay, R. K. Prud'Homme, and L. C. Brinson: Functionalized graphene sheets for polymer nanocomposites. *Nat. Nanotechnol.* **3**(6), 327 (2008).
39. N. Guo and M. C. Leu: Effect of different graphite materials on the electrical conductivity and flexural strength of bipolar plates fabricated using selective laser sintering. *Int. J. Hydrogen Energy* **37**(4), 3558 (2012).
40. F. W. Low, C. W. Lai, and S. B. Abd Hamid: Easy preparation of ultrathin reduced graphene oxide sheets at a high stirring speed. *Ceram. Int.* **41**(4), 5798 (2015).
41. V. Georgakilas, M. Otyepka, A. B. Bourlinos, V. Chandra, N. Kim, K. C. Kemp, P. Hobza, R. Zboril, and K. S. Kim: Functionalization of graphene: covalent and non-covalent approaches, derivatives and applications. *Chem. Rev.* **112**(11), 6156 (2012).
42. W. Gao, L. B. Alemany, L. Ci, and P. M. Ajayan: New insights into the structure and reduction of graphite oxide. *Nat. Chem.* 1, 403 (2009).
43. T. Szabo, O. Berkesi, P. Forgo, K. Josepovits, Y. Sanakis, D. Petridis, and I. Dekany: Evolution of Surface Functional Groups in a Series of Progressively Oxidized Graphite Oxides. *Chem. Mater.* 18, 2740 (2006).
44. J. Wei, T. Vo, and F. Inam: Epoxy/graphene nanocomposites – processing and properties: a review. *RSC Adv.* **5**(90), 73510 (2015).
45. A. B. Bourlinos, D. Gournis, D. Petridis, T. Szabó, A. Szeri, and I. Dékány: Graphite Oxide: Chemical Reduction to Graphite and Surface Modification with Primary Aliphatic Amines and Amino Acids. *Langmuir* **19**(15), 6050 (2003).
46. A. Castro Neto, F. Guinea, N. Peres, K. Novoselov, and A. Geim: The electronic properties of graphene. *Rev. Mod. Phys.* **81**(1), 109 (2009).
47. M. M. J. Treacy, T. W. Ebbesen, and J. M. Gibson: Exceptionally high Young's modulus observed for individual carbon nanotubes. *Nature* **381**, 678 (1996).
48. B. I. Yakobson: Mechanical relaxation and "intramolecular plasticity" in carbon nanotubes. *Appl. Phys. Lett.* 72, 918 (1998).
49. M. Yu: Strength and Breaking Mechanism of Multiwalled Carbon Nanotubes

Under Tensile Load. *Science (80).* **287**(5453), 637 (2000).

50. V. Sazonova, Y. Yaish, H. Ustünel, D. Roundy, T. A. Arias, and P. L. McEuen: A tunable carbon nanotube electromechanical oscillator. *Nature* 431, 284 (2004).
51. P. Steurer, R. Wissert, R. Thomann, and R. Mulhaupt: Functionalized graphenes and thermoplastic nanocomposites based upon expanded graphite oxide. *Macromol. Rapid Commun.* **30**(4–5), 316 (2009).
52. J. Hwang, T. Yoon, S. H. Jin, J. Lee, T.-S. Kim, S. H. Hong, and S. Jeon: Enhanced mechanical properties of graphene/copper nanocomposites using a molecular-level mixing process. *Adv. Mater.* **25**(46), 6724 (2013).
53. Y. Zhang and C. Pan: Measurements of mechanical properties and number of layers of graphene from nano-indentation. *Diam. Relat. Mater.* **24**, 1 (2012).
54. H. Q. Li, Y. G. Wang, C. X. Wang, and Y. Y. Xia: A competitive candidate material for aqueous supercapacitors: High surface-area graphite. *J. Power Sources* **185**(2), 1557 (2008).
55. G. Fugallo, A. Cepellotti, L. Paulatto, M. Lazzeri, N. Marzari, and F. Mauri: Thermal Conductivity of Graphene and Graphite: Collective Excitations and Mean Free Paths. *Nano Lett.* **14**(11), 6109 (2014).
56. V. V Brazhkin, V. L. Solozhenko, V. I. Bugakov, S. N. Dub, O. O. Kurakevych, M. V Kondrin, and A. G. Lyapin: Bulk nanostructured carbon phases prepared from C60: approaching the ideal hardness. *J. Phys. Condens. Matter* **19**(23), 236209 (2007).
57. A. Peigney, C. H. Laurent, E. Flahaut, and A. Rousset: Carbon nanotubes in novel ceramic matrix nanocomposites. *Ceram. Int.* **26**, 677 (2000).
58. R. S. Ruoff and D. C. Lorents: Mechanical and thermal properties of carbon nanotubes. *Carbon N. Y.* **33**, 925 (1995).
59. Salvetat-Delmotte, J. P. & Rubio, A. Mechanical properties of carbon nanotubes: A fiber digest for beginners. Carbon N. Y. 40, 1729 (2002).
60. J. R. Patterson, Y. K. Vohra, S. T. Weir, and J. Akella: Single-wall carbon nanotubes under high pressures to 62 GPa studied using designer diamond anvils. *J. Nanosci. Nanotechnol.* **1**, 143 (2001).
61. P. Montes-navajas, N. G. Asenjo, and A. Corma: Surface area measurement of graphene oxide in aqueous solutions. *Langmuir* **29**, 13443 (2013).

62. N. Lombardo, C. Knudson, and R. Ozanich: Thermal Conductivity of Graphene and Graphene Oxide Nanoplatelet. *Ieee* 1 (2014).
63. J. Suk, R. Piner, J. An, and R. Ruoff: Mechanical properties of monolayer graphene oxide. *ACS Nano* **4**, 6557 (2010).
64. A. Alazmi, O. El Tall, S. Rasul, M. N. Hedhili, S. P. Patole, and P. M. F. J. Costa: A process to enhance the specific surface area and capacitance of hydrothermally reduced graphene. *Nanoscale* **8**, 17782 (2016).
65. P. Wu, H. Lv, T. Peng, D. He, and S. Mu: Nano conductive ceramic wedged graphene composites as highly efficient metal supports for oxygen reduction. *Sci. Rep.* **4**, 3968 (2014).
66. A. Esawi and K. Morsi: Dispersion of carbon nanotubes (CNTs) in aluminum powder. *Compos. Part A Appl. Sci. Manuf.* **38**(2), 646 (2007).
67. B. V Manoj Kumar and Y.-W. Kim: Processing of polysiloxane-derived porous ceramics: a review. *Sci. Technol. Adv. Mater.* **11**(4), 44303 (2010).
68. T. A. Ring: Fundamentals of Ceramic Powder Processing and Synthesis (Academic Press,Inc, California, 2015).
69. P. Kun, O. Tapasztó, F. Wéber, and C. Balázsi: Determination of structural and mechanical properties of multilayer graphene added silicon nitride-based composites. *Ceram. Int.* **38**(1), 211 (2012).
70. P. Miranzo, C. Ramírez, B. Román-Manso, L. Garzón, H. R. Gutiérrez, M. Terrones, C. Ocal, M. I. Osendi, and M. Belmonte: In situ processing of electrically conducting graphene/SiC nanocomposites. *J. Eur. Ceram. Soc.* **33**(10), 1665 (2013).
71. O. Tapasztó, M. Markó, and C. Balázsi: Distribution Patterns of Different Carbon Nanostructures in Silicon Nitride Composites. *J. Nanosci. Nanotechnol.* **12**(11), 8775 (2012).
72. M. Michálková, M. Kašiarová, P. Tatarko, J. Dusza, and P. Šajgalík: Effect of homogenization treatment on the fracture behaviour of silicon nitride/graphene nanoplatelets composites. *J. Eur. Ceram. Soc.* **34**(14), 3291 (2014).
73. F. A. T. Guimarães, K. L. Silva, V. Trombini, J. J. Pierri, J. A. Rodrigues, R. Tomasi, and E. M. J. A. Pallone: Correlation between microstructure and mechanical properties of Al2O3/ZrO2 nanocomposites. *Ceram. Int.* **35**(2), 741 (2009).
74. J. K. M. F. Daguano, C. Santos, R. C. Souza, R. M. Balestra, K. Strecker, and

C. N. Elias: Properties of ZrO2-Al2O3 composite as a function of isothermal holding time. *Int. J. Refract. Met. Hard Mater.* **25**(5–6), 374 (2007).

75. A. Centeno, V. G. Rocha, B. Alonso, A. Fernández, C. F. Gutierrez-Gonzalez, R. Torrecillas, and a. Zurutuza: Graphene for tough and electroconductive alumina ceramics. *J. Eur. Ceram. Soc.* **33**(15–16), 3201 (2013).
76. G. B. Yadhukulakrishnan, S. Karumuri, A. Rahman, R. P. Singh, a. Kaan Kalkan, and S. P. Harimkar: Spark plasma sintering of graphene reinforced zirconium diboride ultra-high temperature ceramic composites. *Ceram. Int.* **39**(6), 6637 (2013).
77. L. S. Walker, V. R. Marotto, M. a Rafiee, N. Koratkar, and E. L. Corral: Toughening in graphene ceramic composites. *ACS Nano* **5**(4), 3182 (2011).
78. A. Rincón, R. Moreno, A. S. a. Chinelatto, C. F. Gutierrez, E. Rayón, M. D. Salvador, and A. Borrell: Al2O3-3YTZP-Graphene multilayers produced by tape casting and spark plasma sintering. *J. Eur. Ceram. Soc.* **34**(10), 2427 (2014).
79. Y. Fan, W. Jiang, and A. Kawasaki: Highly Conductive Few-Layer Graphene/Al2O3 Nanocomposites with Tunable Charge Carrier Type. *Adv. Funct. Mater.* **22**(18), 3882 (2012).
80. K. Wang, Y. Wang, Z. Fan, J. Yan, and T. Wei: Preparation of graphene nanosheet/alumina composites by spark plasma sintering. *Mater. Res. Bull.* **46**(2), 315 (2011).
81. S. Watcharotone, D. Dikin, S. Stankovich, R. Piner, I. Jung, G. H. B. Dommett, G. Evmenenko, S.E. Wu, S.-F. Chen, C.P. Liu, S. T. Nguyen, and R. S. Ruoff: Graphene-silica composite thin films as transparent conductors. *Nano Lett.* **7**(7), 1888 (2007).
82. R. Narasimman, S. Vijayan, and K. Prabhakaran: Graphene-reinforced carbon composite foams with improved strength and EMI shielding from sucrose and graphene oxide. *J. Mater. Sci.* **50**(24), 8018 (2015).
83. J. Dimaio, S. Rhyne, Z. Yang, K. Fu, R. Czerw, J. Xu, S. Webster, Y. Sun, D. L. Carroll, and J. Ballato: Transparent silica glasses containing single walled carbon nanotubes. *Information Sciences*. **149**, 69 (2003).
84. C. Zheng, M. Feng, X. Zhen, J. Huang, and H. Zhan: Materials investigation of multi-walled carbon nanotubes doped silica gel glass composites. *J. Non-Cryst.Sol.* **354**, 1327 (2008).

85. P. Colombo, G. Mera, R. Riedel, and G. D. Sorarù: Polymer-Derived Ceramics: 40 Years of Research and Innovation in Advanced Ceramics. *J. Am. Ceram. Soc.* **1837**, no (2010).
86. R. Riedel, G. Mera, R. Hauser, and A. Klonczynski: Silicon-Based Polymer-Derived Ceramics: Synthesis Properties and Applications-A Review. *J. Ceram. Soc. Japan* **114**(1330), 425 (2006).
87. H. Porwal, S. Grasso, and M. J. Reece: Review of graphene–ceramic matrix composites. *Adv. Appl. Ceram.* **112**(8), 443 (2013).
88. E. Ionescu, A. Francis, and R. Riedel: Dispersion assessment and studies on AC percolative conductivity in polymer-derived Si–C–N/CNT ceramic nanocomposites. *J. Mater. Sci.* **44**(8), 2055 (2009).
89. F. Ji, Y.L. Li, J.M. Feng, D. Su, Y.Y. Wen, Y. Feng, and F. Hou: Electrochemical performance of graphene nanosheets and ceramic composites as anodes for lithium batteries. *J. Mater. Chem.* **19**(47), 9063 (2009).
90. K. H. Cheah and J. K. Chin: Fabrication of Embedded Microstructures Via Lamination of Thick Gel-Casted Ceramic Layers. *Int. J. Appl. Ceram. Technol.* **11**, 1 (2013).
91. V. Sarin: Comprehensive Hard Materials (Elsevier, 2014).
92. B. Lee, M. Y. Koo, S. H. Jin, K. T. Kim, and S. H. Hong: Simultaneous strengthening and toughening of reduced graphene oxide/alumina composites fabricated by molecular-level mixing process. *Carbon N. Y.* **78**, 212 (2014).
93. Z. A. Munir, U. Anselmi-Tamburini, and M. Ohyanagi: The effect of electric field and pressure on the synthesis and consolidation of materials: A review of the spark plasma sintering method. *J. Mater. Sci.* **41**(3), 763 (2006).
94. J. E. Garay: Current-Activated, Pressure-Assisted Densification of Materials. *Annu. Rev. Mater. Res.* **40**(1), 445 (2010).
95. D. M. Hulbert, D. Jiang, D. V. Dudina, and A. K. Mukherjee: The synthesis and consolidation of hard materials by spark plasma sintering. *Int. J. Refract. Met. Hard Mater.* **27**(2), 367 (2009).
96. B. Milsom, G. Viola, Z. Gao, F. Inam, T. Peijs, and M. J. Reece: The effect of carbon nanotubes on the sintering behaviour of zirconia. *J. Eur. Ceram. Soc.* **32**(16), 4149 (2012).
97. V. An, A. Khasanov, and C. de Izarra: Spark plasma sintering of alumina nanopowders produced by electrical explosion of wires. *Springerplus* **4**(1), 581

(2015).

98. J. F. Bartolomé, A. Smirnov, H.-D. Kurland, J. Grabow, and F. A. Müller: New ZrO_2/Al_2O_3 Nanocomposite Fabricated from Hybrid Nanoparticles Prepared by CO2 Laser Co-Vaporization. *Sci. Rep.* **6**(February), 20589 (2016).
99. S. W. Kim, K. A. Khalil: High Frequency Induction Heating Sintering of Ultra-Fine Al_2O_3-(ZrO_2+X % mol Y_2O_3) Bioceramics S. in *Adv. Mater. Res.* (2007).
100. S.M. Kwon, S.J. Lee, and I.J. Shon: Enhanced properties of nanostructured ZrO_2–graphene composites rapidly sintered via high-frequency induction heating. *Ceram. Int.* **41**(1), 835 (2015).
101. I. Ahmad, M. Islam, H. S. Abdo, T. Subhani, K. A. Khalil, A. Almajid, B. Yazdani, and Y. Zhu: Toughening mechanisms and mechanical properties of graphene nanosheet-reinforced alumina. *Mater. Des.* **88**, 1234 (2015).
102. R. I. Todd, E. Zapata-Solvas, R. S. Bonilla, T. Sneddon, and P. R. Wilshaw: Electrical characteristics of flash sintering: thermal runaway of Joule heating. *J. Eur. Ceram. Soc.* **35**(6), 1865 (2015).
103. M. Cologna, B. Rashkova, and R. Raj: Flash Sintering of Nanograin Zirconia in <5 s at 850°C. *J. Am. Ceram. Soc.* **93**(11), 3556 (2010).
104. S. Grasso, H. Yoshida, H. Porwal, Y. Sakka, and M. Reece: Highly transparent α-alumina obtained by low cost high pressure SPS. *Ceram. Int.* **39**(3), 3243 (2013).
105. N. Claussen: Fracture toughness of Al2O3 with an unstabilized ZrO2Dispersed phase. *J. Am. Ceram. Soc.* **59**(1–2), 49 (1976).
106. D. J. Green, R. H. J. Hannink, and M. V Swain: Transformation Toughening of Ceramics (LRC Press, Boca Raton, Florida, 1989).
107. V. Naglieri, P. Palmero, L. Montanaro, and J. Chevalier: Elaboration of alumina-zirconia composites: Role of the zirconia content on the microstructure and mechanical properties. *Materials (Basel).* **6**(5), 2090 (2013).
108. A. Wojteczko, R. Lach, K. Wojteczko, and Z. Pędzich: Investigations of the subcritical crack growth phenomenon and the estimation of lifetime of alumina and alumina–zirconia composites with different phase arrangements. *Ceram. Int.* **42**(8), 9438 (2016).
109. A. Rittidech and N. Suekwamsue: Influence of yttria additives on structural, microstructural and mechanical properties of alumina–zirconia composites prepared by two-stage sintering. *Ceram. Int.* **41**, S123 (2015).

110. S. Y. Liu, Y. Wang, C. Zhou, and Z. Y. Pan: Mechanical properties and tribological behavior of alumina/zirconia composites modified with SiC and plasma treatment. *Wear* **332**–**333**, 885 (2015).
111. H. L. C. Pulgarin and M. P. Albano: Three different alumina-zirconia composites: Sintering, microstructure and mechanical properties. *Mater. Sci. Eng. A* **639**, 136 (2015).
112. A. Rincón, R. Moreno, A. S. A. Chinelatto, C. F. Gutierrez, M. D. Salvador, and A. Borrell: Effect of graphene and CNFs addition on the mechanical and electrical properties of dense alumina-toughened zirconia composites. *Ceram. Int.* **42**(1), 1105 (2016).
113. L. A. Díaz, S. Rivera, A. Fernández, A. Okunkova, Y. G. Vladimirov, and R. Torrecillas: Mechanical Behavior of Alumina Toughened Zirconia Nanocomposites with Different Alumina Additions. *Adv. Sci. Technol.* **96**, 61 (2014).
114. J. Dusza, J. Morgiel, A. Duszová, L. Kvetková, and M. Nosko: Microstructure and fracture toughness of Si_3N_4 + graphene platelet composites. *J. Eur. Ceram. Soc.* **32**, 3389 (2012).
115. C. Ramirez and M. I. Osendi: Toughening in ceramics containing graphene fillers. *Ceram. Int.* **40**(7), 11187 (2014).
116. Y.F. Chen, J.Q. Bi, C.L. Yin, and G.L. You: Microstructure and fracture toughness of graphene nanosheets/alumina composites. *Ceram. Int.* **40**(9), 13883 (2014).
117. L. Kvetková, A. Duszová, P. Hvizdoš, J. Dusza, P. Kun, and C. Balázsi: Fracture toughness and toughening mechanisms in graphene platelet reinforced Si3N4 composites. *Scr. Mater.* **66**(10), 793 (2012).
118. J. Liu, H. Yan, M. J. Reece, and K. Jiang: Toughening of zirconia/alumina composites by the addition of graphene platelets. *J. Eur. Ceram. Soc.* **32**(16), 4185 (2012).
119. J. Liu, H. Yan, and K. Jiang: Mechanical properties of graphene platelet-reinforced alumina ceramic composites. *Ceram. Int.* **39**(6), 6215 (2013).
120. H. Porwal, P. Tatarko, S. Grasso, J. Khaliq, I. Dlouhý, and M. J. Reece: Graphene reinforced alumina nano-composites. *Carbon N. Y.* **64**, 359 (2013).
121. B. Yazdani, Y. Xia, I. Ahmad, and Y. Zhu: Graphene and carbon nanotube (GNT)-reinforced alumina nanocomposites. *J. Eur. Ceram. Soc.* **35**(1), 179

(2015).

122. H. Kim, S. Lee, Y. Oh, Y. Yang, and Y. Lim: Unoxidized graphene/alumina nanocomposite: Fracture-and wear-resistance effects of graphene on alumina matrix. *Sci. Rep.* (2014).
123. J. Dusza, G. Blugan, J. Morgiel, J. Kuebler, F. Inam, T. Peijs, M. J. Reece, and V. Puchy: Hot pressed and spark plasma sintered zirconia/carbon nanofiber composites. *J. Eur. Ceram. Soc.* **29**(15), 3177 (2009).
124. P. Rutkowski, L. Stobierski, D. Zientara, L. Jaworska, P. Klimczyk, and M. Urbanik: The influence of the graphene additive on mechanical properties and wear of hot-pressed Si3N4 matrix composites. *J. Eur. Ceram. Soc.* **35**(1), 87 (2015).
125. M. Belmonte, C. Ramírez, J. González-Julián, J. Schneider, P. Miranzo, and M. I. Osendi: The beneficial effect of graphene nanofillers on the tribological performance of ceramics. *Carbon N. Y.* **61**, 431 (2013).
126. P. Hvizdoš, J. Dusza, and C. Balázsi: Tribological properties of Si3N4–graphene nanocomposites. *J. Eur. Ceram. Soc.* **33**(12), 2359 (2013).
127. J.H. Shin and S.H. Hong: Fabrication and properties of reduced graphene oxide reinforced yttria-stabilized zirconia composite ceramics. *J. Eur. Ceram. Soc.* **34**(5), 1297 (2014).
128. W. Zhang, A. a. Dehghani-Sanij, and R. S. Blackburn: Carbon based conductive polymer composites. *J. Mater. Sci.* **42**(10), 3408 (2007).
129. N. Grossiord, J. Loos, O. Regev, and C. Koning: Toolbox for dispersing carbon nanotubes into polymers to get conductive nanocomposites. *Chem. Mater.* **18**, 1089 (2006).
130. I. Balberg and N. Binenbaum: Computer study of the percolation threshold in a two-dimensional anisotropic system of conducting sticks. *Phys. Rev. B* No. October (1983).
131. R. Hashemi and G. J. Weng: A theoretical treatment of graphene nanocomposites with percolation threshold, tunneling-assisted conductivity and microcapacitor effect in AC and DC electrical settings. *Carbon N. Y.* **96**(April), 474 (2016).
132. Y. Fan, L. Wang, J. Li, J. Li, S. Sun, F. Chen, L. Chen, and W. Jiang: Preparation and electrical properties of graphene nanosheet/Al2O3 composites. *Carbon N. Y.* **48**(6), 1743 (2010).

133. Y. Çelik, A. Çelik, E. Flahaut, and E. Suvaci: Anisotropic mechanical and functional properties of graphene-based alumina matrix nanocomposites. *J. Eur. Ceram. Soc.* **36**(8), 2075 (2016).
134. D. McLachlan: Electrical resistivity of composites. *J. Am. Ceram. Soc.* **73**(8), 2187 (1990).
135. C. Ramirez, L. Garzón, P. Miranzo, M. I. Osendi, and C. Ocal: Electrical conductivity maps in graphene nanoplatelet/silicon nitride composites using conducting scanning force microscopy. *Carbon N. Y.* **49**(12), 3873 (2011).
136. C. Ramirez, F. M. Figueiredo, P. Miranzo, P. Poza, and M. I. Osendi: Graphene nanoplatelet/silicon nitride composites with high electrical conductivity. *Carbon N. Y.* **50**(10), 3607 (2012).
137. P. Čapková, V. Matějka, J. Tokarský, P. Peikertová, L. Neuwirthová, L. Kulhánková, J. Beňo, and V. Stýskala: Electrically conductive aluminosilicate/graphene nanocomposite. *J. Eur. Ceram. Soc.* **34**(12), 3111 (2014).
138. C. Ramirez, F. M. Figueiredo, P. Miranzo, P. Poza, and M. I. Osendi: Graphene nanoplatelet/silicon nitride composites with high electrical conductivity. *Carbon N. Y.* **50**(10), 3607 (2012).
139. G. A. Landis: Robotic exploration of the surface and atmosphere of Venus. *Acta Astronaut.* **59**(7), 570 (2006).
140. M.-H. Wu and P.-S. Lin: Design, fabrication and characterization of a low-temperature co-fired ceramic gaseous bi-propellant microthruster. *J. Micromechanics Microengineering* **20**(8), 85026 (2010).
141. D. Plumlee, J. Steciak, and A. Moll: Development and simulation of an embedded hydrogen peroxide catalyst chamber in low-temperature co-fired ceramics. *Int. J. Appl. Ceram. Technol.* **4**(5), 406 (2007).
142. M.H. Wu and R. Yetter: A novel electrolytic ignition monopropellant microthruster based on low temperature co-fired ceramic tape technology. *Lab Chip* **9**(7), 910 (2009).
143. K. L. Zhang, S. K. Chou, and S. S. Ang: Development of a solid propellant microthruster with chamber and nozzle etched on a wafer surface. *J. Micromechanics Microengineering* **14**(6), 785 (2004).
144. S. Z. Alois Friedberger, Georg Schulte,Gerhard Mueller, Dimitri Telitschkin: US 8407980 B2 (2013).

145. R. Mohammad-Rezaei, H. Razmi, and M. Jabbari: Graphene ceramic composite as a new kind of surface-renewable electrode: application to the electroanalysis of ascorbic acid. *Microchim. Acta* **181**(15–16), 1879 (2014).
146. M. Zhou, T. Lin, F. Huang, Y. Zhong, Z. Wang, Y. Tang, H. Bi, D. Wan, and J. Lin: Highly Conductive Porous Graphene/Ceramic Composites for Heat Transfer and Thermal Energy Storage. *Adv. Funct. Mater.* **23**(18), 2263 (2013).
147. C. F. Gutierrez-Gonzalez, A. Smirnov, A. Centeno, A. Fernández, B. Alonso, V. G. Rocha, R. Torrecillas, A. Zurutuza, and J. F. Bartolome: Wear behavior of graphene/alumina composite. *Ceram. Int.* **41**(6), 7434 (2015).
148. G. Eda and M. Chhowalla: Graphene-based composite thin films for electronics. *Nano Lett.* **9**(2), 814 (2009).
149. G. Gogotsi, V. Galenko, and B. Ozerskii: Fracture toughness, strength, and other characteristics of yttria-stabilized zirconium ceramics. *Ind. Ceram.* **41** (2000).
150. S. R. Choi and N. P. Bansal: Mechanical behavior of zirconia/alumina composites. *Ceram. Int.* **31**(1), 39 (2005).
151. A. Kishimoto, M. Ito, and S. Fujitsu: Microwave sintering of ion conductive zirconia based Microwave sintering of ion conductive zirconia based composite dispersed with alumina. *J. Mater. Sci. Lett.* 943 (2001).
152. H. Tsubakino, T. Fujiwara, K. Satani, and S. Ioku: Composition of grain boundary phase formed in zirconia-3 mol% yttria containing alumina. *J. Mater. Sci.* **6**(c), 4 (1997).
153. T. Oungkulsolmongkol: Hardness and fracture toughness of alumina-based particulate composites with zirconia and strontia additives. *J. Met. Mater.* **20**(2), 71 (2010).
154. S. Dwivedi, S. Sharma, and R. Mishra: A356 Aluminum Alloy and applications-A Review. *Adv. Mater. Manuf.* **2**, 81 (2014).
155. D. K. Koli, G. Agnihotri, and R. Purohit: A Review on Properties, Behaviour and Processing Methods for Al- Nano Al2O3 Composites. *Procedia Mater. Sci.* **6**(Icmpc), 567 (2014).
156. M. Moraes and C. Elias: Mechanical properties of alumina-zirconia composites for ceramic abutments. *Mater.* **7**(4), 643 (2004).
157. K. Kageyama, Y. Harada, and H. Kato: Preparation and mechanical properties of alumina-zirconia composites with agglomerated structures using pre-sintered

powder. *Mater. Trans.* **44**(8), 1571 (2003).

158. G. R. Anstis, P. Chantikul, D. B. Marshall, and B. R. Lawn: A critical evaluation of indentation techniques for measuring fracture toughness: I. Direct crack measurements. *J. Am. Ceram. Soc.* **64**, 533 (1981).
159. H. Sarraf, L. Skarpova, J. Havrda, and L. Bartovska: Evaluation of the Effect of Solid Loadings on Rheological Properties of Highly Concentrated Biocompatible Nanoparticle Suspensions. *J. Nanotechnol. Nanomedicine Nanobiotechnology* **3**(1), 1 (2016).
160. E. E. Tkalya, M. Ghislandi, G. de With, and C. E. Koning: The use of surfactants for dispersing carbon nanotubes and graphene to make conductive nanocomposites. *Curr. Opin. Colloid Interface Sci.* **17**(4), 225 (2012).
161. J. Luo and R. Stevens: Tetragonality of Nanosized 3Y-TZP Powders. *J. Am. Ceram. Soc.* **82**(7), 1922 (1999).
162. A. M. Herrera, A. Antônio, M. De Oliveira, A. P. Novaes De Oliveira, and D. Hotza: Processing and Characterization of Yttria-Stabilized Zirconia Foams for High-Temperature Applications. *J. Ceram.* **785210**(8) (2013).
163. S. P. Rao, S. S. Tripathy, and A. M. Raichur: Dispersion studies of sub-micron zirconia using Dolapix CE 64. *Colloids Surfaces A Physicochem. Eng. Asp.* **302**(1–3), 553 (2007).
164. H. Majidian, T. Ebadzadeh, and E. Salahi: Stability properties of alumina-zircon-SiC suspensions by adsorption of Dolapix onto the particles. *J. Ceram.* **348**(2013), 342 (2013).
165. L. Besra, D. K. Sengupta, B. P. Singh, and S. Bhattacharjee: *J. Am. Ceram. Soc.* **88**, 109 (2005).
166. B. P. Singh, R. Menchavez, C. Takai, M. Fuji, and M. Takahashi: Stability of dispersions of colloidal alumina particles in aqueous suspensions. *J. Colloid Interface Sci.* **291**(1), 181 (2005).
167. Pradip: On the Interpretation of Electrokinetic Behavior of Chemisorbing Surfactant Systems. *Trans. Indian Inst.* **41**(1), 15 (1988).
168. X. Jiang, Y. Rui, and G. Chen: Improved Properties of Cotton by Atmospheric Pressure Plasma Polymerization Deposition of Sericin. *J Vinyl Addit. Technol* **21**(2), 129 (2009).
169. K. Pandey, N. Asthana, M. M. Dwivedi, and S. K. Chaturvedi: Effect of Plasticizers on Structural and Dielectric Behaviour of [PEO + (NH 4) 2 C 4 H

8 (COO) 2] Polymer Electrolyte. *J. Polym.* **2013**, 1 (2013).

170. E. Bernardo, P. Colombo, E. Pippel, and J. Woltersdorf: Novel Mullite Synthesis Based on Alumina Nanoparticles and a Preceramic Polymer. *J. Am. Ceram. Soc.* **89**(5), 1577 (2006).
171. D. Galusek, Z. Lencés, P. Sajgalík, and R. Riedel: Thermal analysis study of polymer-to-ceramic conversion of organosilicon precursors. *J. Min. Metall. Sect. B Metall.* **44**(1), 35 (2008).
172. I. Kaus, P. I. Dahl, J. Mastin, T. Grande, and M.-A. Einarsrud: Synthesis and Characterization of Nanocrystalline YSZ Powder by Smoldering Combustion Synthesis. *J. Nanomater.* **2006**, 1 (2006).
173. T. Oszinda, M. Schaller, and S. Schulz: Chemical repair of plasma damaged porous ultra low-κ SiOCH film using a vapor phase process. *J. Electrochem.* **157**(12), 1140 (2010).
174. J. Judes and V. Kamaraj: Preparation and characterization of yttria stabilized zirconia minispheres by the sol-gel drop generation method. *Mater. Sci.* **27**(2), 407 (2009).
175. S. Cavalu, F. Banica, V. Simon, I. Akin, and G. Goller: Surface Modification of Alumina/ Zirconia Ceramics Upon Different Fluoride-Based Treatments. *Int. J. Appl. Ceram. Technol.* **11**(2), 402 (2014).
176. S. Kaur, R. Riedel, and E. Ionescu: Pressureless fabrication of dense monolithic SiC ceramics from a polycarbosilane. *J. Eur. Ceram. Soc.* **34**(15), 3571 (2014).
177. A. Žalga, A. Kareiva, and A. Žarkov: UV-Vis spectroscopical investigations of the YSZ thin films on corundum, silicon and silica substrates. *Chemija* **25**(1), 29 (2014).
178. M. M. Hossen, M. Phil, and A. K. M. A. Hakim: Investigation of Mechanical Properties of Al 2 O 3 - 20 Wt % Zro 2 Composites As a Function of Sintering Temperature. *Eur. Sci. J.* **10**(9), 399 (2014).
179. J. An, J. Zhao, Z. G. Su, Z. Wen, and D. S. Xu: Microstructure and Mechanical Properties of ZTA Ceramic-Lined Composite Pipe Prepared by Centrifugal-SHS *Arab. J. Sci. Eng.* **40**, 2701 (2015).
180. S. Tekeli: Fracture toughness (KIC), hardness, sintering and grain growth behaviour of 8YSCZ/Al2O3 composites produced by colloidal processing. *J. Alloys Compd.* **391**(1–2), 217 (2005).
181. S. W. Kim and K. A.-R. Khalil: High-Frequency Induction Heat Sintering of

Mechanically Alloyed Alumina-Yttria-Stabilized Zirconia Nano-Bioceramics. *J. Am. Ceram. Soc.* **89**(4), 1280 (2006).

182. T. Tsukuma, K., Kubota, Y. and Tsukidate: Thermal and mechanical properties of Y, 2O, 3-stabilised tetragonal zirconia polycrystals. *Adv. Ceram. Sci. Technol. Zirconia II,* **12** (1984).
183. P. Swanson and C. Fairbanks: Crack Interface Grain Bridging as a Fracture Resistance I, Mechanism in Ceramics: I, Experimental Study on Alumina. *J. ...* **70**, 279 (1987).
184. H. De Aza, J. Chevalier, G. Fantozzi, M. Schehl, and R. Torrecillas: Crack growth resistance of alumina, zirconia and zirconia toughened alumina ceramics for joint prostheses. *Biomaterials* **23**(3), 937 (2002).
185. D. Li, Z. Yang, D. Jia, D. Wu, Q. Zhu, B. Liang, S. Wang, and Y. Zhou: Microstructure, oxidation and thermal shock resistance of graphene reinforced SiBCN ceramics. *Ceram. Int.* **42**(3), 4429 (2016).
186. D. Li, M. B. Müller, S. Gilje, R. B. Kaner, and G. G. Wallace: Processable aqueous dispersions of graphene nanosheets. *Nat. Nanotechnol.* **3**(2), 101 (2008).
187. R. K. Chintapalli, F. G. Marro, B. Milsom, M. Reece, and M. Anglada: Processing and characterization of high-density zirconia–carbon nanotube composites. *Mater. Sci. Eng. A* **549**, 50 (2012).
188. M. M. R. Boutz, A. J. A. Winnubst, B. Van Langerak, R. J. M. Olde Scholtenhuis, K. Kreuwel, and A. J. Burggraaf: The effect of ceria co-doping on chemical stability and fracture toughness of Y-TZP. *J. Mater. Sci.* **30**(7), 1854 (1995).
189. J. J. Mccolon: Ceramic Hardness (Plenum Press, New York, 1990).
190. J. D. Lin and J. G. Duh: Fracture toughness and hardness of ceria- and yttria-doped tetragonal zirconia ceramics. *Mater. Chem. Phys.* **78**(1), 253 (2003).
191. S. N. Aqida, M. I. Ghazali, J. Hashim, G. B. V. Kumar, C. S. P. Rao, N. Selvaraj, and M. S. Bhagyashekar: Effects of porosity on mechanical properties of metal matrix composite: an overview. *J. Miner. Mater. Charact. Eng.* **9**(1), 17 (2004).
192. C. Rossi, T. Do Conto, and D. Est: Design , fabrication and modelling of MEMS-based microthrusters for space. *Sma* **10**, 1156 (2001).
193. A. P. London, A. H. Epstein, and J. L. Kerrebrock: High-Pressure Bipropellant

Microrocket Engine. *J. Propuls. Power* **17**(4), 780 (2001).

194. F. Santoni and P. Tortora: Micropropulsion experiment on UNISAT-2. *Aerosp.Conf. Proceed.* **9**, 479 (2002).
195. P. Kundu, T. K. Bhattacharyya, and S. Das: Design, fabrication and performance evaluation of a vaporizing liquid microthruster. *J. Micromechanics Microengineering* **22**(2), 25016 (2012).
196. S. A. Whitmore, D. P. Merkley, M. I. Judson, and S. D. Eilers: Development and Testing of a Green Monopropellant Ignition System. *49th AIAA/ASME/SAE/ASEE Jt. Propuls. Conf.* **7**, 1 (2013).
197. P. Kundu, A. K. Sinha, T. K. Bhattacharyya, and S. Das: MnO_2 Nanowire embedded hydrogen peroxide monopropellant MEMS thruster. *J. Microelectromechanical Syst.* **22**(2), 406 (2013).

APPENDIX

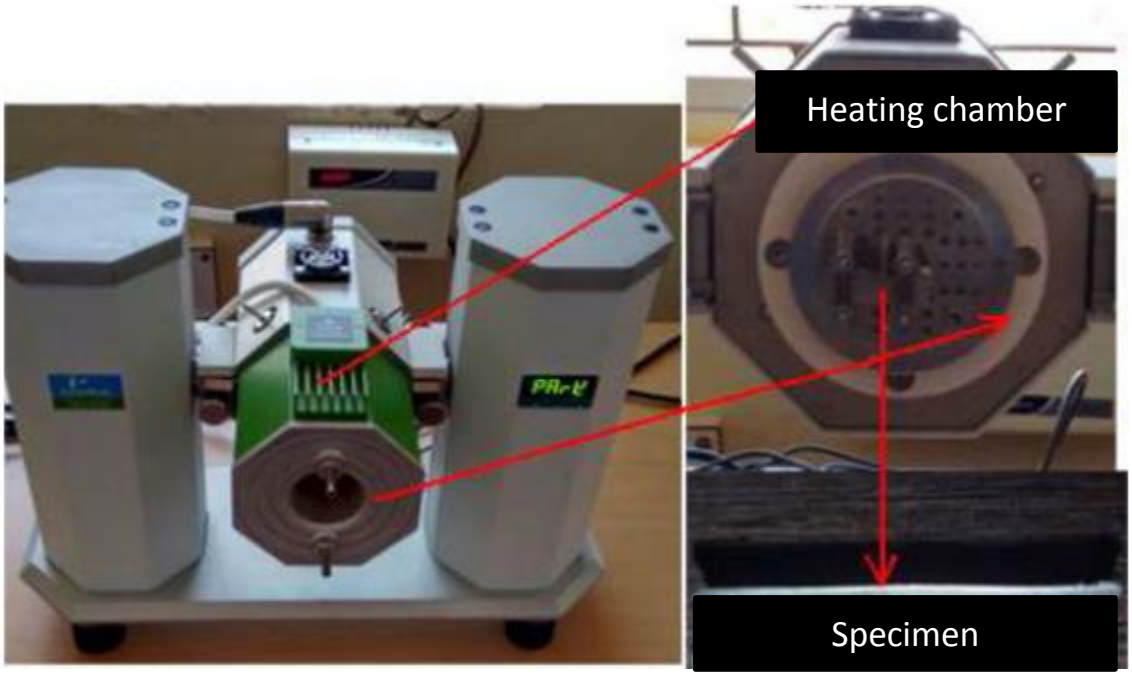

Appendix1.1: Dynamic mechanical analyser (DMA) for testing damping behaviour of ceramic composites.

Appendix1.2: Tubular furnace for sintering YSZ-graphene composites connected with Argon gas.

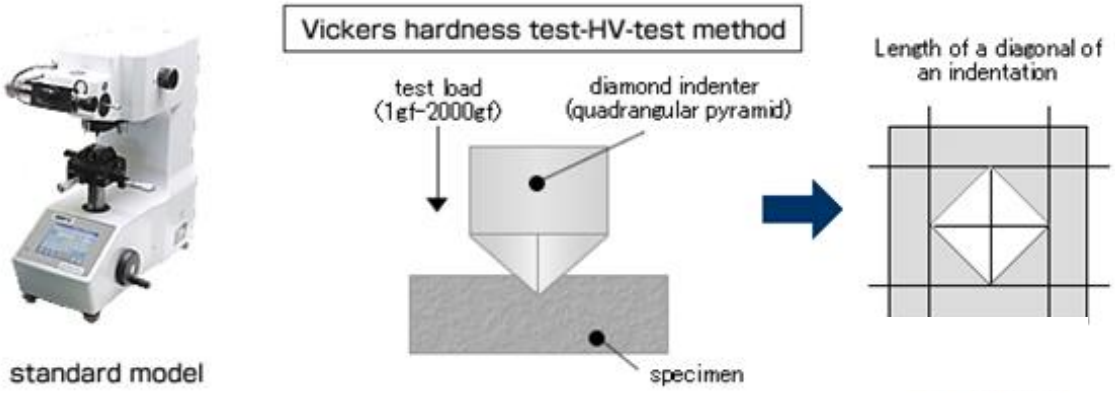

Appendix 1.3: Methodology for measuring hardness using Vickers indentation method.

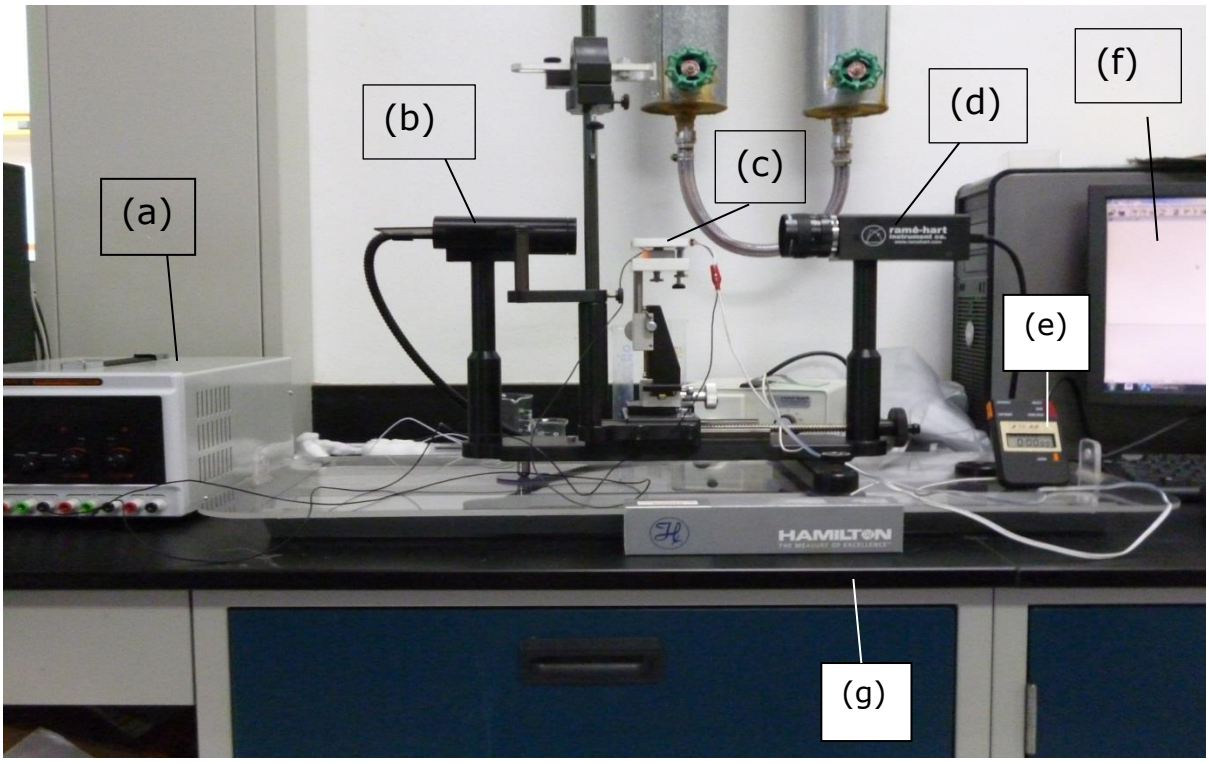

Appendix 1.4:Contact angle measurements using goniometer and computer software, DROPimage (a) Power supply (b) Cold light source (c) Platform (d) Camera (e) Stopwatch (f) Desktop computer connected to the camera (g) Syringe

Cutting plotter condition

Cutting plotter model	Graphtec CE6000
Cutting blade	CB09U
Cutting force	12
Force offset	-2
Speed	1 cm/s
Tangential mode	ON